International Journal of Polymer Science

Polymers and Polymeric Composites with Electronic Applications

Lead Guest Editor: Renbo Wei
Guest Editors: Xiufu Hua and Zhiyuan Xiong

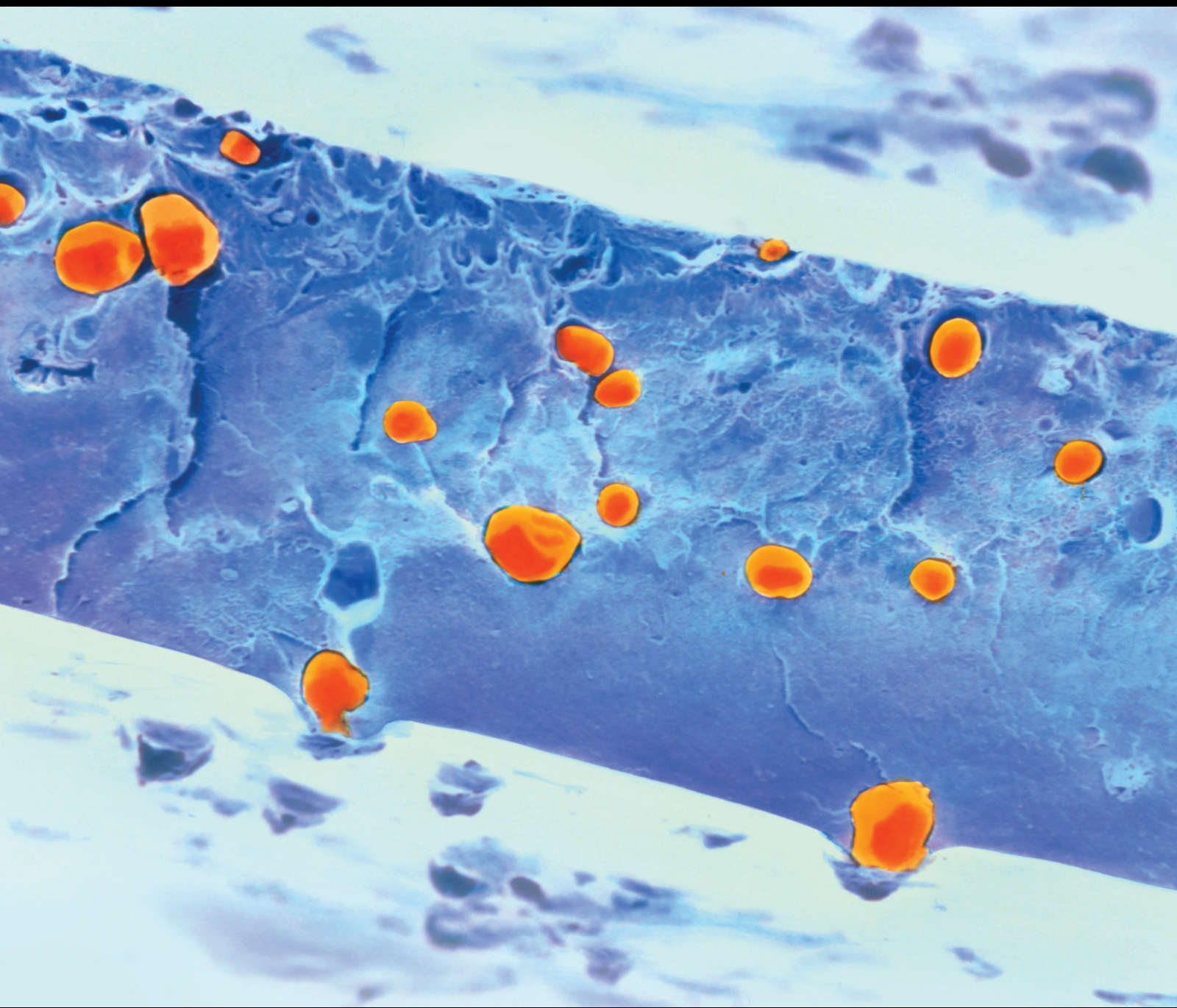

Polymers and Polymeric Composites with Electronic Applications

International Journal of Polymer Science

Polymers and Polymeric Composites with Electronic Applications

Lead Guest Editor: Renbo Wei
Guest Editors: Xiufu Hua and Zhiyuan Xiong

Editorial Board

Contents

Hindawi
International Journal of Polymer Science
Volume 2018, Article ID 8412480, 1 page
https://doi.org/10.1155/2018/8412480

Editorial

Polymers and Polymeric Composites with Electronic Applications

Renbo Wei,[1] **Xiufu Hua**,[2] **and Zhiyuan Xiong**[3]

[1]*Research Branch of Advanced Functional Materials, School of Materials and Energy, University of Electronic Science and Technology of China, Chengdu 610054, China*
[2]*Department of Scientific Research and Development, Tsinghua University, Beijing 100084, China*
[3]*Department of Materials Engineering, Monash University, Victoria 3800, Australia*

Correspondence should be addressed to Renbo Wei; weirb10@uestc.edu.cn

Received 27 August 2018; Accepted 27 August 2018; Published 11 November 2018

The development of the modern society has resulted in all kinds of electronic equipment and devices that are composed of elements which are made from electronic materials. These electronic materials contain the ceramics such as silicon used for the fabrication of the chips, metals like copper which appears in the printed circuits, and the polymeric materials utilized as the insulation, packing, and isolation, among others. In comparing with the inorganic electronic materials, the polymer-based electronic materials have attracted considerable attention due to their relatively low density, flexibility, easy processing, low manufacturing cost, and even recyclable. As a result, polymers and polymeric composites have shown increasing applications as the components in the electronic equipment and devices. What is more, some newly developed polymeric electronic materials are taking the place of their inorganic counterparts. Basing on their electronic applications, this special issue focuses on the preparation, characterization, performances, and applications of some polymer-based electronic materials.

Six original research papers and a review paper were collected in this special issue. These papers are themed on the fabrication and properties of polymeric electronic materials that can be potentially used as component in capacitors, solar cells, light emitting diode, and so on. The details of the topics in this special issue include the following: (1) effect of polar groups on the dielectric properties of dielectric polymers; (2) review of designing and preparing of high dielectric constant polymeric composites; (3) electric conductivity of polymeric composites with copper as a filler; (4) AC conductivity of polymeric composites with a conductive polymer as an additive; (5) designing of copolymers with optimized photoelectric properties through theoretical calculations; (6) microwave absorption properties of polyaniline and magnetite core-shell structured hybrid; and (7) polyimides as binder polymers on organic light-emitting diode panels.

We expect that the related researchers will get inspired by this special issue.

Conflicts of Interest

The guest editorial team declares no conflict of interest regarding the publication of this special issue.

Acknowledgments

We sincerely appreciate the contributions from the authors, the comments and suggestions from the reviewers, and the efforts and supports from the editorial staff members to this special issue.

Renbo Wei
Xiufu Hua
Zhiyuan Xiong

Hindawi
International Journal of Polymer Science
Volume 2018, Article ID 3417060, 6 pages
https://doi.org/10.1155/2018/3417060

Research Article

Preparation and Microwave Absorption Properties of Polyaniline and Magnetite Core-Shell-Structured Hybrid

Xuan Zhang

Department of Chemical Engineering, Northwest University, China

Correspondence should be addressed to Xuan Zhang; zhangxuan0904@stumail.nwu.edu.cn

Received 29 June 2018; Revised 7 August 2018; Accepted 9 August 2018; Published 24 October 2018

Academic Editor: Zhiyuan Xiong

In this study, polyaniline and Fe_3O_4 (PAN@Fe_3O_4) hybrids are fabricated and their microwave absorption property is studied. PAN@Fe_3O_4 hybrids are fabricated by the in situ aniline polymerization at spherical of Fe_3O_4 which is prepared by the solvothermal process. Fourier-transform infrared spectrophotometer (FTIR), X-ray diffraction (XRD), and X-ray photoelectron spectroscopy (XPS) are applied to confirm the composition of the fabricated PAN@Fe_3O_4 hybrids. The morphologies of PAN@Fe_3O_4 hybrids are studied by scanning electron microscope (SEM) and transmission electron microscopy (TEM). The content of polyaniline in the PAN@Fe_3O_4 hybrids is calculated by thermogravimetric analysis (TGA). The magnetic properties of PAN@Fe_3O_4 hybrids are characterized by vibrating sample magnetometer (VSM). The microwave absorption property of PAN@Fe_3O_4 hybrids are measured on a vector network analyzer. The research show that the microwave absorptions property of the obtained PAN@Fe_3O_4 hybrids can be adjusted by controlling the in situ aniline polymerization at spherical of Fe_3O_4.

1. Introduction

With the expansion use of electric device, including personal computers, mobile phones, microwave oven, and other military equipment and/or space equipment, microwave has become a new pollution to our health [1–6]. The effective way to solve this problem is the development of new microwave absorption materials [7, 8]. The basic requirement of the microwave absorption materials is to show strong microwave absorption, represented by reflection loss [9]. Usually, the microwave absorption materials are to dissipate the incident microwave which includes the dielectric dissipation and magnetic dissipation [10, 11]. Excellent microwave absorption materials also exhibit compatibility between the dielectric dissipation and magnetic dissipation. The magnetic dissipation can be easily achieved by using magnetic materials such as magnetic iron oxide. As a result, magnetite is mostly utilized as microwave absorption materials [12, 13]. The dielectric dissipation can be achieved by introducing the dielectric materials and/or conducting materials [14, 15]. These include phthalocyanine copper and its derivatives [16], the carbon materials including CNT [17], carbon black, and graphene [18], and the conducting polymers such as polyaniline and polythiophene [19]. The conducting polymers that usually combine the low density and excellent conductivity have attracted considerable attention both from the research and the practical application. In the conducting polymers, polyaniline (PAN) can be easily obtained and shows excellent conductivity after doping. Up to now, PAN has been used to prepare composites with polyethylene, poly(vinylidene fluoride), graphene, CNT, and others [20, 21].

With the magnetite as the magnetic dissipation part and PAN as the dielectric dissipation part, PAN and magnetite hybrid materials can be obtained to be used as microwave absorption materials. However, another problem is the compatibility between them due to the inorganic part of magnetite and organic part of PAN. To solve this problem, core-shell-structured hybrid containing magnetite core and PAN shell can be imagined.

In this study, we fabricated hybrid PAN@Fe_3O_4 by the in situ aniline polymerization at the spherical of Fe_3O_4 which is

prepared by the solvothermal process. The PAN@Fe_3O_4 hybrids are characterized by XPS, XRD, TGA, SEM, TEM, FTIR, and VSM. After that, microwave absorption property of the prepared PAN@Fe_3O_4 hybrids is studied in detail.

2. Experimental Section

2.1. Materials. Ethylene glycol (99%), $FeCl_3{\cdot}6H_2O$ (99%), and polyethylene glycol 2000 (99%) were purchased from Kelong Reagents, Chengdu, China. Sodium dodecyl benzene sulfonate (SDBS, 99%), hydrochloric acid (37%), ammonium sulfate (98%), and aniline (99%) were purchased from Changzheng Reagents, Chengdu, China. Other chemicals and reagents were commercial available products, and all of them were used as received.

2.2. Preparation of Fe_3O_4. Magnetite was fabricated by the solvothermal process throughout previous literature [8]. $FeCl_3{\cdot}6H_2O$ (10.0 g) and polyethylene glycol 2000 (3.7 g) were mixed with 160 ml ethylene glycol at RT, followed by adding sodium acetate trihydrate (27.0 g). The system was mixed by mechanical agitation as well as ultrasonication for 40 min to form an orange solution. After that, the above-prepared mixture was poured into an autoclave; the whole system was heated at 180°C for 12 h, after that it was cooled down to RT. The product was segregated by a magnet and was purified 3–5 times with purified water and ethanol, respectively. Finally, the product was dried under vacuum at 70°C for 8 h.

2.3. Preparation of Polyaniline and Fe_3O_4 (PAN@Fe_3O_4) Hybrids. The polyaniline and Fe_3O_4 (PAN@Fe_3O_4) hybrids were fabricated by the in situ aniline polymerization at the spherical of Fe_3O_4 with the existence of ammonium sulfate. With the change of the amount of the aniline and ammonium sulfate, polyaniline and Fe_3O_4 hybrids with different contents of polyaniline were obtained. The typical procedure is as follows: 0.25 g Fe_3O_4 was dispersed in 100 ml deionized water with the help of SDBS (25 mg) and mechanical agitation. After that, the system was cooled at 0–5°C through the ice. At the time, aniline (0.25 ml), dissolved in 0.1 mol/l HCl (50 ml), was also cooled at 0–5°C through another ice system. The cooled aniline solution was mixed with the Fe_3O_4 dispersion with vigorous mechanical agitation in the ice bath. The ammonium sulfate (2.5 g) was dissolved in 25 ml purified water at 0–5°C in the third ice bath. After being cooled down, the ammonium sulfate was put dropwise in Fe_3O_4 and aniline mixture. The polymerization was kept on for at least 12 h. In this study, three polyaniline and Fe_3O_4 hybrids named as PAN@Fe_3O_4-1, PAN@Fe_3O_4-2, and PAN@Fe_3O_4-3 were prepared.

2.4. Characterization. The structure of PAN@Fe_3O_4 hybrid materials was characterized by XRD (Rigaku RINT 2400) and XPS (PHI-5300 ESCA). FTIR (8000S) was also utilized to characterize the PAN@Fe_3O_4 hybrids. The content of polyaniline in the PAN@Fe_3O_4 hybrid was calculated by TGA (Q50). The morphologies of PAN@Fe_3O_4 hybrids were studied by SEM (JSM-6490LV) and TEM (H600). The magnetic property of PAN@Fe_3O_4 hybrids was studied by VSM (BHV-525). The electromagnetic property of PAN@Fe_3O_4 hybrids was tested on a vector network analyzer (8720ET) at 0.5–18 GHz. The sample was fabricated through blending PAN@Fe_3O_4 hybrids with wax in a mass ratio of 3 : 1.

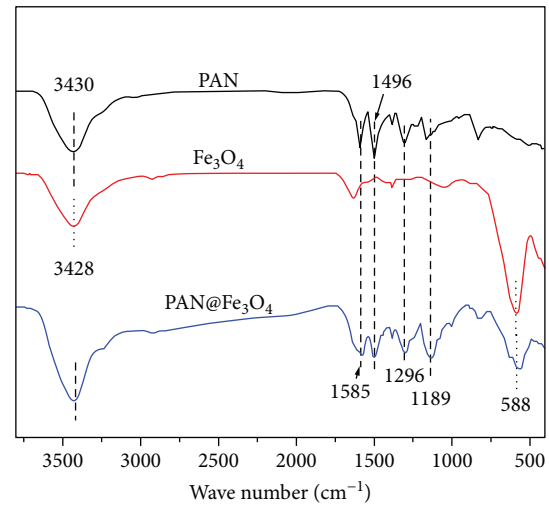

Figure 1: FTIR spectrum of PAN, Fe_3O_4, and PAN@Fe_3O_4-1.

3. Results and Discussion

In the study, polyaniline and Fe_3O_4 (PAN@Fe_3O_4) hybrids are fabricated and their microwave absorption property is studied. The PAN@Fe_3O_4 hybrid is fabricated by the in situ aniline polymerization at the spherical of Fe_3O_4 which is prepared by the solvothermal process [8]. Figure 1 shows FTIR spectra of PAN, Fe_3O_4, as well as PAN@Fe_3O_4-1; compared with that of Fe_3O_4, the FTIR curves of PAN@Fe_3O_4-1 show additional absorption peaks at 3430 cm^{-1} (N-H), 1585 and 1496 cm^{-1} (benzene ring), and 1189 cm^{-1} (AR-N) which indicate the existence of polyaniline in the system [19]. In addition, the peak at 588 cm^{-1} (Fe-O) is observed on the spectra curves of Fe_3O_4 and PAN@Fe_3O_4-1.

XPS is also used to characterize the composition of the obtained PAN@Fe_3O_4 hybrids. Figure 2(a) shows the XPS spectra of Fe_3O_4 and PAN@Fe_3O_4-1. On the spectrum of Fe_3O_4, the peaks at 534 eV and 716 eV correspond the O1s and Fe2p, while the peak at 287 eV is resulted from the C1s which might come from the ethylene glycol and polyethylene glycol 2000 used during the solvothermal process. The Fe2p peak can be divided into two peaks at 711 eV and 725 eV which come from Fe2p1/2 and Fe2p3/2 as shown in Figure 2(b); this confirms the existence of Fe_3O_4. In comparison, the XPS spectrum of PAN@Fe_3O_4-1 shows new peak at 405 eV which is attributed to the N1s from the polyaniline at the spherical of PAN@Fe_3O_4-1. Both of the FTIR and the XPS confirm the preparation of polyaniline and Fe_3O_4 hybrids [7].

XRD is a technic to confirm component of prepared new nanocomposites by comparing XRD pattern peaks with the standard card. Figure 3 shows XRD curves of prepared samples. As shown in the picture, six peaks at 30°, 35°, 43°, 54°, 57°, and 63° which match well with (220), (311), (400),

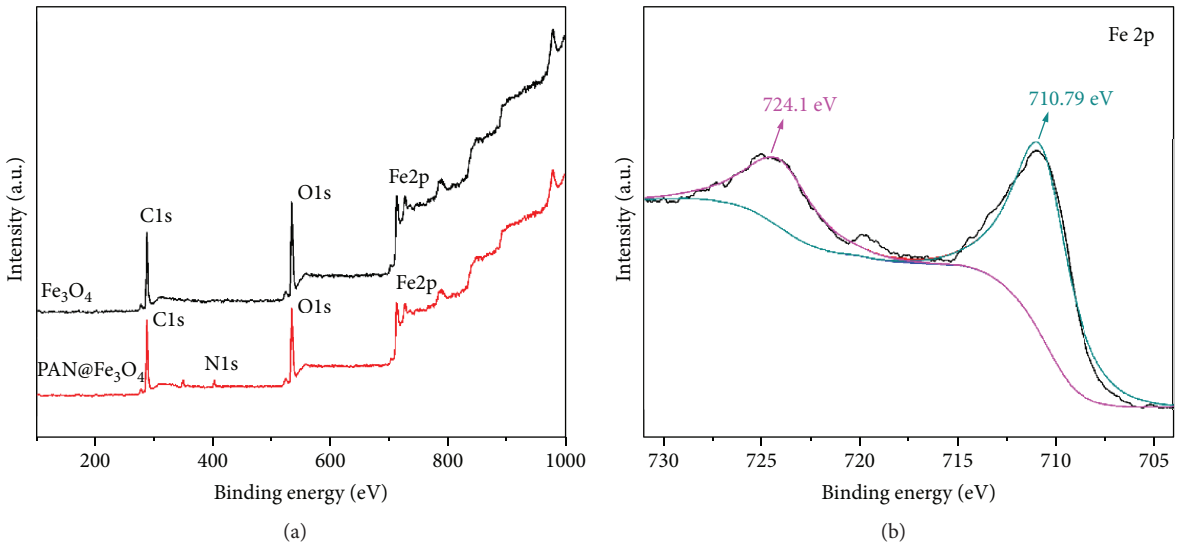

Figure 2: XPS spectra of Fe_3O_4 and PAN@Fe_3O_4-1 (a) and Fe2p peak (b).

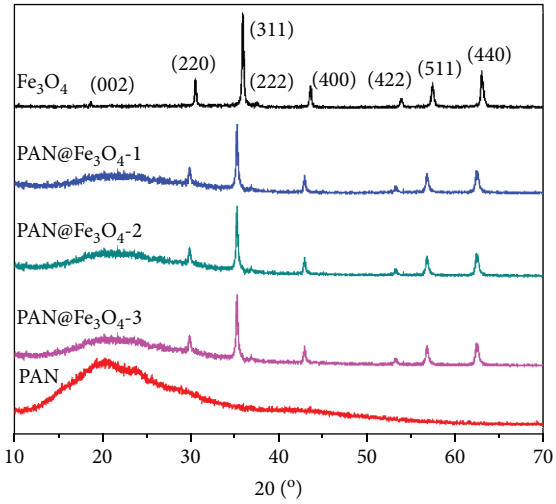

Figure 3: XRD pattern of Fe_3O_4, PAN@Fe_3O_4-1, PAN@Fe_3O_4-2, PAN@Fe_3O_4-3, and PAN.

(422), (511), and (440) planes of the standard XRD of magnetite (JCPDS file no.19-0629) are observed on the curves of Fe_3O_4. While a wide peak at 20° is seen on the curves of PAN. PAN@Fe_3O_4-1 shows peaks combining from PAN and Fe_3O_4, indicating the composition of PAN and Fe_3O_4 in PAN@Fe_3O_4-1. The other samples also show similar XRD patterns which confirm the Fe_3O_4 in the PAN@Fe_3O_4 hybrids [22].

After the characterization of the composition of PAN@Fe_3O_4 hybrids, the micro morphology of them is studied through SEM and TEM. Figure 4 shows SEM micro images of Fe_3O_4 and PAN@Fe_3O_4-1. As shown in the figure, the Fe_3O_4 exhibits smooth surface. In addition, anomalous nanoparticles including spheres, hemispheres, bowls, and open balls are observed for Fe_3O_4. While for PAN@Fe_3O_4-1, its surface becomes coarser indicating the existence of the polyaniline. More importantly, the shape of the PAN@Fe_3O_4-1 becomes regular spheres. The structure change of the PAN@Fe_3O_4-1 from Fe_3O_4 indicates the formation of the core-shell-structured particles.

Figure 5 shows the TEM micro images of Fe_3O_4 and PAN@Fe_3O_4-1. Similar to that of the SEM micro image, the TEM micro image of Fe_3O_4 shows irregular shapes of nanoparticles. In addition, it is clearly that Fe_3O_4 shows hollow structure. As for that of PAN@Fe_3O_4-1, a shell can be observed at the spherical of the nanoparticles. What is more, it seems that the hollow structure of the Fe_3O_4 is filled with something after the polymerization of aniline. Both of the SEM and TEM results indicate the core-shell structure of PAN@Fe_3O_4-1.

After the confirmation of the fabrication of PAN@Fe_3O_4 hybrids, the content of polyaniline in the PAN@Fe_3O_4 hybrids is calculated by the TGA measurement. Figure 6 shows the TGA curves of Fe_3O_4, PAN@Fe_3O_4-1, PAN@Fe_3O_4-2, and PAN@Fe_3O_4-3. Fe_3O_4 shows only 2% weight decrement when the temperature is up to 600°C, which is negligible. As for the PAN@Fe_3O_4 hybrids, obvious weight decrement resulting from the decomposing of polyaniline is observed. The residual mass of PAN@Fe_3O_4-1, PAN@Fe_3O_4-2, and PAN@Fe_3O_4-3 is 90%, 84%, and 77%, respectively. The TGA results mean that the content of polyaniline in PAN@Fe_3O_4-1, PAN@Fe_3O_4-2, and PAN@Fe_3O_4-3 is 10 wt%, 16 wt%, and 23 wt%, respectively.

The magnetic property of PAN@Fe_3O_4 hybrid composite was studied by a VSM. Figure 7 shows the saturation magnetization of the samples indicating the magnetic property of the PAN@Fe_3O_4 hybrids. According to the results, the saturation magnetization decreases with the increasing content of polyaniline due to the decrement of content of Fe_3O_4 which contributes the magnetic properties effectively. The saturation magnetization of PAN@Fe_3O_4-1, PAN@Fe_3O_4-2, and PAN@Fe_3O_4-3 is 75.3, 58.9, and 42.1 emu/g, respectively.

With the fabrication and characterization of PAN@Fe_3O_4 hybrids, their microwave absorption property is studied. Permittivity ($\varepsilon = \varepsilon' + i\varepsilon''$) as well as permeability

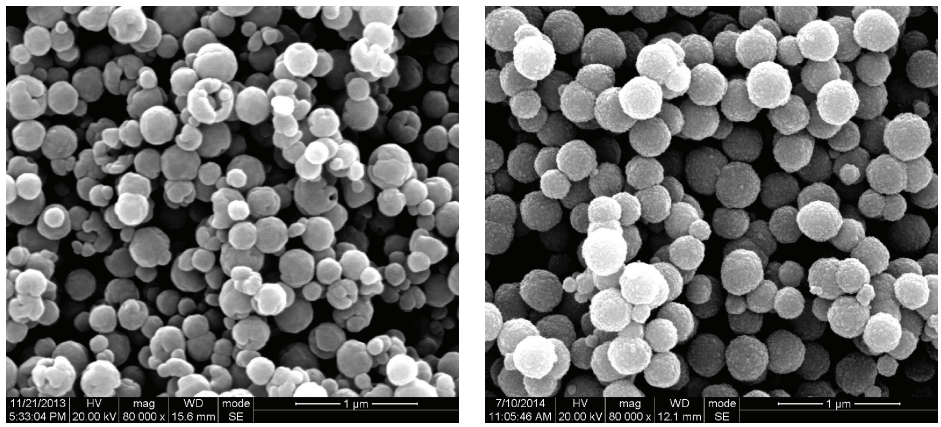

(a) (b)

Figure 4: SEM micro images of Fe_3O_4 and PAN@Fe_3O_4-1.

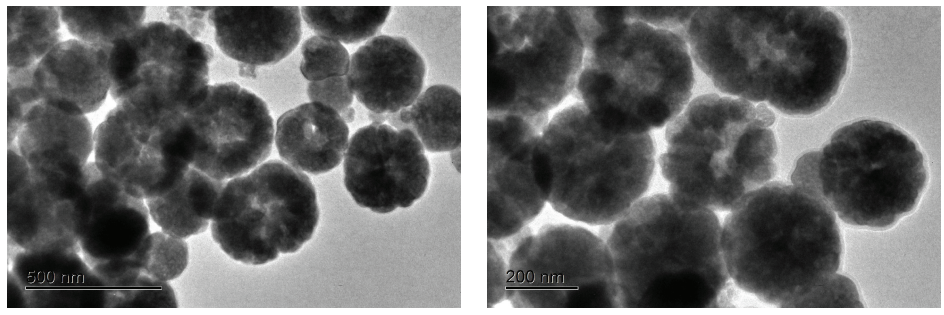

(a) (b)

Figure 5: TEM micro images of Fe_3O_4 and PAN@Fe_3O_4-1.

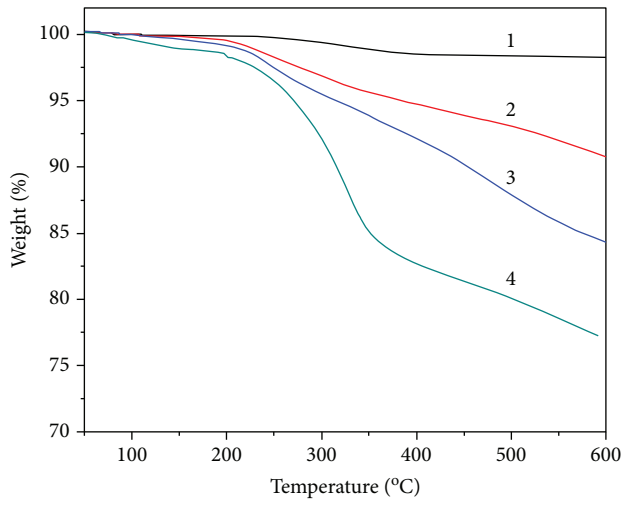

Figure 6: TGA curves of Fe_3O_4 (curve 1), PAN@Fe_3O_4-1 (curve 2), PAN@Fe_3O_4-2 (curve 3), and PAN@Fe_3O_4-3 (curve 4).

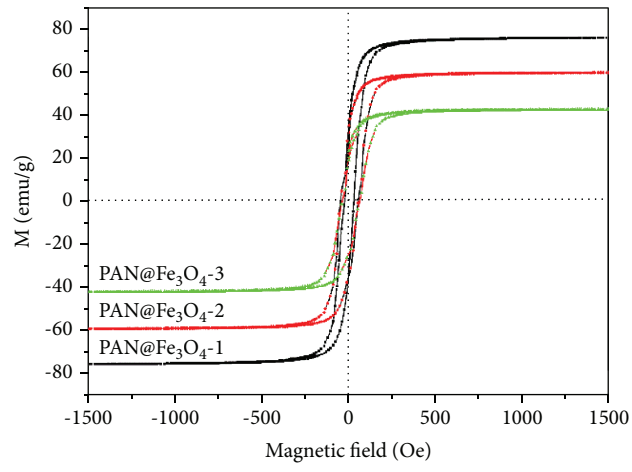

Figure 7: Magnetization curves of PAN@Fe_3O_4-1, PAN@Fe_3O_4-2, and PAN@Fe_3O_4-3.

($\mu = \mu' + j\mu''$) were measured from 0.5–18 GHz for Fe_3O_4 and PAN@Fe_3O_4 hybrids. By using the obtained permittivity and permeability, PAN@Fe_3O_4 hybrids' microwave absorption properties are calculated by using transmit line theory [23, 24]. Figure 8(a) exhibits reflection loss (RL) of Fe_3O_4; the minimum RL is −15.3, −12.7, −15.5, and −17.2 dB at 1.0, 1.5, 2.0, and 2.5 mm, respectively. Usually, the reflection loss below −10 dB indicates that 90% microwave energy is dissipated and the reflection loss below −20 dB means that 99% microwave energy is being dissipated. As the minimum reflection loss of Fe_3O_4 is higher than −20 dB, it is not good enough to be used directly.

Figures 8(b) and 8(c) show the RL of PAN@Fe_3O_4-1 and PAN@Fe_3O_4-2. The outcome shows both RL of PAN@Fe_3O_4-1 and PAN@Fe_3O_4-2 are worse than that of Fe_3O_4,

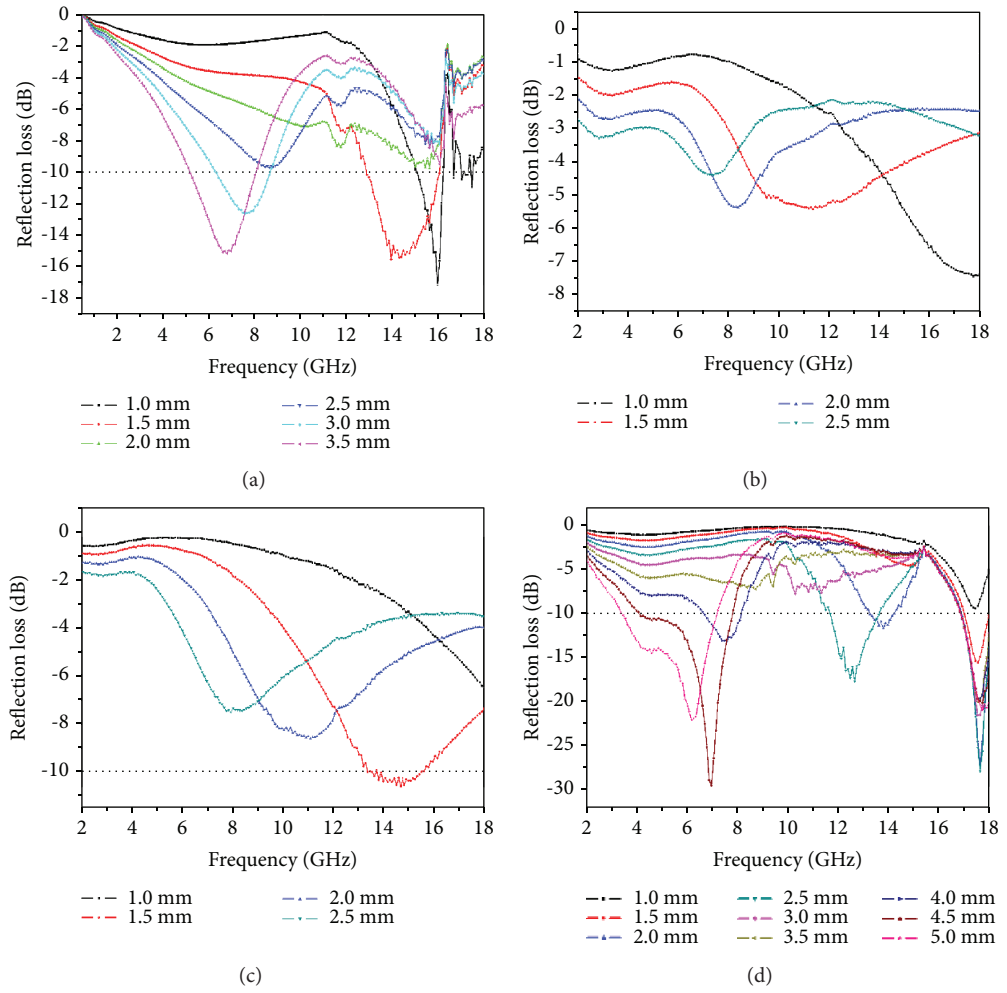

Figure 8: Reflection loss of Fe_3O_4 (a), PAN@Fe_3O_4-1 (b), PAN@Fe_3O_4-2 (c), and PAN@Fe_3O_4-3 (d).

which might be contributed to the mismatching of impedance between Fe_3O_4 and polyaniline. While for PAN@-Fe_3O_4-3, excellent microwave absorption property is obtained. As can be seen through Figure 8(d), the minimum RL of PAN@Fe_3O_4-3 is as low as −29.3 dB. The low reflection loss of PAN@Fe_3O_4-3 is due to the changeable content of polyaniline through the aniline polymerization at the spherical of Fe_3O_4. As a result, controlling the in situ aniline polymerization at the spherical of Fe_3O_4 can adjust the microwave absorption property of the obtained PAN@-Fe_3O_4 hybrids.

4. Conclusions

In conclusion, a series of polyaniline and Fe_3O_4 (PAN@-Fe_3O_4) hybrids was prepared to study their microwave absorption properties. PAN@Fe_3O_4 was fabricated by the in situ aniline polymerization at the spherical of Fe_3O_4. FTIR, XPS, and XRD measurements showed the composition of polyaniline and Fe_3O_4 in the prepared PAN@Fe_3O_4 hybrids. SEM and TEM micro images indicated the core-shell structure of the PAN@Fe_3O_4 hybrids. The TGA results suggested that the content of polyaniline in PAN@Fe_3O_4-1, PAN@Fe_3O_4-2, and PAN@Fe_3O_4-3 is 10 wt%, 16 wt%, and 23 wt%, respectively. The saturation magnetization of the PAN@Fe_3O_4 decreased with the increment of PAN content in the hybrids. The minimum reflection loss of PAN@-Fe_3O_4-3 was as low as −29.3 dB which is much better than the other samples. Controlling the in situ aniline polymerization at the spherical of Fe_3O_4 can adjust the microwave absorption of the obtained PAN@Fe_3O_4 hybrids.

Data Availability

The data used to support the findings of this study are included within the article. The funding statement will be provided in the coming revised version.

Conflicts of Interest

The authors declare that there are no conflicts of interest regarding the publication of this paper.

Acknowledgments

The financial support from the National Natural Science Foundation of China (20176169) is gratefully acknowledged.

References

[1] M. Choi, D. Choi, and J. Kim, "Magnetic permeability behaviors of FeCo micro hollow fiber composites," *Electronic Materials Letters*, vol. 11, no. 5, pp. 782–787, 2015.

[2] L. B. Kong, Z. W. Li, L. Liu et al., "Recent progress in some composite materials and structures for specific electromagnetic applications," *International Materials Reviews*, vol. 58, no. 4, pp. 203–259, 2013.

[3] T. Liu, Y. Pang, M. Zhu, and S. Kobayashi, "Microporous Co@CoO nanoparticles with superior microwave absorption properties," *Nanoscale*, vol. 6, no. 4, pp. 2447–2454, 2014.

[4] Y. Zhang, Y. Huang, T. Zhang et al., "Broadband and tunable high-performance microwave absorption of an ultralight and highly compressible graphene foam," *Advanced Materials*, vol. 27, no. 12, pp. 2049–2053, 2015.

[5] H. Wu, G. Wu, Y. Ren, L. Yang, L. Wang, and X. Li, "Co^{2+}/Co^{3+} ratio dependence of electromagnetic wave absorption in hierarchical $NiCo_2O_4$–$CoNiO_2$ hybrids," *Journal of Materials Chemistry C*, vol. 3, no. 29, pp. 7677–7690, 2015.

[6] H.-B. Zhang, Q. Yan, W. G. Zheng, Z. He, and Z. Z. Yu, "Tough graphene–polymer microcellular foams for electromagnetic interference shielding," *ACS Applied Materials & Interfaces*, vol. 3, no. 3, pp. 918–924, 2011.

[7] L. Yan, Z. Pu, M. Xu, R. Wei, and X. Liu, "Fabrication and electromagnetic properties of conjugated NH_2-CuPc@Fe_3O_4," *Journal of Electronic Materials*, vol. 46, no. 10, pp. 5608–5618, 2017.

[8] R. Wei, J. Wang, Z. Wang, L. Tong, and X. Liu, "Magnetite-bridged carbon nanotubes/graphene sheets three-dimensional network with excellent microwave absorption," *Journal of Electronic Materials*, vol. 46, no. 4, pp. 2097–2105, 2017.

[9] G. Sun, B. Dong, M. Cao, B. Wei, and C. Hu, "Hierarchical dendrite-like magnetic materials of Fe_3O_4, γ-Fe_2O_3, and Fe with high performance of microwave absorption," *Chemistry of Materials*, vol. 23, no. 6, pp. 1587–1593, 2011.

[10] Y. Zhan, X. Yang, F. Meng, J. Wei, R. Zhao, and X. Liu, "Controllable synthesis, magnetism and solubility enhancement of graphene nanosheets/magnetite hybrid material by covalent bonding," *Journal of Colloid and Interface Science*, vol. 363, no. 1, pp. 98–104, 2011.

[11] D. C. Marcano, D. V. Kosynkin, J. M. Berlin et al., "Improved synthesis of graphene oxide," *ACS Nano*, vol. 4, no. 8, pp. 4806–4814, 2010.

[12] Y. Zhan, R. Zhao, F. Meng et al., "Oriented growth of magnetite along the carbon nanotubes via covalently bonded method in a simple solvothermal system," *Materials Science and Engineering: B*, vol. 176, no. 10, pp. 779–784, 2011.

[13] R. Zhao, K. Jia, J. J. Wei, J. X. Pu, and X. B. Liu, "Hierarchically nanostructured Fe_3O_4 microspheres and their novel microwave electromagnetic properties," *Materials Letters*, vol. 64, no. 3, pp. 457–459, 2010.

[14] Y. N. Hao, X. H. Wang, S. O'Brien, J. Lombardi, and L. T. Li, "Flexible $BaTiO_3$/PVDF gradated multilayer nanocomposite film with enhanced dielectric strength and high energy density," *Journal of Materials Chemistry C*, vol. 3, no. 37, pp. 9740–9747, 2015.

[15] Z. M. Dang, L. Wang, Y. Yin, Q. Zhang, and Q. Q. Lei, "Giant dielectric permittivities in functionalized carbon-nanotube/electroactive-polymer nanocomposites," *Advanced Materials*, vol. 19, no. 6, pp. 852–857, 2007.

[16] Z. Wang, R. Wei, and X. Liu, "Dielectric properties of reduced graphene oxide/copper phthalocyanine nanocomposites fabricated through π–π interaction," *Journal of Electronic Materials*, vol. 46, no. 1, pp. 488–496, 2017.

[17] F. Jin, M. Feng, K. Jia, and X. Liu, "Aminophenoxyphthalonitrile modified MWCNTs/polyarylene ether nitriles composite films with excellent mechanical, thermal, dielectric properties," *Journal of Materials Science: Materials in Electronics*, vol. 26, no. 7, pp. 5152–5160, 2015.

[18] R. Wei, J. Wang, H. Zhang, W. Han, and X. Liu, "Crosslinked polyarylene ether nitrile interpenetrating with zinc ion bridged graphene sheet and carbon nanotube network," *Polymer*, vol. 9, no. 12, p. 342, 2017.

[19] R. Wei, K. Li, J. Ma, H. Zhang, and X. Liu, "Improving dielectric properties of polyarylene ether nitrile with conducting polyaniline," *Journal of Materials Science: Materials in Electronics*, vol. 27, no. 9, pp. 9565–9571, 2016.

[20] G. K. Elyashevich, L. Terlemezyan, I. S. Kuryndin et al., "Thermochemical and deformational stability of microporous polyethylene films with polyaniline layer," *Thermochimica Acta*, vol. 374, no. 1, pp. 23–30, 2001.

[21] S. Yu, F. Qin, and G. Wang, "Improving the dielectric properties of poly (vinylidene fluoride) composites by using poly (vinyl pyrrolidone)-encapsulated polyaniline nanorods," *Journal of Materials Chemistry C*, vol. 4, no. 7, pp. 1504–1510, 2016.

[22] R. Vijayakumar, Y. Koltypin, I. Felner, and A. Gedanken, "Sonochemical synthesis and characterization of pure nanometer-sized Fe_3O_4 particles," *Materials Science and Engineering: A*, vol. 286, no. 1, pp. 101–105, 2000.

[23] S. Sun, Q. He, S. Xiao, Q. Xu, X. Li, and L. Zhou, "Gradient-index meta-surfaces as a bridge linking propagating waves and surface waves," *Nature Materials*, vol. 11, no. 5, pp. 426–431, 2012.

[24] X. Gu, W. Zhu, C. Jia, R. Zhao, W. Schmidt, and Y. Wang, "Synthesis and microwave absorbing properties of highly ordered mesoporous crystalline $NiFe_2O_4$," *Chemical Communications*, vol. 47, no. 18, pp. 5337–5339, 2011.

Hindawi
International Journal of Polymer Science
Volume 2018, Article ID 3790834, 7 pages
https://doi.org/10.1155/2018/3790834

Research Article

Side-Chain Polyimides as Binder Polymers for Photolithographic Patterning of a Black Pixel Define Layer for Organic Light Emitting Diode

Genggongwo Shi,[1] Sung Hoon Park,[2] Jeseob Kim,[1] Minji Kim,[2] and Lee Soon Park[2]

[1]*CCTech Inc., 72, Sicheng-Ro, 721Beon-Gil, Paltan-Myeon, Haseong-Si, Gyeonggi-Do 18524, Republic of Korea*
[2]*School of Material Science and Engineering, Ulsan National Institute of Science and Technology (UNIST), Ulsan 44919, Republic of Korea*

Correspondence should be addressed to Lee Soon Park; parkls@unist.ac.kr

Received 13 April 2018; Revised 4 July 2018; Accepted 23 July 2018; Published 20 September 2018

Academic Editor: Renbo Wei

A pixel define layer (PDL) in an organic light emitting diode (OLED) is patterned using a photolithographic process before the deposition of organic layers on top of ITO anode. If the patterning of PDL on OLED panels can be achieved using a black photoresist, the patterning of black matrix (BM) on top of PDL patterns can be omitted by reducing the reflection of ambient light from OLED panels. In this study, we synthesized a series of side-chain-type polyimides as binder polymers of black photoresists and investigated the potential of using the black photoresist for the fine patterning of black PDL on OLED panels.

1. Introduction

Organic light emitting diodes (OLEDs) have become one of the major trends in the fabrication of flat panel displays because of their advantages, such as light weight, slim panels, fast response time, wide viewing angle, high resolution, and low power consumption [1-4]. The light emitting area of an OLED device is disposed at the luminous region of the pixel array on the OLED panel connected to a thin film transistor unit. Before the deposition of OLED organic layers, a pixel define layer (PDL) is patterned via a photolithographic process, as shown in Figure 1 [5-8].

Currently, positive-tone photosensitive polyimide [9, 10] is used to fabricate PDL microstructures. The corresponding PDL is yellowish brown similar to that of polyimide films. Since the yellowish-brown polyimide layer of PDL reflects the incident light, the visibility of the OLED display is reduced, particularly when used outdoors. Therefore, in the current positive-tone photolithographic process, a black matrix (BM) layer is patterned on top of the PDL pattern to improve the visibility of the OLED device (Figure 1).

If the patterning of PDL on OLED panels can be achieved using a negative-tone black photoresist [11] containing black pigment instead of the positive-tone photoresist based on photosensitive polyimide, the photolithographic process of patterning BM on top of the PDL pattern would be omitted. The required components for a typical negative-tone black photoresist include the photoinitiator, photosensitizer, multifunctional monomer, black pigment millbase, and binder polymer developable with aqueous alkaline solution. The binder polymer is crucial in the patterning of black PDL on OLED panels. It is not only one of the major components in terms of weight but also affects the shape of PDL patterns during its development in the photolithographic process. The process temperature of OLED panel fabrication reaches close to 300°C, including the postcure step after photolithographic patterning of PDL; therefore, the thermal stability of the binder polymer

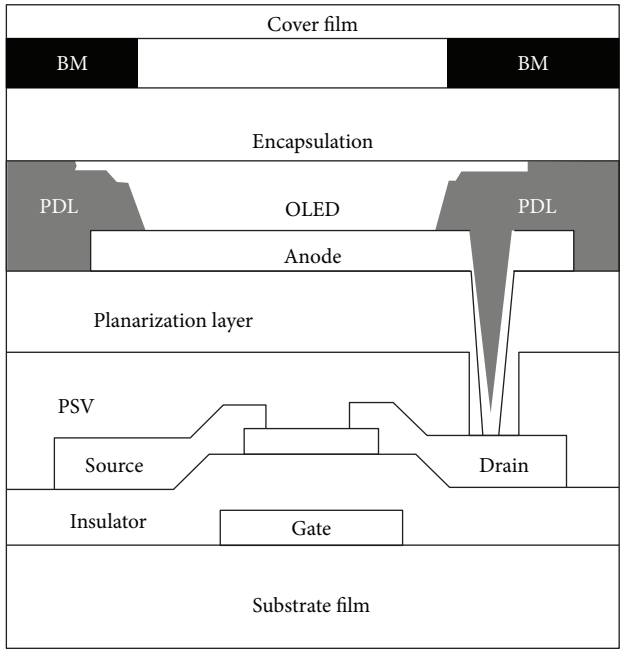

Figure 1: Typical cross-sectional view of an OLED panel.

should also be considered. Herein, new binder polymers with thermally stable imide linkages were synthesized and applied to the black photoresist formulation to pattern black PDL on OLED panels.

2. Experimental Methods

2.1. Materials and Characterization. Chemicals and solvents were reagent grades and used without further purification: poly(styrene-*co*-maleic anhydride), cumene terminated, $M_n \sim 1600$ (PSMA); 5-aminoisophthalic acid (AIPA); 3,5-bis(trifluoromethyl) aniline (6FAL); 4-aminostyrene (AS); 2-hydroxylethylacrylate (2-HEA); glycidyl methacrylate (GMA); dimethyl acetamide (DMAc); 3,5-di-*tert*-4-butylhydroxytoluene (BHT); tetrabutylphosphonium bromide (TBPB); propylene glycol monomethyl ether acetate (PGMEA); and pentaerythritol triacrylate (PETA).

Thermogravimetric analysis (TGA) was performed on a TA Instruments Q500 thermogravimetric analyzer with a programmed temperature at 10 °C/min. Fourier-transform infrared spectroscopy (FT-IR) was performed on a Varian 670/620 spectrometer using the KBr pellet method. ^{1}H NMR spectroscopy was taken on a Bruker AVANCE III HD 400 MHz spectrometer.

2.2. Synthesis of Styrene-Type Side-Chain Polyimides. PSMA (20 mmol based on maleic anhydride units) was dissolved in 20 mL of DMAc. Varying molarities of AS, AIPA, and 6FAL were added sequentially once every hour and stirred at room temperature. After the formation of amic acid linkages between maleic anhydride units of PSMA and three aromatic amines (AS, AIPA, and 6FAL), a free radical polymerization inhibitor (BHT) and a chemical imidization agent (acetic anhydride; 10 mL) were added and the reaction mixture was reacted for 4.5 h at 100 °C to afford side-chain polyimides (PSI-x) [12] (Figure 2). After cooling down, the reaction mixture was poured into excess water (>10× volume) and the precipitates were collected by centrifugation. EtOAc was added to the precipitates, and the insoluble was removed via filtration. The organic solution was washed twice using brine, dried with anhydrous Na_2SO_4, and evaporated to dryness. The solid product was washed using diethyl ether multiple times to afford PSI series side-chain polyimide as brown powder.

2.3. Synthesis of Acrylate-Type Side-Chain Polyimides. PSMA (20 mmol based on maleic anhydride units) was dissolved in 20 mL of DMAc solvent. First, 2-HEA (10 mmol) and pyridine (1 mmol) were added to the PSMA solution and the reaction mixture was stirred at room temperature for 16 h. Second, 6FAL (10 mmol) was added and stirred at room temperature for 1 h. Acetic anhydride (10 mL) was added, and the mixture was stirred at 100 °C for 4.5 h for the imidization reaction to occur (Figure 3). After the reaction, the mixture was poured into excess amount of water. The subsequent procedure was the same as that of PSI series in Section 2.2 to afford PSEI series.

2.4. Synthesis of Methacrylate-Type Side-Chain Polyimides. PSMA (20 mmol based on maleic anhydride unit) was also dissolved in 20 mL of DMAc. AIPA (6 mmol) and 6FAL (14 mmol) were added sequentially once an hour and stirred at room temperature. The reaction mixture was heated to 130 °C and stirred for 16 h [13]. After cooling down, GMA (4 mmol), TBPB (0.4 mmol), and BHT (0.04 mmol) were added and stirred at 90 °C for another 3 h (Figure 4). The reaction mixture was poured into excess water. The subsequent procedure was the same as PSI series to afford PSEA-1.

For the PSEA-2 synthesis, PSMA was dissolved in PGMEA (net. 30 wt%) instead of DMAc, and the reaction was proceeded as above with GMA.

3. Results and Discussions

3.1. Synthesis of Polyimide-Based Binder Polymers. The use of negative-tone black photoresist, instead of positive-tone photoresist based on photosensitive polyimide could remove both the BM patterning and the 1/4λ polarizing film by reducing the reflection of ambient light from the OLED panel. Positive-tone photoresist based on photosensitive polyimide is used herein because the resulting PDL made of polyimide thin film has a high thermal stability and can withstand temperatures up to 300 °C during the OLED panel fabrication process. However, the positive-tone photoresist based on photosensitive polyimide cannot be used to develop a black photoresist due to limited penetration depth of the UV light in the photolithographic patterning of black PDL on the OLED panel. The negative-tone black photoresist has deeper penetration depth than positive-tone photoresist since the photolithographic patterning is performed via a crosslinking reaction mechanism involving free

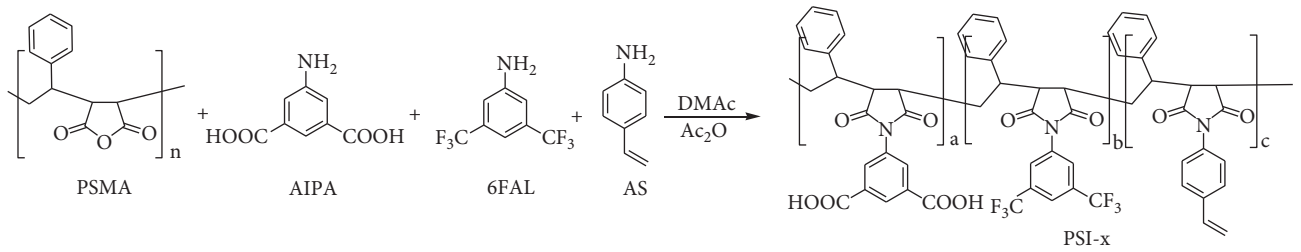

Figure 2: Synthetic scheme of styrene-type side-chain polyimides.

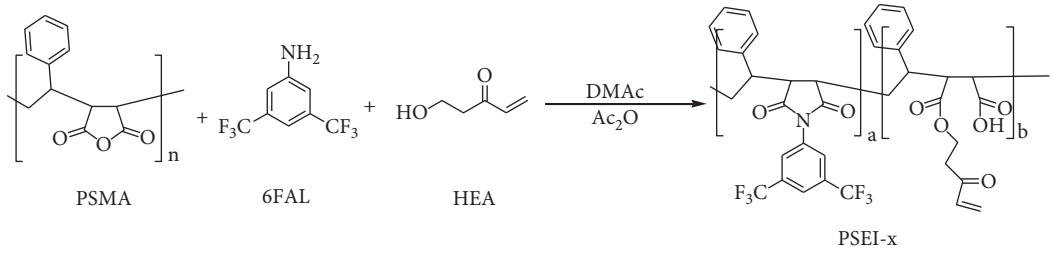

Figure 3: Synthetic scheme of acrylate-type side-chain polyimides.

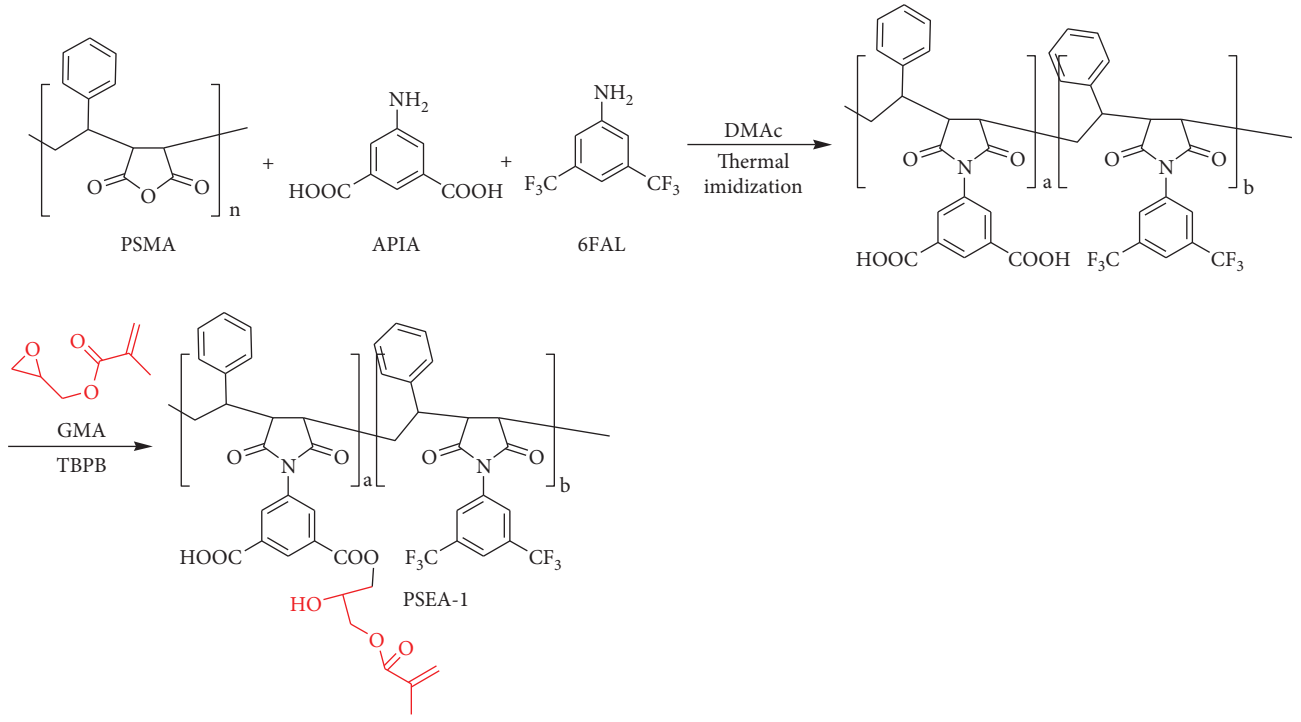

Figure 4: Synthetic scheme of methacrylate-type side-chain polyimides.

radical chain polymerization among multifunctional monomers and the binder polymer.

The binder polymer should have carboxylic groups to be developed easily with aqueous alkaline developer. Moreover, the binder polymer should also be crosslinked tightly with the multifuncional monomers upon UV light irradiation in order not to be soluble in the aqueous alkaline developer. Further, a high thermal stability of the binder polymer that corresponds to the photosensitive polyimide in the positive-tone photoresist is required. According to this guideline, three different binder polymers with thermally stable imide linkages have been synthesized.

3.1.1. PSI and PSEI Series. In the synthesis of PSI series binder polymers, three aromatic amines reacted with the maleic anhydride units of PSMA. The three amines (AIPA, 6FAL, and AS) were used to afford carboxyl groups required in the development step of photolithography. The solubility of the binder polymer in the PGMEA, a common solvent in the photoresist, was also examined. Besides, double bonds

Table 1: Synthesis of side-chain polyimides for binder polymers of black photoresists.

Binder polymer samples	Sample codes	Molarities (mmol)			Yield (%)	GPC M_w
		AS	AIPA	6FAL		
PSI series	PSI-1	4	6	10	52	4716
	PSI-2	4	8	8	44	4863
		2-HEA		6FAL		
PSEI series	PSEI-1	10	10	53	4637	
		AIPA	6FAL	GMA		
PSEA series	PSEA-1	6	14	4	56	4735
	PSEA-2	6	14	6	—	4819

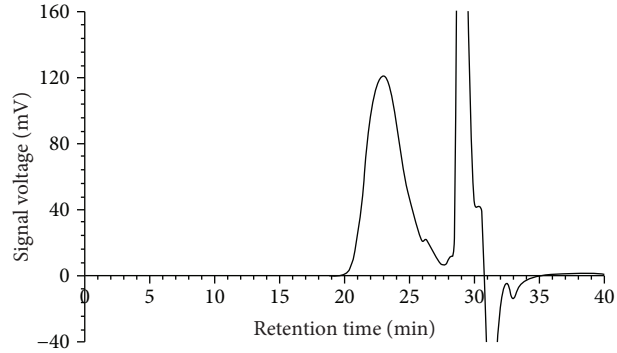

Figure 5: GPC chromatogram of PSEA-2 polyimide.

responsible for the photocrosslinking reaction were also included through the AS monomer. In the synthesis of PSI series, the chemical imidization was carried out utilizing acetic anhydride under mild condition of 100°C to avoid self-polymerization of AS via a thermal initiation mechanism. The PSI product was recovered by precipitation in excess water to remove the excess acetic anhydride followed by filtration, drying, and then tested in the black photoresist.

In PSEI series, 2-HEA was reacted with maleic anhydride units of PSMA to generate both carboxyl groups and double bonds. Then, aromatic amine (6FAL) was imidized using chemical imidization method under mild conditions. Because acetic anhydride was used for imidization, PSEI has to be worked-up in the same way as PSI series.

3.1.2. PSEA Series. PSEA series were synthesized using two different processes. First, APIA and 6FAL amines were reacted via thermal imidization with maleic anhydride groups of PSMA in DMAc solvent at 130°C. Then side-chain polyimide intermediate was reacted with GMA to afford a PSEA-1 binder polymer, in which carboxyl groups were partially converted to epoxymethacrylates. The PSEA-1 sample was recovered in the same manner as PSI series. In the second process, PSEA-2 was synthesized using PGMEA solvent instead of DMAc. However, PSEA-2 was obtained using a one-pot solution method without work-up and was tested directly as the binder polymer in the photolithographic patterning of black PDL in the OLED panel.

Table 1 shows that the yields of polyimides were not high (44%–56%) because the polyimide products had relatively high carboxyl groups and underwent weight loss during precipitation in excess water. GPC, FT-IR, and ^{1}H NMR analyses of the PSEA-2 sample are shown in Figures 5, 6, and 7, respectively. The molecular weight of PSEA-2 (M_w = 4819 g/mol) was higher than that of PSMA (M_n = 1600 g/mol) due to the expansion of hydrodynamic volume after an imidization step that introduced bulky substituents in side chains of a relatively flexible PSMA polymer. According to FT-IR spectra, anhydrides were converted to imides and methacrylate esters. Moreover, ^{1}H NMR spectrum indicated that electron-poor aromatic amines (δ 8.18–8.45), epoxy (δ 4.16), and methacrylate groups (δ 1.87–1.96, 5.66, and 6.07) were introduced to PSMA chains.

3.2. Photolithography and Thermal Stability of Black PDL Patterns. The black photoresist for the patterning of the black PDL of OLED panel is composed of the photoinitiator, photosensitizer, multifunctional monomer, polyimide as a thermal stabilizer, black millbase, and binder polymer. The binder polymer and multifunctional monomer are the main components of the photoresist, which affect the exact patterning of PDL via the photocrosslinking reaction in the UV-irradiated area and development of UV-unirradiated area by aqueous alkaline solution.

In this study, a commercial binder polymer SR-6300 (SMS Co., Korea) known as cresol novolac epoxyacrylate, dissolved in PGMEA solvent at 30 wt%, was used as a reference binder polymer as shown in Table 2. A commercial sample PETA was used as multifunctional monomer, which has the functionality of 3. The thermal stability of the reference black photoresist (PT-0), determined by TGA, was not high enough (up to 300°C) to endure the photolithographic patterning of PDL even after the subsequent postcure treatment at 250°C for 30 minutes.

Figure 8 shows the photolithographic patterns of the black PDL using the side-chain polyimide binder polymers. The black photoresists PT-0 and PT-3 exhibited fine patterns of black PDL. However, PT-1 and PT-2 showed irregular or wavy PDL patterns. In case of PT-1 photoresist PSI type binder polymer had styrenic groups as source of double bonds for the photocrosslinking reaction, so that the adhesion to the silicon wafer was not as good as the reference binder polymer (SR-6300), which has epoxy acrylate as a source of double bonds. In the case of the PT-2 black photoresist, the wavy PDL pattern was related to the high acid value of the binder polymer PSEI-1 in which acrylate groups were introduced via the reaction of 2-HEA with maleic anhydride units of PSMA. High amount of 2-HEA monomer had to be used for the complete solubility of the resulting PSEI-1 in PGMEA. The PT-3 black photoresist showed fine PDL patterns due to the balance of good adhesion to the silicon wafer and the optimum acid value from benzoic acid-type carboxyl groups.

The effect of side-chain polyimide binder polymers on the thermal stability of the resulting PDL patterns was evaluated via TGA analysis. The black PDL patterns formed on the silicon wafer were scratched off after photolithographic

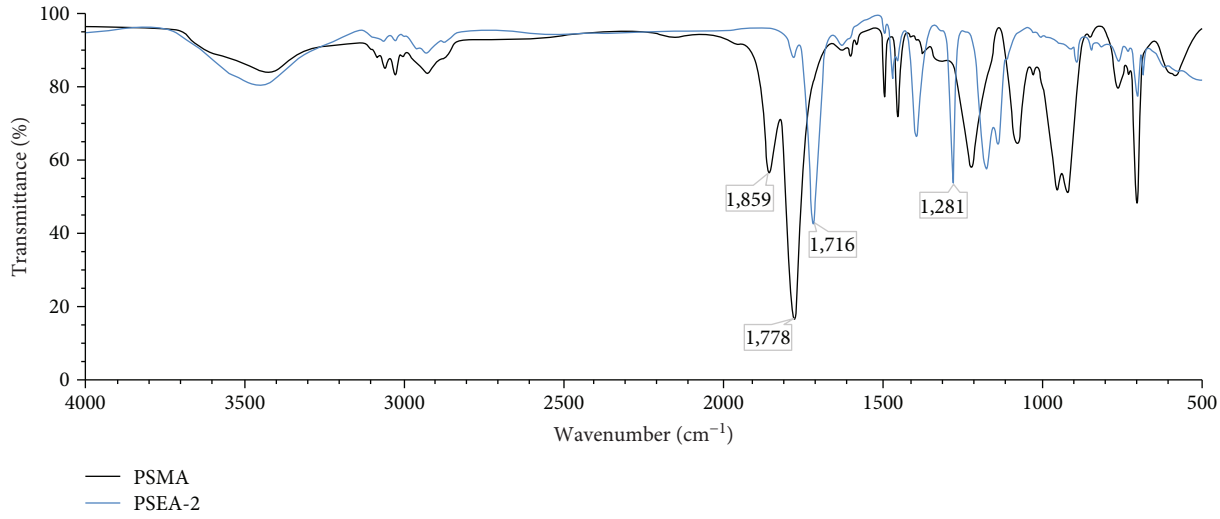

Figure 6: FT-IR charts of PSEA-2 and its starting material PSMA.

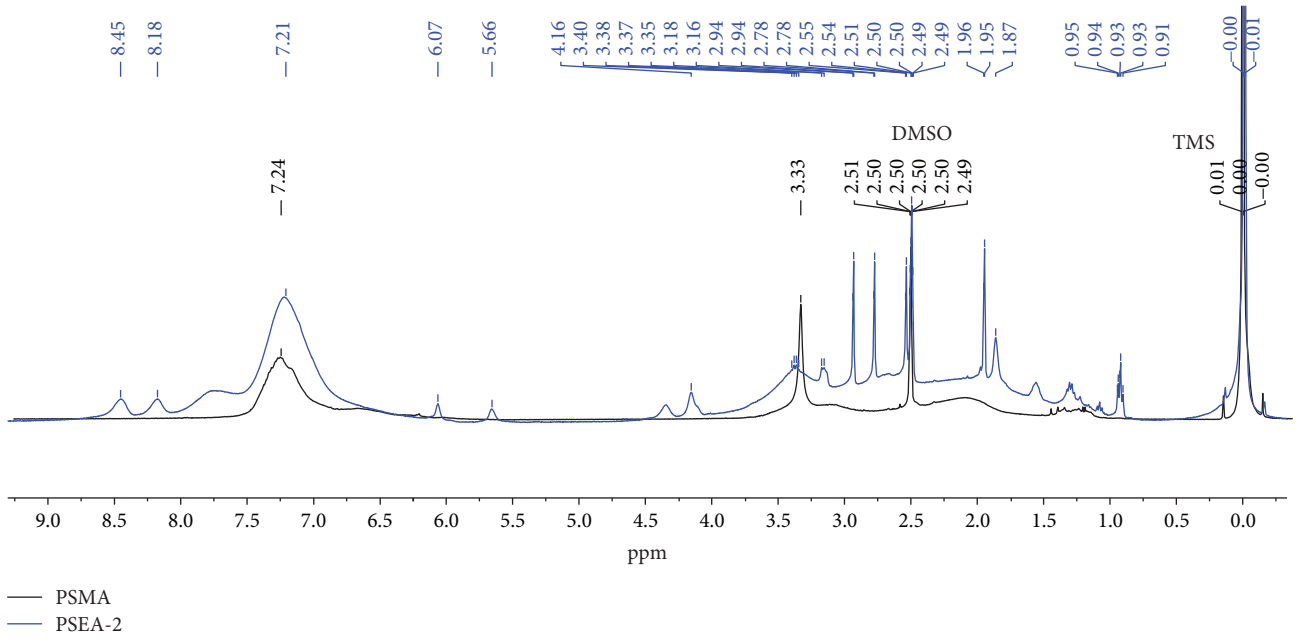

Figure 7: ^{1}H NMR diagrams of PSEA-2 and its starting material PSMA in d_6-DMSO.

patterning using a sharp razor blade, and the fine black powder was subjected to TGA analysis. As shown in Table 2 and Figure 9, the PT-3 photoresist having thermally stable side-chain polyimide PSEA-2 as a binder polymer exhibited higher 1 wt% loss temperature than the PT-0 reference photoresist which had commercial SR-6300 as binder polymer.

4. Conclusion

In this study, a series of new binder polymers having thermally stable side-chain imide linkages were synthesized and used in the black photoresist formulation to pattern black PDL on the OLED panel. For the synthesis of binder polymers, poly(styrene-*co*-maleic anhydride) was used as the starting material and three different types of side-chain polyimides were obtained. The epoxy methacrylate-type side-chain polyimide afforded a fine black PDL pattern with high thermal stability, comparable to that of the currently used positive-tone photosensitive polyimide.

Data Availability

The data used to support the findings of this study are available from the corresponding author upon request.

Table 2: Formulation of black photoresists and thermal stability of a black PDL pattern [14].

Components/photoresist samples		PT-0	PT-1	PT-2	PT-3
Photoinitiators	Irgacure 754	1	1	1	1
	Irgacure TPO	6	6	6	6
Photosensitizer	Darocure ITX	2	2	2	2
Binder polymer (30 wt% in PGMEA)	SR-6300	35			
	PSI-2		35		
	PSEI-1			35	
	PSEA-2				35
Multifunctional monomer	PETA	8	8	8	8
Polyimide thermal stabilizer (30 wt% in PGMEA)	MY-10	10	10	10	10
Black millbase (23 wt% in PGMEA)	LT-1 (SKC htm Co., Korea)	35	35	35	35
Solvent	PGMEA	5	5	5	5
Total	wt%	100	100	100	100
Thermal stability	1 wt% loss temp. (°C, TGA)	282	—	—	303

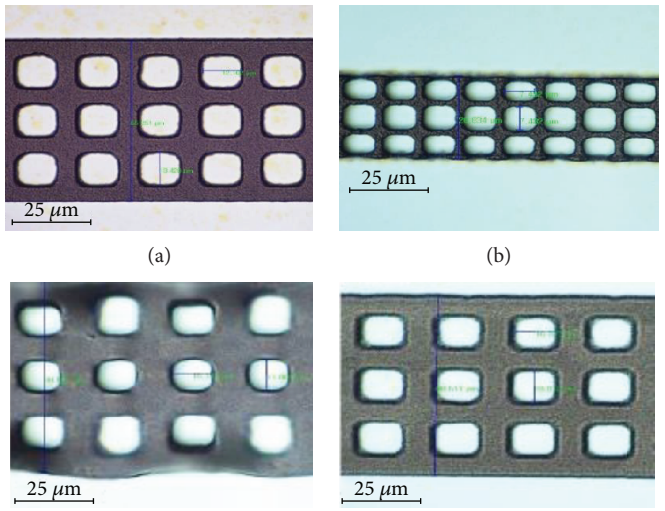

Figure 8: The optical microscopic images of black PDL patterns obtained with (a) PT-0, (b) PT-1, (c) PT-2, and (d) PT-3 black photoresists.

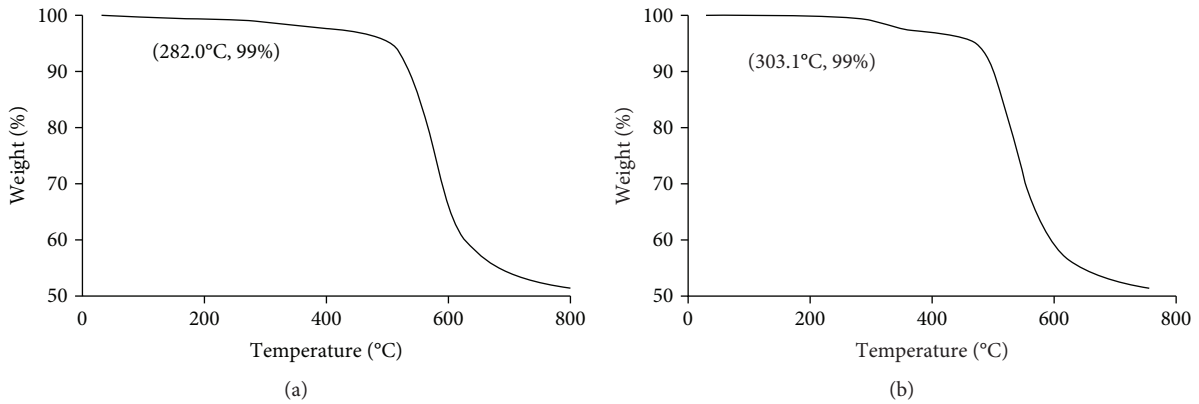

Figure 9: TGA thermograms of black powders obtained from the black PDL patterns. (a) PT-0 and (b) PT-3.

Disclosure

Part of this work's content will be used on "The 18th International Meeting on Information Display (IMID)" to be held on Aug. 29, 2018.

Conflicts of Interest

The authors declare that they have no competing interests.

Acknowledgments

This study was supported by the Technology Innovation Program (or Industrial Strategic Technology Development Program) (10063289, Development of High Temperature Negative Tone Photosensitive Black Resin and Fabrication Process for Pol-less AMOLED Devices) funded by the Ministry of Trade, Industry & Energy (MOTIE, Korea).

References

[1] J. K. Lee, S. Cho, and D. W. Kang, "Analysis of light leakage between the adjacent pixels in a color-filter stacked white OLED display," *Displays*, vol. 45, pp. 6–13, 2016.

[2] M. Kim and G. H. Jin, "ITO/AlNdN/Al contact process for active matrix OLED displays," *Electronics Letters*, vol. 45, no. 8, p. 421, 2009.

[3] M. Noda, N. Kobayashi, M. Katsuhara et al., "47.3: a rollable AM-OLED display driven by OTFTs," *SID Symposium Digest of Technical Papers*, vol. 41, no. 1, p. 710, 2010.

[4] W. Liu, C. Jiang, D. Wang, and Y. Li, "Organic light-emitting diode (OLED) display panel, pixel define layer (PDL) and preparation method thereof," 2016, U.S. Patent 9373814 B2.

[5] D. J. Liaw, K. L. Wang, Y. C. Huang, K. R. Lee, J. Y. Lai, and C. S. Ha, "Advanced polyimide materials: syntheses, physical properties and applications," *Progress in Polymer Science*, vol. 37, no. 7, pp. 907–974, 2012.

[6] S. Tamai, A. Yamaguchi, and M. Ohta, "Melt processible polyimides and their chemical structures," *Polymer*, vol. 37, no. 16, pp. 3683–3692, 1996.

[7] J. A. Defranco, B. S. Schmidt, M. Lipson, and G. G. Malliaras, "Photolithographic patterning of organic electronic materials," *Organic Electronics*, vol. 7, no. 1, pp. 22–28, 2006.

[8] M. Aleksandrova, "Specifics and challenges to flexible organic light-emitting devices," *Advances in Materials Science and Engineering*, vol. 2016, Article ID 4081697, 8 pages, 2016.

[9] K.-i. Fukukawa and M. Ueda, "Recent progress of photosensitive polyimides," *Polymer Journal*, vol. 40, no. 4, pp. 281–296, 2008.

[10] Y. Tsuda, Y. Matsuda, and T. Matsuda, "Soluble polyimides bearing long-chain alkyl groups on their side chainviapolymer reaction," *International Journal of Polymer Science*, vol. 2012, Article ID 972541, 10 pages, 2012.

[11] C.-K. Lee, T.-M. Don, D.-J. Lin, C.-C. Chen, and L.-P. Cheng, "Characterization of acrylic copolymers applied in negative-type photoresist via a ternary composition diagram," *Journal of Applied Polymer Science*, vol. 109, no. 1, pp. 467–474, 2008.

[12] H.-C. Yu, J. W. Jung, J.-Y. Choi, and C.-M. Chung, "Kinetic study of low-temperature imidization of poly(amic acid)s and preparation of colorless, transparent polyimide films," *Journal of Polymer Science: Part A*, vol. 54, no. 11, pp. 1593–1602, 2016.

[13] E. Pyun, R. J. Mathisen, and C. S. P. Sung, "Kinetics and mechanisms of thermal imidization of a polyamic acid studied by ultraviolet-visible spectroscopy," *Macromolecules*, vol. 22, no. 3, pp. 1174–1183, 1989.

[14] S. H. Park, G. Shi, D. M. Seo, M. Kim, J. Kim, and L. S. Park, "Synthesis of multifunctional monomers for patterning pixel define layer of organic light emitting diode," *Molecular Crystals and Liquid Crystals*, vol. 663, no. 1, pp. 168–173, 2018.

Hindawi
International Journal of Polymer Science
Volume 2018, Article ID 5161908, 15 pages
https://doi.org/10.1155/2018/5161908

Review Article

Polyarylene Ether Nitrile-Based High-*k* Composites for Dielectric Applications

Yong You, Chenhao Zhan, Ling Tu, Yajie Wang, Weibin Hu, Renbo Wei, and Xiaobo Liu

Research Branch of Advanced Functional Materials, School of Materials and Energy, University of Electronic Science and Technology of China, Chengdu 610054, China

Correspondence should be addressed to Renbo Wei; weirb10@uestc.edu.cn and Xiaobo Liu; liuxb@uestc.edu.cn

Received 6 April 2018; Accepted 4 June 2018; Published 10 July 2018

Academic Editor: Atsushi Sudo

Flexible polymer-based composites exhibiting high dielectric constant as well as low dielectric loss have been intensively investigated for their potential utilization in electronics and electricity industry and energy storage. Resulting from the polar -CN on the side chain, polyarylene ether nitrile (PEN) shows relatively high dielectric constant which has been extensively investigated as one of the hot spots as dielectric materials. However, the dielectric constant of PEN is still much lower than the ceramic dielectrics such as $BaTiO_3$, TiO_2, and Al_2O_3. In this review, recent and in-progress advancements in the designing and preparing strategies to obtain high-*k* PEN-based nanocomposites are summarized. According to the types of the added fillers, the effects of organic fillers, dielectric ceramic fillers, and conductive fillers on electric properties of PEN-based composites are investigated. In addition, other factors including the structures and sizes of the additive, the compatibility between the additive agent and the PEN, and the interface which affects the dielectric properties of the obtained composite materials are investigated. Finally, challenges facing in the design of more effective strategies for the high-*k* PEN-based dielectric materials are discussed.

1. Introduction

Designing and fabrication of novel advanced electronic materials feeding for the rapid development of information technology has attracted considerable attention for their applications as integrated and portable electronic devices [1, 2]. Miniaturization, portability, and high performance of these materials are the guiding directions for the development of highly integrated components [3–6]. Capacitor, as an important energy storage device, is the most common electronic devices fabricated by dielectrics with high-*k*, high breakdown strength, high-energy density, but low loss tangent [7, 8]. Among these parameters, relative permittivity and loss tangent are the most significant ones which can be easily obtained by researchers and/or manufacturing workers to evaluate the final properties when used in electronic and electrical applications [9–11]. Traditional dielectric materials include oxides (ZnO, Al_2O_3, etc.) [12, 13] and ferroelectric ceramic materials such as (TiO_2, $BaTiO_3$, etc.) [14, 15]. The dielectric constant of oxides is generally below 50, which is not high enough to be used in capacitors. In comparison, the dielectric constant of ferroelectric ceramics can be as high as 10^4 with extremely low dielectric loss and excellent thermal stability, which meets the requirements of most application devices [16, 17]. These ferroelectric ceramic dielectrics exhibiting relatively higher permittivity have attracted tremendous research enthusiasm because of their applications as power transmission system, high-energy storage capacitor, microwave communication, and so on [18–20]. However, to fulfil demands from the electronic industry, it is still a challenge with critical importance to fabricate lightweight and portable equipment with these inorganic dielectric materials. First of all, the density of inorganic materials makes it difficult to meet the requirements of lightweight and portable devices. Secondly, most inorganic dielectric materials require high sintering temperature, which is not conducive to the preparation of materials, energy conservation, and environmental protection. Thirdly, it is difficult to realize the bending and flexibility of large curvature due to the structural characteristics of the inorganic material. Finally, the poor corrosion resistance to acid and alkali limits its application in some special fields [21–23].

In comparing with the inorganic materials, high-performance polymers and polymer-based composites (organic materials) show the characteristics of lightweight, flexibility, and resistance to acid and alkali as well as easy processing [24, 25]. As a result, these organic materials are tremendously studied as dielectrics to replace the inorganic materials [26–28]. However, the relatively low permittivity of polymer limits its further utilization as dielectrics. Fortunately, the relative permittivity of the polymer can be effectively improved through the introduction of fillers [24]. At present, the fabrication of polymeric composite dielectrics showing high-k, low loss tangent, low density, and good mechanical properties is of great significance to the preparation of new energy storage elements [25].

The polymer-based composites are two component, three component, and/or multicomponent [29, 30] mixtures consisting of polymer matrix and additives. As for the polymer matrix, polymeric dielectric materials are widely used in various fields of social production and life resulting from their easy processing and high dielectric strength. Up to now, polyimide (PI), polyethylene (PE), and polyvinylidene fluoride (PVDF) as well as many other polymers have been employed to fabricate capacitors [31–34]. However, resulting from their relative low T_g, the polymeric dielectrics including PE and PVDF cannot work continuously at atmospheres higher than 160°C. The present solution, which uses additional thermal management systems to cool the devices, is impracticable in low-cost and large-scale applications. As a result, candidates with higher T_g are imperative [35]. Polyarylene ether nitrile (PEN), a high-performance thermoplastic polymer, has been intensively studied because of its excellent performances including thermal stability, easy processing, radiation resistance, and excellent mechanical performances as well as chemical resistance [36–38]. In addition, resulting from the polar -CN on the side chain, PEN shows relatively high dielectric constant. Basing on these novel properties, PEN has shown its application as dielectrics at high-temperature environments in automotive and electronic industries [39, 40].

In order to obtain composites having high permittivity, various kinds of fillers, including ferroelectric ceramics, conductive nanoparticles, and organic dielectrics, are incorporated into the polymer matrix [41, 42]. Usually, the higher permittivity of the used additives, the better permittivity of the obtained composites [14, 17]. As a result, the most used additives include the high-permittivity ferroelectric ceramics and the conducting fillers [15, 16, 30]. Maxwell-Wagner polarization indicates that the permittivity of the composite increases obviously when the content of the filler reaches a critical value (percolation threshold) [14]. Unfortunately, the loss tangent of the system increases simultaneously due to the incompatibility between the organic substrate and the inorganic additives. As a result, the micromorphology of fillers, the distribution mode of the additives in the polymeric substrate, surface treatment, and preparation methods of the fillers (i.e., "core-shell" nanoarchitectures) [43–46] are equal important as the kind of fillers that determines the properties of the obtained composites [47–51]. This article reviews the progress of PEN-based composites exhibiting high-k for electric applications. Furthermore, the feasible methods to improve permittivity and reduce loss tangent of the composites are emphatically analyzed.

2. PEN Matrix

At present, some kinds of polymer dielectric materials such as biaxial tensile polypropylene and polyester are used in civil fields. Although they have shown excellent dielectric properties, these dielectric materials can only maintain the stability of various performance under 160°C [52, 53], which is far from meeting some high-tech applications, such as aerospace and new energy vehicles. Therefore, the high-k material with high thermal stability has aroused the interest of researchers. It is well known that PEN is a high-performance thermoplastic engineering resin owing to the high mechanical behavior, thermal stability, easy processing, radiation resistance, and corrosion resistance [54–58].

PEN matrix was usually prepared via the reaction of nucleophilic substitution polymerization synthesized by 2,6-dichlorobenzonitrile and aromatic diphenols under the catalysis of potassium carbonate, which has widely reported in previous work [54]. The associated synthesis route is shown in Figure 1. It can be seen the strong polarity group of -CN in the side of macromolecular chain of PEN, and the main chain contains a large number of rigid aromatic rings. In addition, there is a free rotational -O- (ether bond) in the main chain. Therefore, these characteristics endow the PEN with excellent tensile strength, tensile modulus, chemical stability, and radiation resistance [56]. The performance parameters of the first industrial PEN ID-300 [59] are shown in Table 1.

Besides, with the development of polymerization methods, the PEN is not limited to the homopolymer of PEN mentioned above. Professor Liu's group has prepared a series of random copolymers and block copolymers of PEN [60], which greatly enriches the variety of PEN meeting different application requirements of the modern society. What is more, with nearly 40 years of development, the series of PEN can be divided into amorphous PEN, semicrystalline PEN, and crystalline PEN according to its crystallinity, and it can also be divided into noncross-linked PEN and cross-linked PEN according to the cross-linking of the system.

3. High-k PEN Composites

High permittivity of the materials is the basic property for their application as capacitors. Although the ceramic material exhibits high-k, it is also hard to suit current requirements for the development of energy storage elements. The development of polymer-based composite containing polymer matrix and additives as dielectric material is one of the technical routes to solve this problem. Combining flexibility and lightweight of polymer matrix with high-k of additives, the polymer-based composites are endowed with specific properties, such as high-k, lightweight, and easy-to-process [61, 62]. On the basis of the type of additives, the polymer composite dielectric materials were divided into polymer-

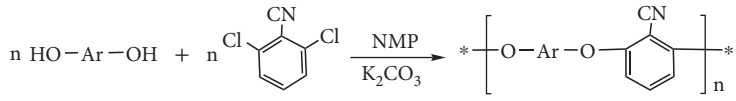

where representative–Ar–can be any of these groups:

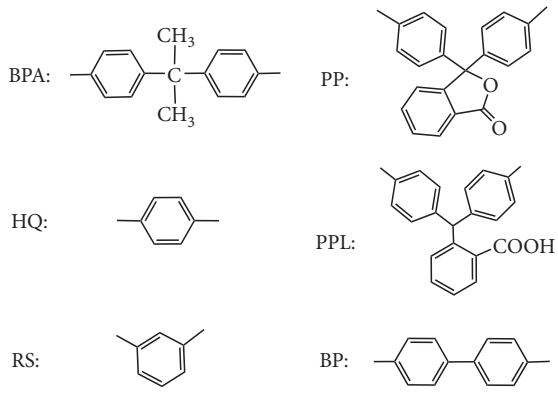

Figure 1: Synthesis route of PEN.

Table 1: Properties of PEN ID-300.

Product property	Performance parameter
Thermal properties	Glass transition temperature (T_g) is 145°C; hot deformation temperature is 165°C; continuous use temperature is 230°C
Mechanical properties	Tensile strength is 123 MPa; breaking elongation is 15%; tensile modulus is 2.3 GPa
Dielectric properties	Dielectric constant is about 3.5; dielectric loss is 0.08–0.01 (1 kHz)
Corrosion resistance	Resistance to organic solvents, alkaloids, ketones, and hydrocarbons excepted sulfuric acid

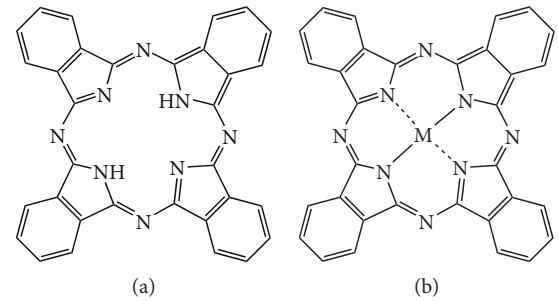

Figure 2: Structures of phthalocyanines (a) and metal phthalocyanines (b).

based composite dielectric materials filled with organic fillers, ceramic fillers, conductive fillers, among others.

3.1. High-k PEN Composites with Organic Fillers. The advantage of organic filler is that it exhibits good compatibility with polymer matrix and is easily to be dispersed uniformly in PEN matrix to obtain homogenous composite material. The organic filler/PEN composite dielectric materials show excellent mechanical properties and are suitable for preparation of composite thin film with high-k. Phthalocyanines (Pcs) have highly coplanar 18 electronic π-bonded conjugate structures and can react with a number of metal ions to form metal phthalocyanine (MPcs), as shown in Figure 2. Meanwhile, the axis and edge of phthalocyanine ring can connect many kinds of special functional active substituent, its structure modification makes these compounds with physical and chemical properties [63]. As a classic organic semiconductor, the dielectric constant of copper phthalocyanine (CuPc) is up to 10^5 [64]. The dielectric permittivity and loss tangent of PEN/CuPc nanocomposite materials are about 45 and 0.4 at 1 kHz, respectively [65]. When the filler mass fraction of CuPc is up to 40 wt%, the PEN/CuPc composites still maintain good mechanical properties. In addition, the surface treatment of CuPc by chemical modification is an effective way to improve the dispersion of fillers and polymer, decrease the dielectric permittivity-frequency dependence, and reduce the loss tangent of the composites significantly. On the other hand, phthalocyanine-containing polymers, prepared by self-polymerization and/or self-assembly of Pcs, not only possess the unique physical and chemical properties of Pcs, but also combine good solubility and processability of polymers [66].

Beside the Pcs, organic compounds which can form Pc after cross-linking are also introduced into PEN matrix to make PEN composites. Yang et al. [67] prepared 1,3,5-tri-(3,4-dicyanophenoxy) benzene (TPh) through a reaction with the phloroglucinol and 4-nitro-phthalonitrile and then prepared the PEN/TPh composite materials which presented high dielectric permittivity, low loss tangent, and high heat resistance. Furthermore, the phthalocyanine rings can be formed by self-cross-linked through the -CN group in pendants or in the end of macromolecular chain of PEN [68], which can improve the dielectric properties and thermal stability of the composites. As shown in Figure 3, when PEN matrix was mixed with TPh, the dielectric permittivity of the obtained samples after cross-linking at high temperature is much higher than that of films without cross-linking. It is

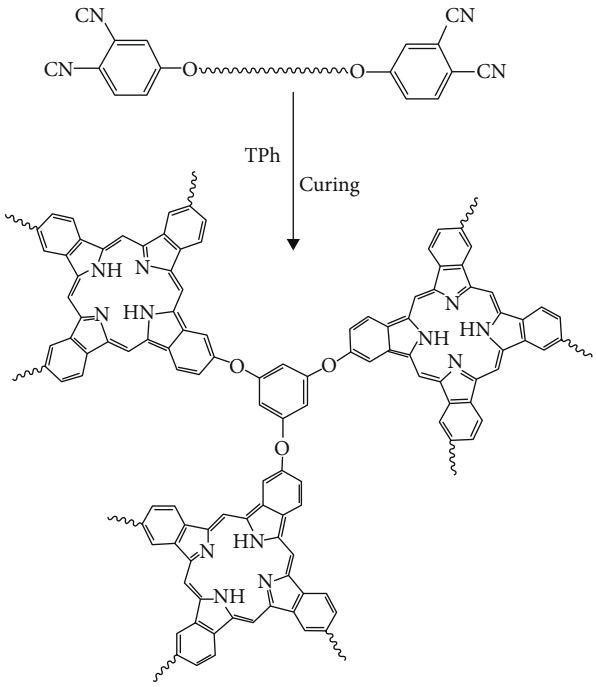

Figure 3: Formation of phthalocyanine rings from PEN and TPh.

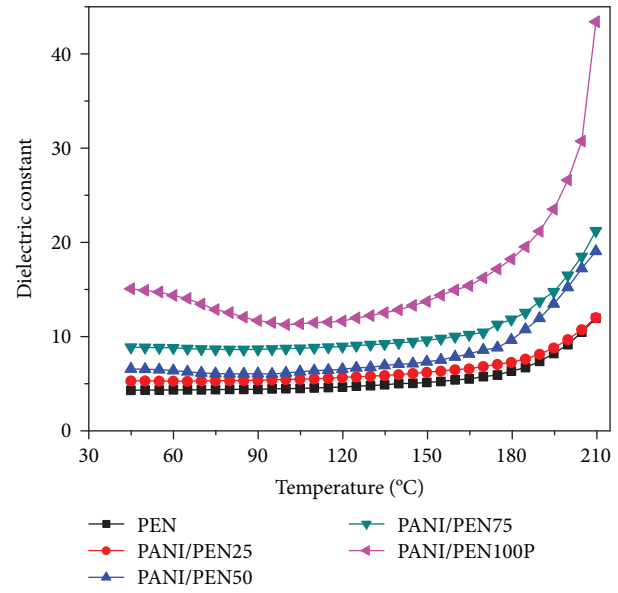

Figure 4: Dielectric permittivity-temperature dependences of PEN/PANI composites at 1 kHz. (PEN, PANI/PEN25, PANI/PEN50, PANI/PEN75, and PANI/PEN100 represent the composites with 0, 2.5, 5.0, 7.5, and 10 wt% of PANI, resp.).

because that the phthalocyanine rings were formed during the cross-linking which increased the dielectric permittivity of the samples. Besides, the formation of cross-linking network contributed to the low loss tangent. More importantly, the microscopic structures of the obtained PEN/TPh system have a big change after self-cross-linking, and the homogeneous phrases were formed gradually from phrase separation. The properties above make the PEN/TPH composites show a great potential for application in some extreme environment [67].

High-k polymers can be also treated as fillers to increase the dielectric properties of polymers. Long et al. [69] reported that the polyvinylidene fluoride (PVDF) and PEN polymer alloys with different mass ratios were prepared successfully by solution casting method. For PVDF/PEN alloy (with 90 wt% PVDF), it can be seen that the dielectric permittivity has a slight decrease from 7.1 to 5.8 (1 kHz) with the frequency from 25 Hz to 1 MHz, which presented a week dependence of dielectric constant and frequency. Besides, it is also found that the dielectric permittivity and loss tangent of PVDF/PEN alloy (with 90 wt% PVDF) increase slowly from 7 and 0.02 to 18 and 0.05 (1 kHz) before the melt point of PVDF, which indicated that the PVDF/PEN alloys have a relatively stable dependence of dielectric permittivity and temperature.

Moreover, the organic conducting polymeric materials are also used as additives to fabricate high-k polymer-based composite materials. Wei et al. [70] investigated that the polyaniline (PANI) was doped with sulfuric acid as a filler to prepare PEN/PANI composite films for improving the dielectric permittivity of PEN by using solution casting method. It is clearly seen that there was just a T_g of the composites on DSC curves, and no phase separation was observed on the SEM images. All these indicated that the PANI has a well compatibility with the PEN matrix. Besides, the dielectric permittivity of PEN-based composite film presented a sostenuto increase with the increment of PANI content. When the content of PANI is 10 wt%, the dielectric permittivity of the PEN/PANI composite film is 23.5 at 250 Hz, which increases by 650% by comparing to pure PEN matrix. The dielectric properties indicated that the PANI can enhance the dielectric permittivity of PEN effectively. In addition, the PEN/PANI composites have a relatively stable dependence of dielectric permittivity and temperature before 180°C (Figure 4).

3.2. High-k PEN Composites with Ceramic Fillers. Apart from organic fillers, selection of high-k dielectric ceramic fillers of different types and shapes improves the dielectric permittivity of PEN-based composites effectively. It is well known that the dielectric permittivity of ferroelectric ceramics can be as high as 10^4 with extremely low dielectric loss and excellent thermal stability. PEN-based composites with high-k are easily prepared after the incorporation of these ferroelectric ceramics. However, due to the poor compatibility between the polymer matrix and the fillers, the loss tangent of the composites will increase dramatically without modification. As a result, the micromorphology of fillers, the dispersion mode of the fillers in resin matrix, surface treatment, and preparation methods are equal important as the kind of fillers that affect the dielectric properties of PEN composites.

3.2.1. Ceramic Nanoparticles as Fillers. The mostly used high-k ceramics are barium titanate ($BaTiO_3$) [41], strontium titanate ($SrTiO_3$) [71], titanium dioxide (TiO_2) [14], calcium titanate ($CaTiO_3$) [72], among others. Ceramic additives serve as insulators due to high bandgap, and accumulation

of charges can only take place under a certain electric field. Besides, it is crucial for the improvement of the dielectric constant of polymer-based composites in interfacial area between the polymer matrix and fillers. What is more, the dielectric permittivity of the ceramic additives is much higher than the resin matrix, and the dielectric permittivity of polymer-based composites is enhanced with the increment of the filler content which leads to an increment in the interfacial area of polymer matrix and fillers [73]. Especially, the relationship between dielectric permittivity and filler content is increasing linearly. As a result, the content and size of ceramic particles are two important matters affecting the electrical characteristics of the obtained polymer-based composites [74].

(1) Effect of Filler's Content. Every barber knows that the dielectric permittivity of the polymer-based composites increases with the increase of ceramic filler content. Hence, the dielectric permittivity of polymer matrix can be obtained 10–20 times by filling in high-proportion ceramic particles (>50%, volume fraction). Tang et al. [75] reported that the PEN/BT nanocomposites were prepared through the ultrasonic dispersion fabrication process. The dielectric constant of PEN/BT nanocomposites increased from 4.07 to 12.55 at 1 kHz with the content of BT nanoparticles increased from 0 wt% to 40 wt%. Besides, although the dielectric permittivity of the PEN-based nanocomposites decreases with the increase of frequency, the dependence of the frequency and dielectric permittivity is reduced. However, the high content of ceramic fillers will make the particles unfavorable to uniform dispersion in the resin matrix, which leads to the agglomeration of the additives and formation interfacial voids and pores [76]. This would drastically reduce the mechanical strength and breakdown strength of polymer-based composites. Therefore, the breakdown strength of PEN/BT nanocomposites decreased rapidly from 231.48 to 158.07 kV/mm with the content of fillers increased from 0 wt% to 40 wt%.

(2) Effect of Filler's Size. The size of filler is another important factor affecting electrical properties of ferroelectric ceramics/polymer composites. Besides, the performance of particle has a close relationship with the filler's size, which is usually presented as the smaller the filler's size is, the larger the specific surface area is. When additives with micron size or larger are introduced into polymer matrix, defects are easily formed which results in the electric field distortion in composite materials. At the same time, the local electric field will be enhanced by the void and porosity caused by agglomeration of the additives in the polymer-based composites. All these defects reduce the breakdown strength and mechanical strength of the composites. In comparison, the nanosized filler can effectively enhance mechanical properties of polymer-based composites and increase the amount of the ceramic fillers filled in the matrix. Theoretically, the dielectric permittivity of polymer-based composites increases with the decrease of filler particle size. It is mainly because that the use of small particle size fillers will increase the interface area among polymer resin and filler, which enhanced interface polarization causing by the increment of the electron density on the interface [77, 78].

3.2.2. Core-Shell-Structured Ceramic Nanoparticles as Fillers. Dispersion and compatibility of fillers within the polymer substrate are the most important parameters that determine the dielectric properties of the polymer-based composites. When the additives are heterogeneously distributed within the polymeric substrate, defects and voids which obviously reduce the mechanical strength and dielectric constant of the system emerge easily. As the PEN contains oleophilic groups, while the surfaces of fillers tend to have hydrophilic groups, such as -OH and -COOH, it is extremely easy to produce local reunion causing by incompatibility of them when the filler is blended with the polymer matrix directly. As a result, there are still some challenges before achieving desirable composites even although the use of nanoparticles shows some advantages in designing high-permittivity polymer composites. These challenges include achieving homogeneous dispersion, tailoring the nanoparticle interface within polymer matrix, among others, which are the key points to realize composites with desired dielectric property. In order to solve these problems, the fabrication of core-shell-structured particles with organic shells is usually adopted.

(1) Core-Shell-Structured Ceramic Nanoparticles. Polymer-based nanocomposites with high-k have shown application as dielectrics in energy storage due to their intrinsic properties including lightweight and easy processing. To achieve applications of the additives in enhancing dielectric properties of the system, many researchers prepared core-shell-structured additives, which are effective tool for the fabrication novel high-permittivity polymer-based composites [43]. At the early stage, many surfactants, oligomers, and small molecules were used to improve the compatibility of the two-phase interface by using the weak electrostatic interaction between molecules or van der Waals force to form a shell layer [79, 80]. However, at the filler's surface, the physical adsorption of these molecules cannot form a stable interface, resulting in the low dielectric strength and high dielectric loss. Therefore, stronger forces such as chemical bond and/or hydrogen bond, through which a more stable interfacial layer can be formed between the inorganic additive and the polymeric substrate, are needed. Generally, the introduced chemical bond not only reduces the defects at the interface, but also improves the physical property of the system. What is more, the chemical bond between the interfaces can keep the composites stable in the electric field and force field. In addition, phase separation is effectively stopped with the existence of chemical bond between additives and polymeric substrate [81].

Taking $BaTiO_3$ as a representative, Figure 5 presents a general method in preparing high-permittivity polymer composites using core-shell-structured additives. Combining the rotary coating technology with a posttreatment bonding process, Tang et al. [82] reported a new method to prepare $BaTiO_3$@CPEN core-shell-structured nanoparticles. The CPEN shell is carboxyl-functionalized polyarylene ether nitrile on which the carboxyl groups react with the hydroxyl

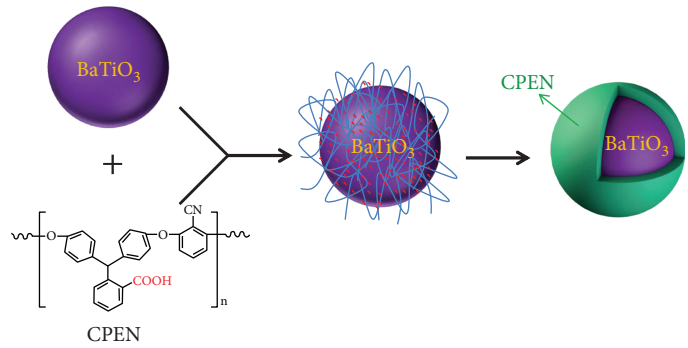

Figure 5: Synthetic route for the core-shell-structured $BaTiO_3$/CPEN nanoparticles.

groups on the surface of $BaTiO_3$. The TEM results showed that the $BaTiO_3$ core was wrapped by the CPEN shell completely, and the thickness of the CPEN shell was in the range of 4–7 nm. Then, the $BaTiO_3$@CPEN and PEN composite films with different contents of $BaTiO_3$@CPEN were fabricated through the solution casting method. The dielectric permittivity of pristine PEN is 4.3, while it gradually raises with the addition of $BaTiO_3$@CPEN. When the content of $BaTiO_3$@CPEN is 40 wt%, the dielectric permittivity of the obtained composite is as high as 13.5, which is about 3 times compared with the PEN. The dielectric loss increases a little with the addition of $BaTiO_3$@CPEN, but it keeps lower than 2.3% even plenty of additives were added. It is because that the CPEN shell at $BaTiO_3$@CPEN has the similar structure with the PEN substrate, the compatibility between the CPEN and PEN results in the homogeneous dispersion of $BaTiO_3$@CPEN in PEN substrate which decreases the interfacial polarization, and thus, a low dielectric loss system was obtained. Similarly, Huang et al. [83] prepared a series of surface-modified titanium dioxide (TiO_2@CPEN) and PEN composites with different mass contents of TiO_2@CPEN by using a similar method. TiO_2 nanoparticles were completely wrapped by CPEN and formed the core-shell structures. The modified TiO_2 nanoparticles were uniformly distributed in the PEN substrate due to the existence of the CPEN shell. Moreover, the TiO_2@CPEN particles did not display any signs of evulsion in the PEN substrate, resulting from the fact that the interaction between PEN and the interface of TiO_2@CPEN particles is quite strong. The result indicated that permittivity of the TiO_2@CPEN/PEN composite increases linearly with the increasing content of surface-modified TiO_2 particles. When TiO_2@CPEN nanoparticle content is 40 wt%, permittivity of the obtained TiO_2@CPEN/PEN nanocomposite at 1 kHz reaches 7.9, while loss tangent of the system is also below 3% (1 kHz).

(2) Core-Shell-Shell-Structured Ceramic Nanoparticles. At present, "molecular bridge" is the main method to realize the dispersion of the core-shell-shell-structured filler in the polymer substrate. The key point of the "molecular bridge" is the introduction of the inner shell acting as the buffer layer connecting both the core and the external shell. The buffer layer acts as molecular bridge forming bonds between inorganic and organic polymers. Comparing with physical adsorption, this kind of modification has better effect and can effectively reduce the agglomeration of inorganic additives in the polymeric substrate. The mostly used buffer layer is silane coupling agent, which is a kind of low molecular organosilicon compounds with special structure [84]. Other functional materials such as carboxyl-functionalized polymers and sulfonyl-functionalized polymers are also widely used as the buffer layer [85].

Tang et al. [84] reported the preparation of core-shell-shell-structured nanoparticles $BaTiO_3$@SiO_2@HBCuPc and then fabricated its composites with PEN as substrate. $BaTiO_3$@SiO_2@HBCuPc was obtained by reaction between hyperbranched copper phthalocyanine (HBCuPc) and $BaTiO_3$@SiO_2 which were prepared through surface modification of $BaTiO_3$ with silane coupling agent KH550. What is more, combining the coating with bonding technology, You et al. [85] reported the preparation of core-shell-shell-structured nanoparticles $BaTiO_3$@CPEN@CuPc with carboxyl-functionalized polyarylene ether nitrile (CPEN) as the buffer layer. The preparation of $BaTiO_3$@CPEN@CuPc nanoparticles is shown in Figure 6. In the first step, the $BaTiO_3$ was coated with CPEN through the interaction between the carboxyl at CPEN and the hydroxyl on the surface of $BaTiO_3$. Then, the other carboxyl at CPEN reacted with the amino groups at copper phthalocyanine (CuPc). The core-shell-shell-structured nanoparticles $BaTiO_3$@CPEN@CuPc were incorporated into the PEN substrate to fabricate $BaTiO_3$@CPEN@CuPc/PEN composites. Their result showed that the permittivity of the $BaTiO_3$@CPEN@CuPc/PEN composites is stable in the measured frequency. When the $BaTiO_3$@CPEN@CuPc is 20 wt%, the permittivity of the $BaTiO_3$@CPEN@CuPc/PEN composite at 1000 Hz is up to 9.0, with an increment of 130% compared with that of PEN substrate. The increasing of the permittivity can be explained by the formation of microcapacitors in the composite system, and the more the additives are added, the more the microcapacitors are formed [86]. In comparing with $BaTiO_3$/PEN, $BaTiO_3$@CPEN@CuPc/PEN shows higher permittivity at the same content of the additive. This is because the better compatibility between $BaTiO_3$@CPEN@CuPc and PEN as well as the high permittivity of the CuPc. Meanwhile, the compatibility of the $BaTiO_3$@CPEN@CuPc with the PEN substrate contributes to the low dielectric loss. The dielectric loss of $BaTiO_3$@CPEN@CuPc/PEN films at 1000 Hz is only 3.1% with the nanofiller content up to 20 wt%. Another result they obtained is that the

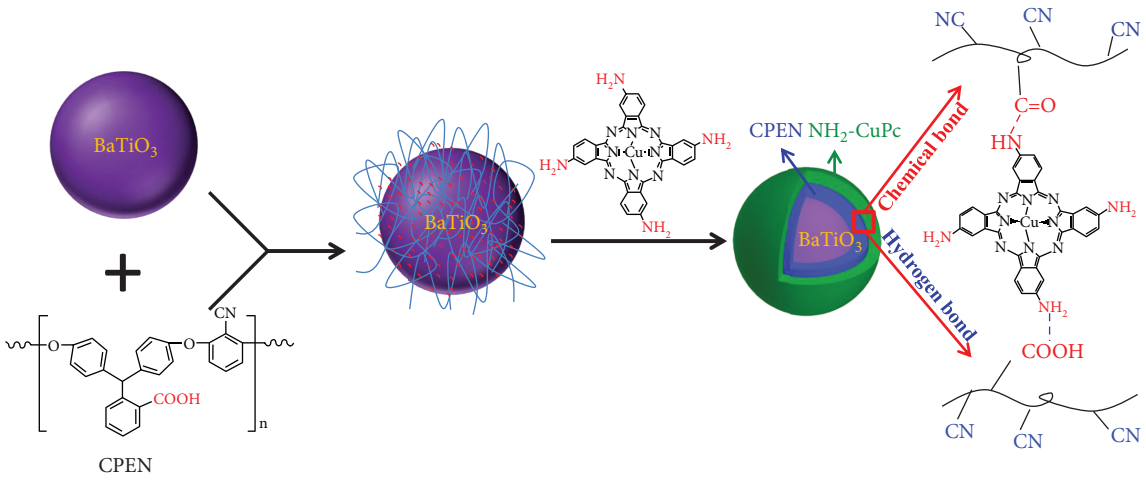

Figure 6: Synthetic route for the core-shell-shell-structured nanoparticles.

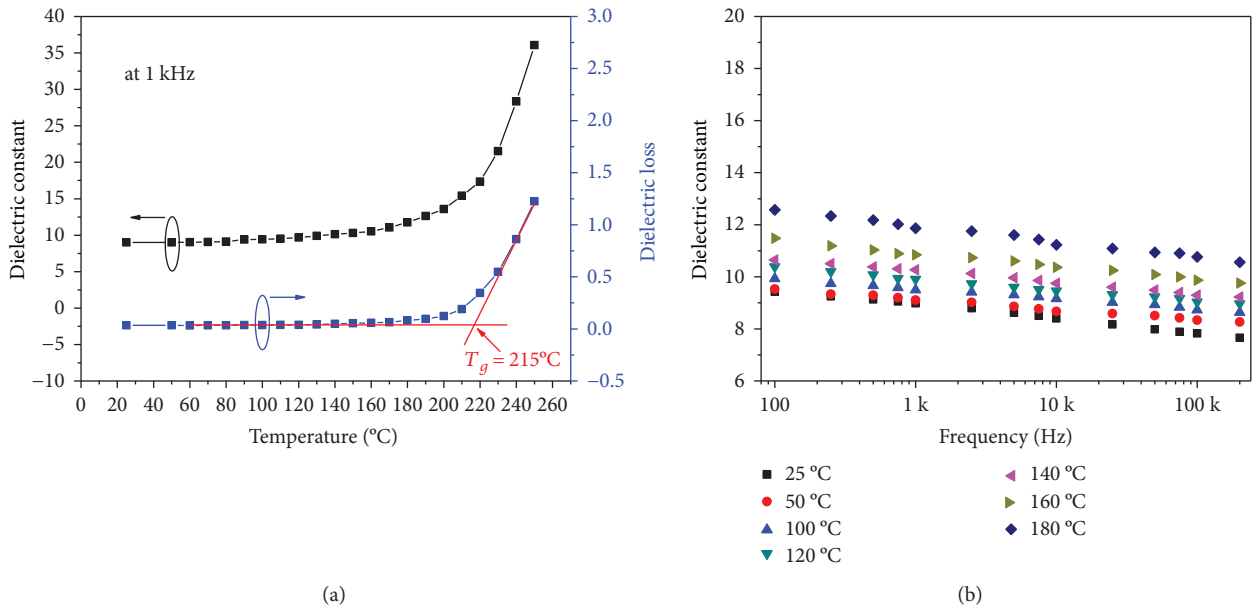

Figure 7: The permittivity-frequency properties of BT@CPEN@CuPc/PEN (20 wt%).

permittivity and the dielectric loss of the $BaTiO_3$@CPEN@-CuPc/PEN composite are quite stable when the temperature is lower than its T_g (>200°C), while both of them increase abruptly when the temperature is nearby or even higher than its T_g. In addition, stable permittivity of $BaTiO_3$@CPEN@-CuPc/PEN composite at different temperatures (25–180°C) is also observed within the measured frequency, as shown in Figure 7.

In summary, the direct recombination and "molecular bridge" are the main methods to prepare the core-shell nanoparticles. Through the fabrication of the core-shell-structured nanoparticles, it is possible to adjust the parameters such as thickness of the shell, compatibility between the additive and the polymeric substrate, interface interaction, among others, which affect the final properties of the obtained high-permittivity composites.

3.3. High-k PEN Composites with Conductive Fillers. Compared with PEN composites with dielectric ceramic fillers, which usually need larger volume fraction of filler, the dielectric constant of the composite increases obviously with the addition of less conductive filler. Usually, the more the additives are added, the more the microcapacitors are formed which increase the permittivity of the system. When the conductive additives are used as the fillers, the microcapacitors can be easily formed at a lower content of the additives. As a result, the percolation threshold of the conductive additives is achieved at lower filler volume fraction, meaning the permittivity increases easily with less conductive additives.

There are many kinds of conductive fillers. Common metal conductive particles (i.e., Ag, Ni, and Al) [87] are the mostly used additives in preparing composites with high dielectric permittivity. Besides, the conductive carbon

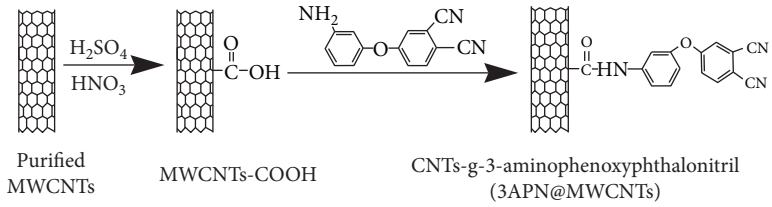

Figure 8: Schematic illustration of preparation of 3-APN@MWCNTs.

nanomaterials including carbon nanotube (CNT), carbon black, graphene, and graphene oxide (GO) represent another kind of widely studied conductive fillers [88, 89]. However, the volume fraction window of the composite material from dielectric to conductive material is closed to the threshold value. It is very important to control the amount of conductive fillers and to disperse them evenly. Otherwise, the conductive path will be formed locally in the material, which will increase the dielectric loss. In addition, it will also cause the energy dissipation and reduce the service life of the composites. Therefore, how to evenly disperse these conductive additives in organic polymer substrate becomes the key step in improving properties of this kind of composite materials.

3.3.1. Metal Conductive Particles as Fillers. At present, some different types of metal conductive particles have been utilized to enhance the permittivity of organic polymers [90, 91]. Through the in situ reduction of silver ion during the compositing process, Li et al. [87] reported Ag nanoparticles and PEN composite (Ag/PEN). The corresponding Ag/PEN composite films were obtained through solvent casting technique. The silver nanoparticles exhibit as nanospheres in the PEN substrate at fractions lower than 1.0 wt%, and they grow to be nanorods when more silver ion is added as the reactant. More importantly, the in situ reduced silver nanoparticles are homogeneously embedded in the PEN substrate even though the silver nanoparticles are unmodified. When 2.0 wt% of silver nanoparticles are embedded in the system, the permittivity increases to 5.8 at 1000 Hz, while the loss tangent keeps lower than 2%. What is more, with the formation of the silver nanoparticles in the system, the electric conductivity increases obviously. As less than 2.0 wt% of silver nanoparticles are embedded in the system, this kind of PEN composite can be used as antistatic materials.

3.3.2. Carbon Nanotubes (CNTs) as Fillers. Carbon nanotubes (CNTs) are monolayer or multilayer coaxial hollow tubular carbon nanotubes (CNTs) with carbon atom SP2 hybrid bonding, forming delocalized π bonds. The conjugation effect of CNTs is remarkable. Besides, CNTs, as one-dimensional nanomaterials, exhibit fascinating properties including excellent mechanical strength, outstanding thermal conductivity, ultrahigh electrical capacity, and thermal stability [92, 93]. Due to these charming properties, CNTs have been widely adopted in substituting or replenishing traditional nanofillers to prepare composites with different functions. Zheng et al. [94] prepared composite films by using 4,4′-dihydroxybiphenyl-based PEN as the organic substrate and multiwalled carbon nanotubes (MWCNTs) as additives. The permittivity of the obtained mixture increases from 4.3 to 6.1 (1 kHz) with the content of MWCNT fillers increases from 0 wt% to 3 wt%, exhibiting little frequency dependence with the incorporation of MWCNTs. Besides, the loss tangent of the composites increases from 0.010 to 0.026 (1 kHz) with the content of MWCNT fillers increases from 0 wt% to 3 wt%, which is caused by the incompatibility of MWCNTs with the organic PEN substrate.

Usually, the van der Waals interaction of the CNTs leads to the self-aggregation. As a result, the CNTs tend to aggregation, which impedes the enhancing of dielectric properties, rather than homogeneously distribution in the organic polymer substrate [95]. In order to overcome these defects, surface modification of CNTs and the controlling of interaction between the modified CNTs and polymeric substrate are the effective methods for the high-k polymer nanocomposites. Jin et al. [96] modified the CNT's surface by grafting organic molecules to enhance compatibility between CNT and PEN substrate. For this purpose, acidulated MWCNT was reacted with amino containing molecule 3-aminophenoxyphthalonitrile (3-APN) through solvothermal to form the modified carbon nanotube (3-APN@MWCNT) (Figure 8). After that, the modified carbon nanotube (3-APN@MWCNT) was utilized as an additive in preparing 3-APN@MWCNT/PEN nanocomposites with high permittivity. When 5.0 wt% of 3-APN@MWCNT is loaded, the permittivity of the obtained 3-APN@MWCNT/PEN nanocomposite at 50 Hz is 32.2, about 8 times to that of the PEN substrate. In addition, the loss tangent is lower than 0.9. Both permittivity and loss tangent increase linearly with the increasing of 3-APN@MWCNT at low loading. 3-APN@MWCNT shows a percolation threshold of 4.0 wt% in the system as the dielectric parameters raise obviously at higher loading. Pu et al. [97] fabricated modified CNT with phthalonitrile groups (CNT-CN) and used it as additive in preparing PEN-based composites. The CNT-CN distributed in the PEN substrate is uniformly due to the plenty of phthalonitrile groups, which are compatible with the nitriles on PEN, at the peripheral surface of it. In addition, the phthalonitriles at CNT-CN react with the nitriles on the main chain of PEN catalyzed by diaminodiphenyl sulfone (DDS) at high temperature, forming triazine rings. As a result, the permittivity can be as high as 33.9 when reacted at 320°C for 4 h.

In addition, core-shell-heterostructured CNT-based nanomaterials are also widely applied to obtain composites with high dielectric constant. Huang et al. [98] reported the preparation of core-shell-heterostructured CNT-based nanomaterials MWCNT@$BaTiO_3$, in which MWCNT acts as core and inorganic $BaTiO_3$ serves as shell, through solvothermal

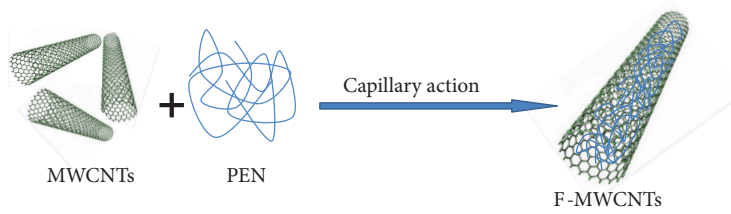

Figure 9: Schematic illustration of fabrication of F-MWCNTs.

reaction. After that, they fabricated MWCNT@$BaTiO_3$/PEN composite through solution casting. The permittivity increases to 13.8 at 100 Hz, with an increment higher than 200%, at the loading of 50.0 wt% of MWCNT@$BaTiO_3$. What is more, Huang et al. also prepared MWCNT@TiO_2 core-shell-heterostructured CNT-based nanomaterials via similar reaction [99]. Tetragonal anatase-phased TiO_2 clusters were formed at the peripheral surface of MWCNT. Besides acting as the additive, this core-shell-heterostructured MWCNT@TiO_2 can be used as microwave absorption materials due to its excellent electromagnetic performances.

Furthermore, You et al. [88] and Xiao et al. [100] reported the opening of MWCNTs' end offering O-MWCNTs which could be utilized as nanoscale vessels. PEN was then filled in the O-MWCNTs through capillary action to obtain F-MWCNTs (the schematic illustration of F-MWCNTs is shown in Figure 9). The PEN filled in the restricted CNT vessel shows extraordinary crystallization behavior in comparing with the crystallization at unrestricted conditions. The F-MWCNTs were also incorporated into the PEN substrate to prepare corresponding composites. The dielectric constant of PEN at 10 kHz is 4.02, and it increases after F-MWCNT is incorporated. The dielectric constant reaches 5.33 (10 kHz) for F-MWCNT/PEN when the concentration of MWCNT is 1.0 wt%. Although the dielectric losses of the composites increase with the increment of the additives, they are around 0.011. Therefore, the incorporation of the F-MWCNT into PEN is an effective approach to design dielectrics with high permittivity and low loss tangent.

3.3.3. Graphene Oxide (GO) and/or Graphene as Fillers. Graphene, a microscale 2D lattice carbon with one atomic thickness, has shown extraordinary electric property [101]. As a result, it can be used as conducting additives in the fabrication of multifunctional high-*k* polymeric dielectrics. On the other hand, graphene exhibits ultra large specific surface area of 2630 m^2/g deriving from its unique structure features. Therefore, microcapacitors, which further improve the dielectric property, can be formed easily when the microsheets are isolated by the polymeric substrate in graphene-based composites. Up to now, graphene has shown its widely application in fabrication of composites with high permittivity. Wang et al. [102] prepared reduced graphene oxide (RGO) and PEN composites (RGO/PEN) through in situ thermal reduction of corresponding graphene oxide (GO) and PEN composites (GO/PEN). GO/PEN was simply fabricated by solution casting process due to the excellent dispersion of GO in solvent like NMP. After thermal reduction, GO transfers into RGO which was uniformly distributed as that of GO in GO/PEN. When 6.0 wt% of RGO is loaded, the permittivity of the final RGO/PEN increases to 129.1 with an increment of about 2600%. In addition, the permittivity of the composite with 2.0 wt% of GO also shows a 230% increment at 50Hz when GOtransforms to RGO after thermal reduction.

Similar to CNT, graphene is insoluble in most solvents due to its all-carbon composition and hydrophobic nature. It is difficult to apply on a large scale due to its poor dispersion in polymer matrixes. Therefore, it is necessary to functionalize it to change the surface energy of the graphene and thus solving the aggregation of graphene sheets in the composite [103, 104]. Up to now, the mostly utilized procedure to modify graphene is firstly disposing it with strong oxidizers to obtain GO and then reducing it back to RGO after the composting process [105–107]. Li et al. [108] prepared GO and then functionalized it with CuPc, offering GO@CuPc, through solvothermal reaction. Then, the GO@CuPc was added into the PEN substrate to prepare high-*k* nanocomposites. When 5.0 wt% of GO@CuPc was loaded in the system, the dielectric constant reaches 52.0 (at 100 Hz). Zhan et al. [109] also prepared GO and firstly reported the chemical modification of it using 4-aminophenoxyphthalonitrile (4-APN), forming (GO-CN). After that, the GO-CN was successfully introduced into PEN substrate to prepare nanocomposite films. As the phthalonitriles at GO-CN show compatibility with PEN, this route opens a new way in preparing graphene and PEN composites. What is more, Wang et al. [110] fabricated composite with GNs-Fe_3O_4 hybrid material as additive and PEN as organic substrate. The GNs-Fe_3O_4 hybrid material was prepared via solvothermal reaction from GO and $FeCl_3$ with ethylene glycol as the reducer.

Moreover, novel 3D CNT and graphene networks were also constructed to prevent the aggregation of them. Wei et al. [111] firstly fabricated 3D CNT-GO networks by coordinating them with metal ions (Cu^{2+}, Zn^{2+}, and others), forming GO-Zn-CNT. After that, a semi-interpenetrating system (GO-Zn-CNT/PEN-Ph) was obtained by penetrating a cross-linkable polyarylene ether nitrile (PEN-Ph) into the GO-Zn-CNT networks. An interpenetrating network (GS-Zn-CNT/PEN) was finally fabricated via simultaneously cross-linking of PEN-Ph and in situ thermal reduction of GO. The fabrication route for the GS-Zn-CNT/PEN is shown in Figure 10. The dielectric constant of GS-Zn-CNT/PEN is as high as 78.0 at 100 Hz, with an increment of 2000% in comparison with PEN, even the content of GO-Zn-CNT is just 2.0 wt%. Besides, the loss tangent of GS-Zn-CNT/PEN

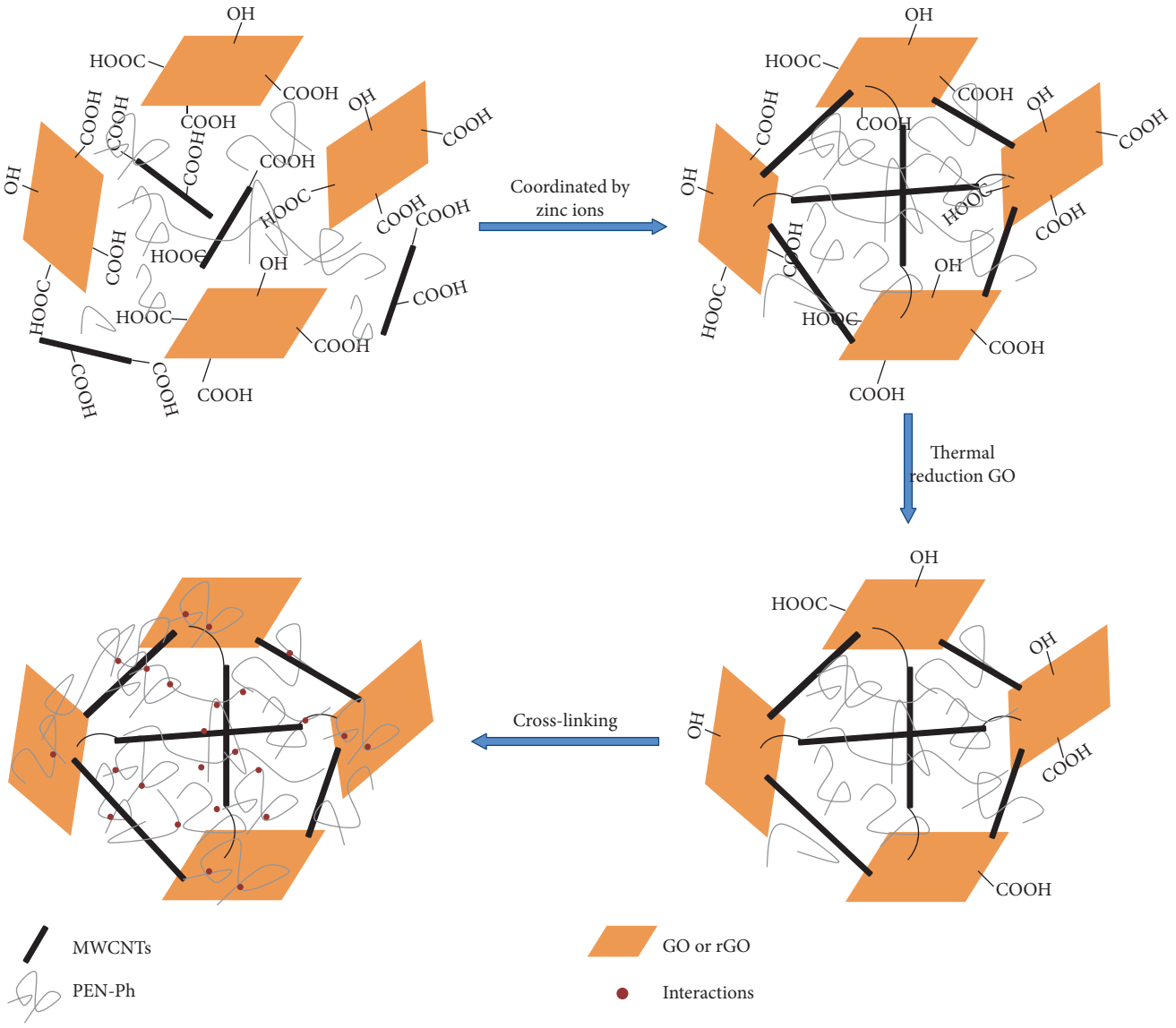

Figure 10: Fabrication route for GS-Zn-CNT/CPEN.

is 0.18 at 100 Hz when the content of GO-Zn-CNT is 2.0 wt%, but it is much lower compared with that of graphene/PEN nanocomposites (0.82 at 100 Hz with 2.0 wt% graphene). Therefore, it is also an effective method to prepare graphene-based high-k composite materials.

4. Conclusions

In conclusion, high-k dielectrics for high-energy storage need to possess high permittivity, low dielectric loss, and excellent mechanical strength as well as high thermal stability. Up to now, there is not any single-component dielectric meeting the mentioned requirement for high-temperature applications. The composting of thermal stable PEN with high dielectric constant additives (such as organic fillers, ceramic fillers, and conductive fillers) is an efficacious technique for the development of thermal resisting high-k dielectrics. Although some important progresses have been made in the research of PEN-based composite dielectric materials in recent years, it still cannot fully meet the development of the electronic industry. This research news article mainly reviews the progress of PEN-based composites for electronic applications. It preliminarily revealed the effects of polymer substrate, type of filler, surface modification, and preparation procedure on PEN composites' dielectric properties. To sum up, the PEN incorporated with organic fillers exhibits relative high permittivity, low loss tangent, excellent mechanical strength, and thermal stability, but the improvement of permittivity is inadequate because of the limited permittivity of these organic fillers. Ferroelectric ceramics can effectively enhance permittivity of PEN-based nanocomposites. However, a high loading fraction is usually needed, which reduces the mechanical performances of the system simultaneously. In comparison, dielectric constant of PEN composites filled with conductive fillers could be significantly increased at lower filling fraction. However, the conductivity of the

composites was also improved, which leads to the corresponding high dielectric loss. As a result, the research and preparation of high-k dielectric materials still face many challenges, which are the goal of future efforts. Further research can be carried out in the following aspects: firstly, preparing the new additives with controllable structure, morphology, size, and so on and exploring some new and simple compositing technology and interface control technology and secondly, researching and developing dielectric composite materials with stable performance in special environments such as high temperature and frequency. Thirdly, fabricating high-k composites exhibits high permittivity, low loss tangent, and other required performances simultaneously with controllable procedures.

Conflicts of Interest

The authors declare that there is no conflict of interest regarding the publication of this paper.

Authors' Contributions

Yong You and Chenhao Zhan contributed equally to this work.

Acknowledgments

The financial supports from the National Natural Science Foundation of China (51603029 and 51773028), the China Postdoctoral Science Foundation (2017M623001), and the National Postdoctoral Program for Innovative Talents (BX201700044) are gratefully acknowledged.

References

[1] J. K. Yuan, S. H. Yao, Z. M. Dang, A. Sylvestre, M. Genestoux, and J. Bai, "Giant dielectric permittivity nanocomposites: realizing true potential of pristine carbon nanotubes in polyvinylidene fluoride matrix through an enhanced interfacial interaction," *The Journal of Physical Chemistry C*, vol. 115, no. 13, pp. 5515–5521, 2011.

[2] L. Qi, B. I. Lee, S. Chen, W. D. Samuels, and G. J. Exarhos, "High-dielectric-constant silver-epoxy composites as embedded dielectrics," *Advanced Materials*, vol. 17, no. 14, pp. 1777–1781, 2005.

[3] T. Kousksou, P. Bruel, A. Jamil, T. el Rhafiki, and Y. Zeraouli, "Energy storage: applications and challenges," *Solar Energy Materials and Solar Cells*, vol. 120, pp. 59–80, 2014.

[4] R. M. Dell and D. A. J. Rand, "Energy storage — a key technology for global energy sustainability," *Journal of Power Sources*, vol. 100, no. 1-2, pp. 2–17, 2001.

[5] Y. Wang and Y. Xia, "Recent progress in supercapacitors: from materials design to system construction," *Advanced Materials*, vol. 25, no. 37, pp. 5336–5342, 2013.

[6] Z. M. Dang, L. Wang, Y. Yin, Q. Zhang, and Q. Q. Lei, "Giant dielectric permittivities in functionalized carbon-nanotube/electroactive-polymer nanocomposites," *Advanced Materials*, vol. 19, no. 6, pp. 852–857, 2007.

[7] W. H. Xu, G. Yang, L. Jin et al., "High-k polymer nanocomposites filled with hyperbranched phthalocyanine-coated BaTiO3 for high-temperature and elevated field applications," *ACS Applied Materials & Interfaces*, vol. 10, no. 13, pp. 11233–11241, 2018.

[8] M. A. Alam, M. H. Azarian, and M. G. Pecht, "Effects of moisture absorption on the electrical parameters of embedded capacitors with epoxy-$BaTiO_3$ nanocomposite dielectric," *Journal of Materials Science: Materials in Electronics*, vol. 23, no. 8, pp. 1504–1510, 2012.

[9] A. S. Aricò, P. Bruce, B. Scrosati, J.-M. Tarascon, and W. van Schalkwijk, "Nanostructured materials for advanced energy conversion and storage devices," *Nature Materials*, vol. 4, no. 5, pp. 366–377, 2005.

[10] J. Xu and C. P. Wong, "Characterization and properties of an organic–inorganic dielectric nanocomposite for embedded decoupling capacitor applications," *Composites Part A: Applied Science and Manufacturing*, vol. 38, no. 1, pp. 13–19, 2007.

[11] Y. Rao and C. P. Wong, "Material characterization of a high-dielectric-constant polymer–ceramic composite for embedded capacitor for RF applications," *Journal of Applied Polymer Science*, vol. 92, no. 4, pp. 2228–2231, 2004.

[12] M. Rahimabady, M. S. Mirshekarloo, K. Yao, and L. Lu, "Dielectric behaviors and high energy storage density of nanocomposites with core–shell $BaTiO_3$@TiO_2 in poly(vinylidene fluoride-hexafluoropropylene)," *Physical Chemistry Chemical Physics*, vol. 15, no. 38, pp. 16242–16248, 2013.

[13] J. Xu and C. P. Wong, "Low-loss percolative dielectric composite," *Applied Physics Letters*, vol. 87, no. 8, article 082907, 2005.

[14] Z. M. Dang, Y. J. Xia, J. W. Zha, J. K. Yuan, and J. Bai, "Preparation and dielectric properties of surface modified TiO_2/silicone rubber nanocomposites," *Materials Letters*, vol. 65, no. 23-24, pp. 3430–3432, 2011.

[15] H. Zheng, J. Wang, S. E. Lofland et al., "Multiferroic $BaTiO_3$-$CoFe_2O_4$ nanostructures," *Science*, vol. 303, no. 5658, pp. 661–663, 2004.

[16] Y. Gao, M. Yuan, X. Sun, and J. Ouyang, "In situ preparation of high quality $BaTiO_3$ dielectric films on Si at 350–500°C," *Journal of Materials Science: Materials in Electronics*, vol. 28, no. 1, pp. 337–343, 2017.

[17] G. Arlt, D. Hennings, and G. de With, "Dielectric properties of fine-grained barium titanate ceramics," *Journal of Applied Physics*, vol. 58, no. 4, pp. 1619–1625, 1985.

[18] K. L. Choi, N. Na, and M. Swaminathan, "Characterization of embedded passives using macromodels in LTCC technology," *IEEE Transactions on Components, Packaging, and Manufacturing Technology: Part B*, vol. 21, no. 3, pp. 258–268, 1998.

[19] M. A. Ramírez, P. R. Bueno, R. Tararam, A. A. Cavalheiro, E. Longo, and J. A. Varela, "Evaluation of the effect of the stoichiometric ratio of Ca/Cu on the electrical and microstructural properties of the $CaCu_3Ti_4O_{12}$ polycrystalline system," *Journal of Physics D: Applied Physics*, vol. 42, no. 18, pp. 185503–185510, 2009.

[20] A. Eigner and S. Semino, "50 years of electrical-stress control in cable accessories," *IEEE Electrical Insulation Magazine*, vol. 29, no. 5, pp. 47–55, 2013.

[21] H. Wang, W. Zhong, P. Xu, and Q. Du, "Properties of polyimide/silica nanohybrids from silicic acid oligomer," *Macromolecular Materials and Engineering*, vol. 289, no. 9, pp. 793–799, 2004.

[22] J. Jumpatam, P. Thongbai, B. Kongsook, T. Yamwong, and S. Maensiri, "High permittivity, low dielectric loss, and high

electrostatic potential barrier in $Ca_2Cu_2Ti_4O_{12}$ ceramics," *Materials Letters*, vol. 76, no. 1, pp. 40–42, 2012.

[23] B. Chu, X. Zhou, K. Ren et al., "A dielectric polymer with high electric energy density and fast discharge speed," *Science*, vol. 313, no. 5785, pp. 334–336, 2006.

[24] K. Yu, Y. Niu, Y. Zhou, Y. Bai, and H. Wang, "Nanocomposites of surface-modified $BaTiO_3$ nanoparticles filled ferroelectric polymer with enhanced energy density," *Journal of the American Ceramic Society*, vol. 96, no. 8, pp. 2519–2524, 2013.

[25] Q. Li, G. Zhang, X. Zhang, S. Jiang, Y. Zeng, and Q. Wang, "Relaxor ferroelectric-based electrocaloric polymer nanocomposites with a broad operating temperature range and high cooling energy," *Advanced Materials*, vol. 27, no. 13, pp. 2236–2241, 2015.

[26] L. Zhu and Q. Wang, "Novel ferroelectric polymers for high energy density and low loss dielectrics," *Macromolecules*, vol. 45, no. 7, pp. 2937–2954, 2012.

[27] X. H. Tang, Y. You, H. Mao, K. Li, R. B. Wei, and X. B. Liu, "Energy storage of polyarylene ether nitriles at high temperature," *Electronic Materials Letters*, vol. 14, no. 4, pp. 440–445, 2018.

[28] J. N. Coleman, U. Khan, W. J. Blau, and Y. K. Gun'ko, "Small but strong: a review of the mechanical properties of carbon nanotube-polymer composites," *Carbon*, vol. 44, no. 9, pp. 1624–1652, 2006.

[29] S. K. Hwang, I. Bae, S. M. Cho, R. H. Kim, H. J. Jung, and C. Park, "High performance multi-level non-volatile polymer memory with solution-blended ferroelectric polymer/high-k insulators for low voltage operation," *Advanced Functional Materials*, vol. 23, no. 44, pp. 5484–5493, 2013.

[30] M. Kaseem, K. Hamad, and Y. G. Ko, "Fabrication and materials properties of polystyrene/carbon nanotube (PS/CNT) composites: a review," *European Polymer Journal*, vol. 79, pp. 36–62, 2016.

[31] R. Ma, A. F. Baldwin, C. Wang et al., "Rationally designed polyimides for high-energy density capacitor applications," *ACS Applied Materials & Interfaces*, vol. 6, no. 13, pp. 10445–10451, 2014.

[32] L. Zhang, S. Chen, S. Yuan, D. Wang, P. H. Hu, and Z. M. Dang, "Low dielectric loss and weak frequency dependence of dielectric permittivity of the CeO_2/polystyrene nanocomposite films," *Applied Physics Letters*, vol. 105, no. 5, article 052905, 2014.

[33] B. Luo, X. Wang, Y. Wang, and L. Li, "Fabrication, characterization, properties and theoretical analysis of ceramic/PVDF composite flexible films with high dielectric constant and low dielectric loss," *Journal of Materials Chemistry A*, vol. 2, no. 2, pp. 510–519, 2014.

[34] H. Li, Z. Li, F. Lin, Y. Chen, D. Liu, and B. Wang, "Insulation resistance of metallized polypropylene film capacitors under different electric fields," *IEEE Transactions on Dielectrics and Electrical Insulation*, vol. 20, no. 4, pp. 1315–1320, 2013.

[35] R. Yang, R. Wei, K. Li, L. Tong, K. Jia, and X. Liu, "Cross-linked polyarylene ether nitrile film as flexible dielectric materials with ultrahigh thermal stability," *Scientific Reports*, vol. 6, no. 1, article 36434, 2016.

[36] F. Meng, R. Zhao, Y. Zhan, and X. Liu, "Design of thorn-like micro/nanofibers: fabrication and controlled morphology for engineered composite materials applications," *Journal of Materials Chemistry*, vol. 21, no. 41, pp. 16385–16390, 2011.

[37] J. Yang, H. Tang, Y. Zhan, H. Guo, R. Zhao, and X. Liu, "Photoelectric properties of poly(arylene ether nitriles)–copper phthalocyanine conjugates complex via in situ polymerization," *Materials Letters*, vol. 72, pp. 42–45, 2012.

[38] X. Huang, M. Feng, and X. Liu, "Design of bristle-like TiO_2-MWCNT nanotubes to improve the dielectric and interfacial properties of polymer-based composite films," *RSC Advances*, vol. 4, no. 10, pp. 4985–4992, 2014.

[39] H. Mao, Y. You, L. F. Tong, X. H. Tang, R. B. Wei, and X. B. Liu, "Dielectric properties of diblock copolymers containing a polyarylene ether nitrile block and a polyarylene ether ketone block," *Journal of Materials Science: Materials in Electronics*, vol. 29, no. 4, pp. 3127–3134, 2017.

[40] L. Tong, R. Wei, J. Wang, and X. Liu, "Phthalonitrile end-capped polyarylene ether nitrile nanocomposites with Cu^{2+} bridged carbon nanotube and graphene oxide network," *Materials Letters*, vol. 178, pp. 312–315, 2016.

[41] K. Abe, D. Nagao, and M. Konno, "Fabrication of highly refractive BaTiO3 nanocomposite films using heat resistant polymer as matrix," *European Polymer Journal*, vol. 49, no. 11, pp. 3455–3459, 2013.

[42] M. Xu, T. Zhang, B. Gu, J. Wu, and Q. Chen, "Synthesis and properties of novel polyurethane–urea/multiwalled carbon nanotube composites," *Macromolecules*, vol. 39, no. 10, pp. 3540–3545, 2006.

[43] L. Xie, X. Huang, Y. Huang, K. Yang, and P. Jiang, "Core-shell structured hyperbranched aromatic polyamide/$BaTiO_3$ hybrid filler for poly(vinylidene fluoride-trifluoroethylene-chlorofluoroethylene) nanocomposites with the dielectric constant comparable to that of percolative composites," *ACS Applied Materials & Interfaces*, vol. 5, no. 5, pp. 1747–1756, 2013.

[44] S. A. Paniagua, Y. Kim, K. Henry, R. Kumar, J. W. Perry, and S. R. Marder, "Surface-initiated polymerization from barium titanate nanoparticles for hybrid dielectric capacitors," *ACS Applied Materials & Interfaces*, vol. 6, no. 5, pp. 3477–3482, 2014.

[45] L. Xie, X. Huang, C. Wu, and P. Jiang, "Core-shell structured poly(methyl methacrylate)/$BaTiO_3$ nanocomposites prepared by in situ atom transfer radical polymerization: a route to high dielectric constant materials with the inherent low loss of the base polymer," *Journal of Materials Chemistry*, vol. 21, no. 16, pp. 5897–5906, 2011.

[46] B. Balasubramanian, K. L. Kraemer, N. A. Reding, R. Skomski, S. Ducharme, and D. J. Sellmyer, "Synthesis of monodisperse TiO_2–paraffin core–shell nanoparticles for improved dielectric properties," *ACS Nano*, vol. 4, no. 4, pp. 1893–1900, 2010.

[47] Z. Li, L. A. Fredin, P. Tewari et al., "In situ catalytic encapsulation of core-shell nanoparticles having variable shell thickness: dielectric and energy storage properties of high-permittivity metal oxide nanocomposites," *Chemistry of Materials*, vol. 22, no. 18, pp. 5154–5164, 2010.

[48] X. Pang, Y. He, B. Jiang et al., "Block copolymer/ferroelectric nanoparticle nanocomposites," *Nanoscale*, vol. 5, no. 18, pp. 8695–8702, 2013.

[49] Y. U. Wang and D. Q. Tan, "Computational study of filler microstructure and effective property relations in dielectric composites," *Journal of Applied Physics*, vol. 109, no. 10, pp. 104102–104109, 2011.

[50] S. Ducharme, "An inside-out approach to storing electrostatic energy," *ACS Nano*, vol. 3, no. 9, pp. 2447–2450, 2009.

[51] A. Maliakal, H. Katz, P. M. Cotts, S. Subramoney, and P. Mirau, "Inorganic oxide core, polymer shell nanocomposite as a high *K* gate dielectric for flexible electronics applications," *Journal of the American Chemical Society*, vol. 127, no. 42, pp. 14655–14662, 2005.

[52] A. Kahouli, O. Gallot-Lavallée, P. Rain et al., "Structure effect of thin film polypropylene view by dielectric spectroscopy and X-ray diffraction: application to dry type power capacitors," *Journal of Applied Polymer Science*, vol. 132, no. 39, 2015.

[53] M. Sharma, M. P. Singh, C. Srivastava, G. Madras, and S. Bose, "Poly(vinylidene fluoride)-based flexible and lightweight materials for attenuating microwave radiations," *ACS Applied Materials & Interfaces*, vol. 6, no. 23, pp. 21151–21160, 2014.

[54] Y. You, X. Huang, Z. Pu, K. Jia, and X. Liu, "Enhanced crystallinity, mechanical and dielectric properties of biphenyl polyarylene ether nitriles by unidirectional hot-stretching," *Journal of Polymer Research*, vol. 22, no. 11, 2015.

[55] X. Liu, S. Long, D. Luo, W. Chen, and G. Cao, "Preparation and properties of polyarylene ether nitrites/multi-walled carbon nanotubes composites," *Materials Letters*, vol. 62, no. 1, pp. 19–22, 2008.

[56] Y. You, X. Du, H. Mao, X. Tang, R. Wei, and X. Liu, "Synergistic enhancement of mechanical, crystalline and dielectric properties of polyarylene ether nitrile-based nanocomposites by unidirectional hot stretching–quenching," *Polymer International*, vol. 66, no. 8, pp. 1151–1158, 2017.

[57] L. Tong, K. Jia, and X. Liu, "Novel phthalonitrile-terminated polyarylene ether nitrile with high glass transition temperature and enhanced thermal stability," *Materials Letters*, vol. 128, pp. 267–270, 2014.

[58] H. Tang, J. Yang, J. Zhong, R. Zhao, and X. Liu, "Synthesis of high glass transition temperature fluorescent polyarylene ether nitrile copolymers," *Materials Letters*, vol. 65, no. 11, pp. 1703–1706, 2011.

[59] Y. Zhan, F. Meng, X. Yang, Y. Lei, R. Zhao, and X. Liu, "Synthesis, characterization and properties of multifunctional poly(arylene ether nitriles) (PEN)/CNTs/Fe_3O_4 nanocomposites," *Journal of Polymer Science Part B: Polymer Physics*, vol. 49, no. 8, pp. 611–619, 2011.

[60] X. B. Liu, R. H. Du, L. L. Hao, S. Wang, G. P. Cao, and H. Jiang, "Synthesis, characterization and rheological property of biphenyl-based polyarylene ether nitrile copolymers," *Express Polymer Letters*, vol. 1, no. 8, pp. 499–505, 2007.

[61] Z. Pu, H. Tang, X. Huang et al., "Effect of surface functionalization of SiO_2 particles on the interfacial and mechanical properties of PEN composite films," *Colloids and Surfaces A: Physicochemical and Engineering Aspects*, vol. 415, pp. 125–133, 2012.

[62] L. Xie, X. Huang, K. Yang, S. Li, and P. Jiang, ""Grafting to" route to PVDF-HFP-GMA/$BaTiO_3$ nanocomposites with high dielectric constant and high thermal conductivity for energy storage and thermal management applications," *Journal of Materials Chemistry A*, vol. 2, no. 15, pp. 5244–5251, 2014.

[63] J. W. Wang, Q. D. Shen, C. Z. Yang, and Q. M. Zhang, "High dielectric constant composite of P(VDF–TrFE) with grafted copper phthalocyanine oligomer," *Macromolecules*, vol. 37, no. 6, pp. 2294–2298, 2004.

[64] Q. M. Zhang, H. Li, M. Poh et al., "An all-organic composite actuator material with a high dielectric constant," *Nature*, vol. 419, no. 6904, pp. 284–287, 2002.

[65] Z. Pu, R. Wei, and X. Liu, "Influence of unidirectional hot-stretching on the mechanical and dielectric properties of polymer-based composites," in *Energy Science and Applied Technology ESAT 2016: Proceedings of the International Conference on Energy Science and Applied Technology (ESAT 2016)*, pp. 191–194, Wuhan, China, 2016.

[66] K. Jia, L. Pan, Z. Wang et al., "Morphology and photophysical properties of dual-emissive hyperbranched zinc phthalocyanines and their self-assembling superstructures," *Journal of Materials Science*, vol. 51, no. 6, pp. 3191–3199, 2016.

[67] R. Yang, K. Li, L. Tong, K. Jia, and X. Liu, "The relationship between processing and performances of polyarylene ether nitriles terminated with phthalonitrile/trifunctional phthalonitrile composites," *Journal of Polymer Research*, vol. 22, no. 11, p. 210, 2015.

[68] Y. Huang, Y. Luo, M. Xu, Y. Lei, and X. Liu, "Studied on mechanical, thermal and dielectric properties of BPh/PEN-OH copolymer," *Composites Part B: Engineering*, vol. 106, no. 1, pp. 294–299, 2016.

[69] C. Long, R. Wei, X. Huang, M. Feng, K. Jia, and X. Liu, "Mechanical, dielectric, and rheological properties of poly(arylene ether nitrile)–reinforced poly(vinylidene fluoride)," *High Performance Polymers*, vol. 29, no. 2, pp. 178–186, 2017.

[70] R. Wei, K. Li, J. Ma, H. Zhang, and X. Liu, "Improving dielectric properties of polyarylene ether nitrile with conducting polyaniline," *Journal of Materials Science: Materials in Electronics*, vol. 27, no. 9, pp. 9565–9571, 2016.

[71] V. S. Nisa, S. Rajesh, K. P. Murali, V. Priyadarsini, S. N. Potty, and R. Ratheesh, "Preparation, characterization and dielectric properties of temperature stable $SrTiO_3$/PEEK composites for microwave substrate applications," *Composites Science and Technology*, vol. 68, no. 1, pp. 106–112, 2008.

[72] Y. Hu, Y. Zhang, H. Liu, and D. Zhou, "Microwave dielectric properties of PTFE/$CaTiO_3$ polymer ceramic composites," *Ceramics International*, vol. 37, no. 5, pp. 1609–1613, 2011.

[73] D. Padalia, G. Bisht, U. C. Johri, and K. Asokan, "Fabrication and characterization of cerium doped barium titanate/PMMA nano-composites," *Solid State Sciences*, vol. 19, no. 5, pp. 122–129, 2013.

[74] T. Hoshina, "Size effect of barium titanate fine particles and ceramics," *Journal of the Ceramic Society of Japan*, vol. 121, no. 1410, pp. 156–161, 2013.

[75] H. Tang, J. Zhong, J. Yang, Z. Ma, and X. Liu, "Flexible polyarylene ether nitrile/$BaTiO_3$ nanocomposites with high energy density for film capacitor applications," *Journal of Electronic Materials*, vol. 40, no. 2, pp. 141–148, 2011.

[76] B. Schumacher, H. Geßwein, J. Haußelt, and T. Hanemann, "Temperature treatment of nano-scaled barium titanate filler to improve the dielectric properties of high-k polymer based composites," *Microelectronic Engineering*, vol. 87, no. 10, pp. 1978–1983, 2010.

[77] Y. Sun, Z. Zhang, and C. P. Wong, "Influence of interphase and moisture on the dielectric spectroscopy of epoxy/silica composites," *Polymer*, vol. 46, no. 7, pp. 2297–2305, 2005.

[78] Y. Kobayashi, T. Tanase, T. Tabata, T. Miwa, and M. Konno, "Fabrication and dielectric properties of the $BaTiO_3$–polymer nano-composite thin films," *Journal of the European Ceramic Society*, vol. 28, no. 1, pp. 117–122, 2008.

[79] P. Kim, S. C. Jones, P. J. Hotchkiss et al., "Phosphonic acid-modified barium titanate polymer nanocomposites with high

permittivity and dielectric strength," *Advanced Materials*, vol. 19, no. 7, pp. 1001–1005, 2007.

[80] Y. Rao, A. Takahashi, and C. P. Wong, "Di-block copolymer surfactant study to optimize filler dispersion in high dielectric constant polymer-ceramic composite," *Composites Part A: Applied Science and Manufacturing*, vol. 34, no. 11, pp. 1113–1116, 2003.

[81] S. J. Chang, W. S. Liao, C. J. Ciou, J. T. Lee, and C. C. Li, "An efficient approach to derive hydroxyl groups on the surface of barium titanate nanoparticles to improve its chemical modification ability," *Journal of Colloid and Interface Science*, vol. 329, no. 2, pp. 300–305, 2009.

[82] H. Tang, P. Wang, P. Zheng, and X. Liu, "Core-shell structured $BaTiO_3$@polymer hybrid nanofiller for poly(arylene ether nitrile) nanocomposites with enhanced dielectric properties and high thermal stability," *Composites Science and Technology*, vol. 123, pp. 134–142, 2016.

[83] X. Huang, Z. Pu, L. Tong, Z. Wang, and X. Liu, "Preparation and dielectric properties of surface modified TiO_2/PEN composite films with high thermal stability and flexibility," *Journal of Materials Science: Materials in Electronics*, vol. 23, no. 12, pp. 2089–2097, 2012.

[84] H. Tang, Z. Ma, J. Zhong, J. Yang, R. Zhao, and X. Liu, "Effect of surface modification on the dielectric properties of PEN nanocomposites based on double-layer core/shell-structured $BaTiO_3$ nanoparticles," *Colloids and Surfaces A: Physicochemical and Engineering Aspects*, vol. 384, no. 1–3, pp. 311–317, 2011.

[85] Y. You, W. Han, L. Tu, Y. Wang, R. Wei, and X. Liu, "Double-layer core/shell-structured nanoparticles in polyarylene ether nitrile-based nanocomposites as flexible dielectric materials," *RSC Advances*, vol. 7, no. 47, pp. 29306–29311, 2017.

[86] F. He, S. Lau, H. L. Chan, and J. Fan, "High dielectric permittivity and low percolation threshold in nanocomposites based on poly (vinylidene fluoride) and exfoliated graphite nanoplates," *Advanced Materials*, vol. 21, no. 6, pp. 710–715, 2009.

[87] K. Li, L. Tong, R. Yang, R. Wei, and X. Liu, "In-situ preparation and dielectric properties of silver-polyarylene ether nitrile nanocomposite films," *Journal of Materials Science: Materials in Electronics*, vol. 27, no. 5, pp. 4559–4565, 2016.

[88] Y. You, R. Wei, R. Yang, W. Yang, X. Hua, and X. Liu, "Crystallization behaviors of polyarylene ether nitrile filled in multi-walled carbon nanotubes," *RSC Advances*, vol. 6, no. 75, pp. 70877–70883, 2016.

[89] A. R. Kamali, H. K. Kim, K. B. Kim, R. Vasant Kumar, and D. J. Fray, "Large scale green production of ultra-high capacity anode consisting of graphene encapsulated silicon nanoparticles," *Journal of Materials Chemistry A*, vol. 5, no. 36, pp. 19126–19135, 2017.

[90] Y. Shen, Y. Lin, M. Li, and C.-W. Nan, "High dielectric performance of polymer composite films induced by a percolating interparticle barrier layer," *Advanced Materials*, vol. 19, no. 10, pp. 1418–1422, 2007.

[91] T. S. Kelby, M. Wang, and W. T. S. Huck, "Controlled folding of 2D Au–polymer brush composites into 3D microstructures," *Advanced Functional Materials*, vol. 21, no. 4, pp. 652–657, 2011.

[92] Z. Pu, L. Tong, M. Feng, K. Jia, and X. Liu, "Influence of hyperbranched copper phthalocyanine grafted carbon nanotubes on the dielectric and rheological properties of polyarylene ether nitriles," *RSC Advances*, vol. 5, no. 88, pp. 72028–72036, 2015.

[93] M. Ruan, J. Guan, D. He, T. Meng, and Q. Zhang, "The hydrogenation of aromatic-naphthalene with Ni_2P/CNTs," *RSC Advances*, vol. 5, no. 71, pp. 57700–57703, 2015.

[94] P. Zheng, Z. Pu, W. Yang, S. Shen, K. Jia, and X. Liu, "Effect of multiwalled carbon nanotubes on the crystallization and dielectric properties of BP-PEN nanocomposites," *Journal of Materials Science: Materials in Electronics*, vol. 25, no. 9, pp. 3833–3839, 2014.

[95] H. H. So, J. W. Cho, and N. G. Sahoo, "Effect of carbon nanotubes on mechanical and electrical properties of polyimide/carbon nanotubes nanocomposites," *European Polymer Journal*, vol. 43, no. 9, pp. 3750–3756, 2007.

[96] F. Jin, M. Feng, K. Jia, and X. Liu, "Aminophenoxyphthalonitrile modified MWCNTs/polyarylene ether nitriles composite films with excellent mechanical, thermal, dielectric properties," *Journal of Materials Science: Materials in Electronics*, vol. 26, no. 7, pp. 5152–5160, 2015.

[97] Z. Pu, X. Huang, L. Chen, J. Yang, H. Tang, and X. Liu, "Effect of nitrile-functionalization and thermal cross-linking on the dielectric and mechanical properties of PEN/CNTs–CN composites," *Journal of Materials Science: Materials in Electronics*, vol. 24, no. 8, pp. 2913–2922, 2013.

[98] X. Huang, M. Feng, and X. Liu, "Synergistic enhancement of dielectric constant of novel core/shell $BaTiO_3$@MWCNTs/PEN nanocomposites with high thermal stability," *Journal of Materials Science: Materials in Electronics*, vol. 25, no. 1, pp. 97–102, 2014.

[99] X. Huang, K. Wang, K. Jia, and X. Liu, "Preparation of TiO_2–MWCNT core/shell heterostructures containing a single MWCNT and their electromagnetic properties," *Composite Interfaces*, vol. 22, no. 5, pp. 343–351, 2015.

[100] Q. Xiao, R. Yang, Y. You, H. Zhang, R. Wei, and X. Liu, "Crystalline, mechanical and dielectric properties of polyarylene ether nitrile with multi-walled carbon nanotube filled with polyarylene ether nitrile," *Journal of Nanoscience and Nanotechnology*, vol. 18, no. 6, pp. 4311–4317, 2018.

[101] A. G. Garcia, S. E. Baltazar, A. H. R. Castro, J. F. P. Robles, and A. Rubio, "Influence of S and P doping in a graphene sheet," *Journal of Computational and Theoretical Nanoscience*, vol. 5, no. 11, pp. 2221–2229, 2008.

[102] Z. Wang, W. Yang, and X. Liu, "Electrical properties of poly(arylene ether nitrile)/graphene nanocomposites prepared by in situ thermal reduction route," *Journal of Polymer Research*, vol. 21, no. 2, p. 358, 2014.

[103] M. Fang, K. Wang, H. Lu, Y. Yang, and S. Nutt, "Single-layer graphene nanosheets with controlled grafting of polymer chains," *Journal of Materials Chemistry*, vol. 20, no. 10, pp. 1982–1992, 2010.

[104] J. Yang, M. Wu, F. Chen, Z. Fei, and M. Zhong, "Preparation, characterization, and supercritical carbon dioxide foaming of polystyrene/graphene oxide composites," *Journal of Supercritical Fluids*, vol. 56, no. 2, pp. 201–207, 2011.

[105] A. L. Higginbotham, J. R. Lomeda, A. B. Morgan, and J. M. Tour, "Graphite oxide flame-retardant polymer nanocomposites," *ACS Applied Materials & Interfaces*, vol. 1, no. 10, pp. 2256–2261, 2009.

[106] W. S. Hummers Jr. and R. E. Offeman, "Preparation of graphitic oxide," *Journal of the American Chemical Society*, vol. 80, no. 6, pp. 1339–1339, 1958.

[107] Z. Ma, D. Liu, Y. Zhu et al., "Graphene oxide/chitin nanofibril composite foams as column adsorbents for aqueous pollutants," *Carbohydrate Polymers*, vol. 144, no. 25, pp. 230–237, 2016.

[108] J. Li, Z. Pu, Z. Wang, Y. Long, K. Jia, and X. Liu, "High dielectric constants of composites of fiber-like copper phthalocyanine-coated graphene oxide embedded in poly(-arylene ether nitriles)," *Journal of Electronic Materials*, vol. 44, no. 7, pp. 2378–2386, 2015.

[109] Y. Zhan, X. Yang, H. Guo, J. Yang, F. Meng, and X. Liu, "Cross-linkable nitrile functionalized graphene oxide/poly(-arylene ether nitrile) nanocomposite films with high mechanical strength and thermal stability," *Journal of Materials Chemistry*, vol. 22, no. 12, pp. 5602–5608, 2012.

[110] J. Wang, R. Wei, L. Tong, and X. Liu, "Effect of magnetite bridged carbon nanotube/graphene networks on the properties of polyarylene ether nitrile," *Journal of Materials Science: Materials in Electronics*, vol. 28, no. 5, pp. 3978–3986, 2017.

[111] R. Wei, J. Wang, H. Zhang, W. Han, and X. Liu, "Crosslinked polyarylene ether nitrile interpenetrating with zinc ion bridged graphene sheet and carbon nanotube network," *Polymer*, vol. 9, no. 12, p. 342, 2017.

Hindawi
International Journal of Polymer Science
Volume 2018, Article ID 3270313, 11 pages
https://doi.org/10.1155/2018/3270313

Research Article

Theoretical Study on the Photoelectric Properties of a Class of Copolymers Based on Benzodithiophene for Solar Cells

Xiao-Hua Xie,[1] **Xin-Wei Zhao**,[2] **and Ming Li**[3]

[1]*School of Chemistry and Chemical Engineering, Yangtze Normal University, Chongqing 408100, China*
[2]*Department of Physics, Tokyo University of Science, 1-3 Kagurazaka, Shinjuku-ku, Tokyo 162-8601, Japan*
[3]*School of Chemistry and Chemical Engineering, Southwest University, Chongqing 400715, China*

Correspondence should be addressed to Ming Li; liming@swu.edu.cn

Received 20 January 2018; Accepted 29 March 2018; Published 30 May 2018

Academic Editor: Xiufu Hua

The structural, electronic, and optical properties of PBDTTBT are comprehensively studied by density functional theory to rationalize the experimentally observed properties. Periodic boundary conditions method is employed to simulate the polymer block and calculate effective charge mass from the band structure calculation to describe charge transport properties. Moreover, both time-dependent density functional theory and a set of multidimensional visualization techniques are used to characterize the exciton dissociation ability in the PCBM: PBDTTBT interface. These theoretical methods and calculation techniques not only promote deep understanding of the connection between chemical structures and optical and electronic properties of the donor-acceptor system but also can be used to rationally design a novel donor-acceptor system. Based on the same calculated methods as PBDTTBT, four copolymers PBDTTTP, PBDTTTO, PBDTTTPD, and PBDTTFPD are designed to study their potentials as donors in polymer BHJ. The results indicate that PBDTTBT's well conjugation benefits its good stability, and its wide and strong absorption spectra in the range of visible light, appropriate FMO levels, well charge transport, and favorable exciton dissociation lead to its photovoltaic performance. Furthermore, through comparing the four designed polymers with PBDTTBT, we conclude that the four designed polymers have stronger exciton dissociation ability and larger open-circuit voltage and external quantum efficiencies. Consequently, the four designed copolymers are promising candidates for polymer BHJ solar cells.

1. Introduction

Solar cells are one critical technology for solving world energy needs. Traditional solar cells made from high-purity silicon have been commercialized, but their applications are finite because of high cost and weight. Polymer photovoltaic cells with a bulk heterojunction (BHJ) active layer have attracted attention due to their potentially low cost, lightweight, flexible, and easy manufacturing [1–4]. In the BHJ structure, the active layer that is sandwiched between anode and cathode constitutes of electron-donating conjugated polymer and electron acceptor, and its properties are the most determining factors in the whole performance of polymer BHJ [5].

In the past few decades, many progresses have been made in polymer BHJ which have reached power conversion efficiencies (PCE) of 11% [6]. The limiting factors of PCE are the stabilities, ability of harvesting the photon flux from the sun, effective exciton separation, and carrier mobilities. In order to improve the device performances, one can develop new device architectures [7, 8], synthesize new polymer donors [9, 10] and new electron acceptors [11–14], or work on both ends.

In recent years, developing low bandgap polymers has provided an alternative approach for achieving high PCEs resulting from their important roles in photoelectric conversion process: capturing solar photons from the sun, exciton generation and separation, carrier injection, hole transport, and affecting the size of the open-circuit voltage (V_{oc}) and short-circuit current (J_{SC}), thus affecting PCE ($\eta = V_{OC} \times J_{SC} \times FF/P_{in}$). In order to develop low-bandgap conjugated polymers, the most powerful strategy is to incorporate

electron-rich donor segments and electron-deficient acceptor segments into the polymer backbone. Due to the push-pull interaction, efficient internal charge transfer (ICT) can take place from the donor (D) to the acceptor (A) upon photoexcitation, thus leading to a new absorption band at longer wavelengths [15] and producing appropriate molecular energy levels for high V_{oc}, good charge transport, and high J_{SC}, thus improving PCE [16].

In recent years, some benzo[1,2-b:4,5-b′]dithiophene-containing polymers have been applied to polymer BHJ and field-effect transistor (FET) [17–22] on account of its electron-rich structures. The relatively large and planar molecular structures of thiophene (TH) derivatives not only keep a high mobility but also help to promote cofacial π-π stacking. Given the symmetrical planar structure and high mobility of benzo[1,2-*b*:4,5-*b*′]dithiophene (BDT), Huo and his coworkers synthesized a polymer based on BDT, that is, PBDTTBT [23]. PBDTTBT was well soluble in common organic solvents due to its strong octyl chains and presented an excellent thermal stability with a decomposition temperature of 337°C without the protection of an inert atmosphere. The group fabricated a polymer solar cell device based on PBDTTBT donor and $PC_{70}BM$ (a fullerene derivative) acceptor in 2010. The structure of the device is ITO/PEDOT-PSS/polymer: $PC_{70}BM$ (1 : 2, *w*/*w*)/Ca/Al, and its V_{oc}, J_{SC}, fill factor (FF), and PCE are 0.92 V, 10.70 mA·cm^{-2}, 57.5%, and 5.66%, respectively [23].

In order to rationalize the experimentally observed properties of known materials and predict those of unknown ones, theoretical investigations on the structure features, charge transport properties, and exciton dissociation abilities of PBDTTBT are indispensable. In the modeling process, we replace the octyls with butyls to reduce the computation cost. Analogously, we replace benzo[c][1,2,5]thiadiazole with four pyridazine derivatives and designed four polybenzo[1,2-*b*:4,5-*b*′]dithiophene derivatives, PBDTTTP, PBDTTTO, PBDTTTPD, and PBDTTFPD and study their potentials as donors in polymer BHJ based on $PC_{70}BM$. Several parameters of determining the performance of solar cells, electronic and structural properties, open-circuit voltage (V_{OC}), charge transfer properties, exciton dissociation abilities, and theoretical PCE have been investigated.

This paper's distribution is as follows. In Section 2, we describe the computational methods to obtain electronic and structural properties. In Section 3, we detailedly describe the influences on the performance of solar cells by comparing PBDTTBT with designed copolymers, and the conclusion is in Section 4.

2. Calculation Methods

Density functional theory (DFT) has been broadly used to investigate the properties of organic compounds because its high accuracy is reasonable with the ab initio method and less computational time cost, and B3LYP, a hybrid functional, is widely used in calculating organic systems [24–27]. In this paper, DFT and time-dependent DFT (TD-DFT) [28] are employed to gain the qualitative properties of all the compounds at b3lyp/6-31g* level [29, 30]. All the optimized structures are the global minima on the potential energy surface. Periodic boundary conditions (PBC) [31] method is used to optimize block polymers at B3LYP/6-31G(d) and B3PW91/6-31G(d) levels [32]. All the calculations are implemented by Gaussian 09 package [33]. As to the copolymers, density topological analyses are examined by atom in molecule (AIM) analyses [34]. Moreover, the nucleus-independent chemical shift (NICS) [35, 36] is also calculated for copolymers at the B3LYP/6-31G* level, and NICS defined as the negative of the magnetic shielding at a ring critical point (RCP) is obtained from the AIM analyses. Furthermore, the bonding characteristics were also investigated by natural bond orbital (NBO) theory [37–40] and AOMix program packages [41].

3. Results and Discussion

3.1. Geometry Optimization. The drafts of the studied copolymers are depicted in Figure 1, and the optimized structures of parent molecules of copolymers by B3LYP/6-31G(d) along with the abbreviations of each segments are shown in Figure 2. The selected bond lengths and bond angles of these copolymers are also given in Figure 1; herein, the C1-C2 (in PBDTTBT) or C2-C3 (in other copolymers) bond is defined as the central bond that connects the donor and acceptor. All the studied copolymers have the same central bonds (1.45 Å), and their dihedral angles are smaller than 37°, which suggest that all the polymers are rigid backbones. The nitrogen- (N-) hydrogen (H) or sulfur (S)/oxygen- (O-) nitrogen (N) interactions forming stable six or five-member rings reduce the dihedral angles and keep the molecular coplanarity, thus benefitting to the rigidity of the copolymers. Besides, the densities of bond critical points (BCPs) and RCPs as well as the distances between the two interactional atoms are also presented in Figure 1. It is worth noting that the angles of S1-C4-C5-C6 and C7-C8-C9-S2 in the four designed copolymers are smaller than C4-C5-C6-C7 and C8-C9-C10-C11 angles in PBDTTBT, which leads to better coplanarity than PBDTTBT.

In order to acquire the charge population analysis on central bonds in studied polymers, we calculate the characters of bond critical points (BCPs) in central bonds and list the data in Table 1S in Supplementary Materials. The data indicate that the two atoms in central bonds are relatively accumulated due to sharing interactions.

Furthermore, the HOMO and LUMO diagrams of monomers in Figure 1S not only can qualitatively illustrate the electronic cloud distribution but also reflect the electron-donating and electron-accepting segments. We can clearly see from Figure 1S that the electronic cloud distribution of HOMO of all the monomers localizes near the polymeric axis and mainly localizes on BDT segments in the four designed copolymers, while that of LUMO localizes near the TBT, TTP, TTO, TTPD, and TFPD segments (the segments in rectangle in Figure 2). The molecular orbital diagrams illustrate that the BDT segments contributing to HOMOs in the five copolymers are as electron-donating segments, and the left segments (TBT,

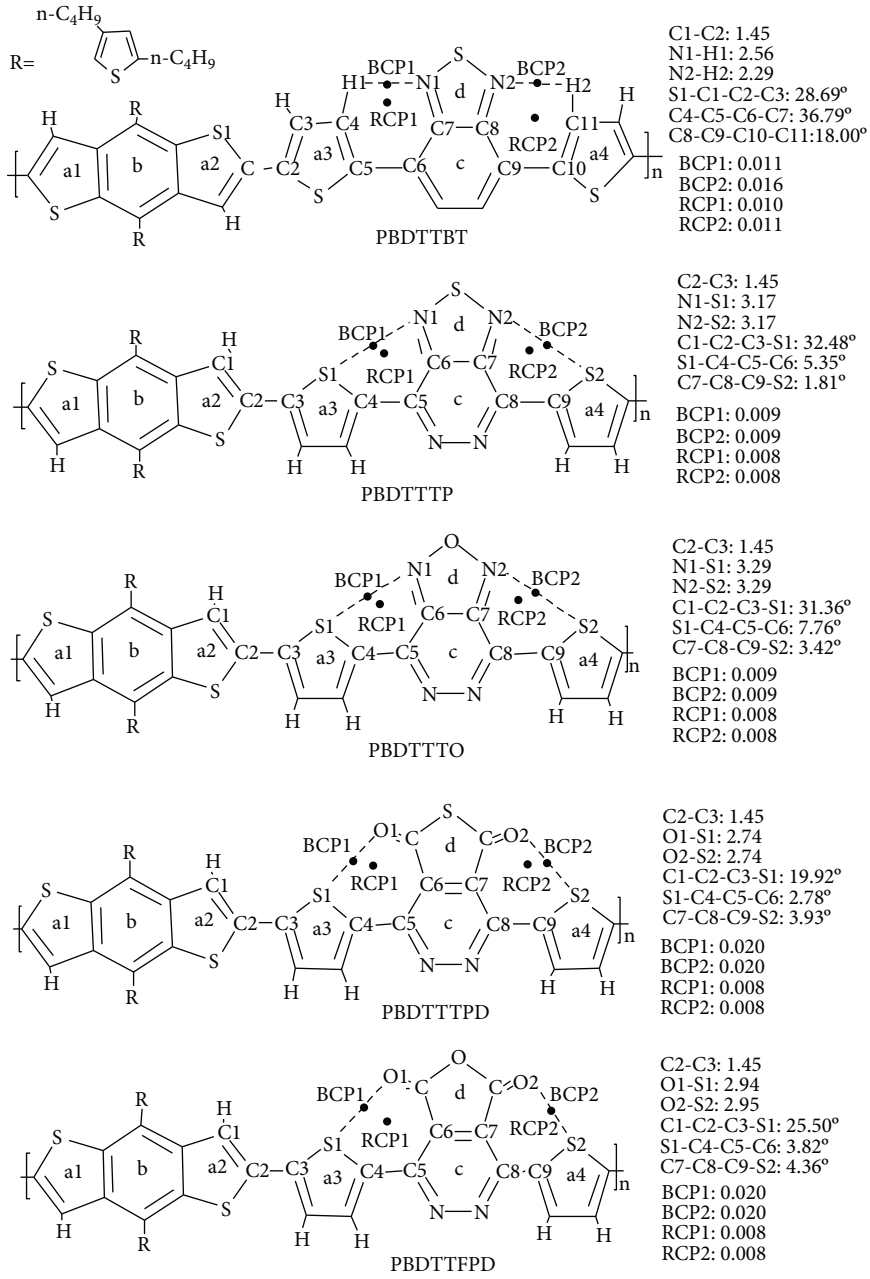

Figure 1: Structural parameters of copolymers and locations for calculated NICS.

TTP, TTO, TTPD, and TFPD) mainly contributing to LUMOs are as electron-accepting segments. Moreover, in order to quantitatively view the components of the HOMOs and LUMOs, the density of state (DOS) and partial DOS (PDOS) of monomers are calculated and given in Figure 3. As shown in Figure 3, TBT segment contributes to both HOMO and LUMO; nevertheless, BDT mainly contributes to HOMO to some degree. The DOS diagrams for other polymers show that the HOMOs are mainly contributed by BDT segments, and the LUMOs are almost entirely from TBT, TTP, TTO, TTPD, and TFPD segments.

In a word, BDT as a donor mainly contributes to HOMO and the left segments mainly contribute to LUMO, and the push-pull interactions in D-A in the four copolymers are formed.

3.2. Conjugational Properties. Generally speaking, favorable structural stability of molecule originates from its favorable conjugated properties to some degree. In order to understand the structural stability of the studied polymers, we investigate their conjugation properties.

NICS is comprehensively used to express the aromaticity of molecules because it can clearly and simply monitor the condition of ring current. Aromatic systems have pretty negative NICS values, antiaromatic systems have strongly positive NICS values, and nonaromatic cyclic systems should

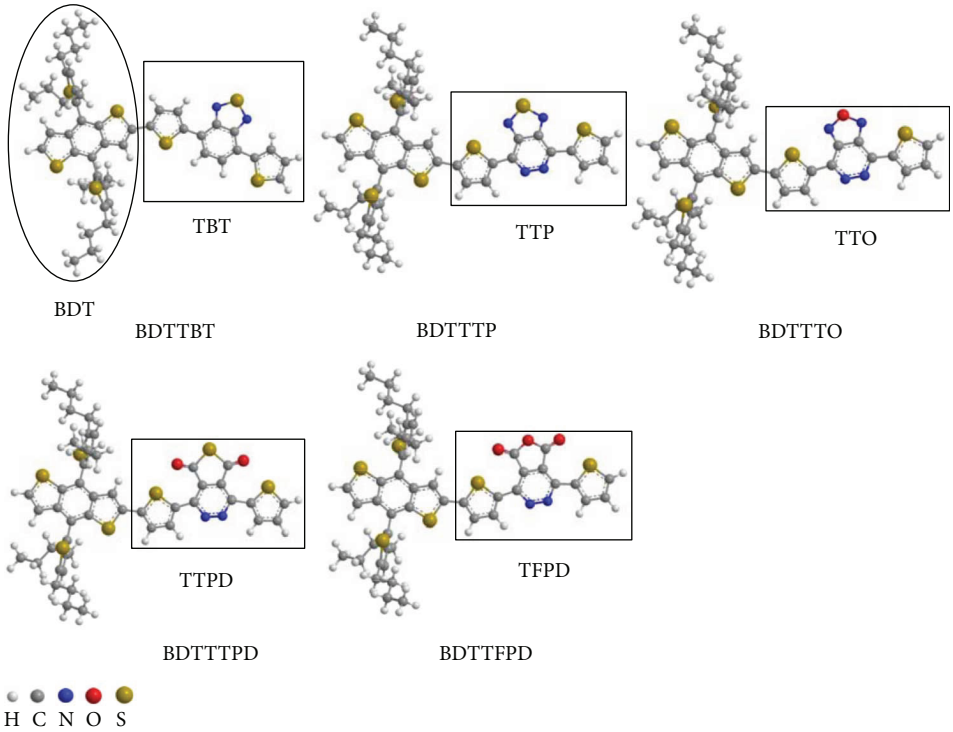

Figure 2: The stereograph of optimized parent molecules of copolymers by DFT//B3LYP/6-31G(d).

have NICS values close to zero [35, 42–44]. The NICS values for the repeated units of polymers are calculated and listed in Table 2S, and the positions of all the rings in the molecules are shown in Figure 1.

In Table 1S, the ring NICS values along the polymeric axis (a, b, and c) are more positive than the individual TH (NICS, −13.9 at B3LYP/6-31G(d) level) and benzene (NICS, −9.7 at B3LYP/6-31G(d) level), which originates from the electrons delocalizing to the whole molecule, thus, forming conjugated systems. As to the same rings, the NICS values of center rings are more negative than the terminal rings, such as the NICS values in a2 and a3 rings are more negative than those in a1 and a4, which illustrate that the ring currents mainly accumulate in the molecular center. In addition, the electrons of the molecules delocalize from donors toward acceptors along the polymeric axis because there are push-pull interactions in the systems; therefore, a2, a3, a4, and c rings are full of ring currents but a1 and b rings lack ring currents. Further, inside rings, that is, d rings, where the NICS values are most negative in respective systems, since electron-rich sulfur and nitrogen atoms in the three systems provide large ring currents. Nevertheless, the carbon atoms in PBDTTTPD and PBDTTFPD are relatively electron-deficient in comparison of nitrogen atoms, which results in small ring currents, thus leading to more positive NICS values in d rings.

Through analyzing the ring currents in RCPs, we find PBDTTTP and PBDTTTO have the same conjugation as PBDTTBT and are relatively stable copolymers.

3.3. Absorption Spectra. As shown in Figure 4(a), the experimental absorption spectrum of PBDTTBT has three absorption bands from 300 to 700 nm both in chloroform and as a solid film, and the main absorption peak of PBDTTBT is located at approximately 581 nm in solution [23]. The simulated absorption spectrum of PBDTTBT monomer at the TD-DFT/B3LYP 6-31G(d) level is depicted in Figure 4(a) for comparison, and the effect of the solvent (chloroform) within polarizable continuum model (PCM) [44] is taken into account during the calculation. The main absorption peak of calculated PBDTTBT monomer is located at 607 nm. The agreements between measured and simulated spectra are well in overall spectral shape, though their main absorption peaks are different. Furthermore, the calculated electronic transitions, absorption wavelengths (λ), oscillator strengths (f), and main configuration of PBDTTBT monomer were shown in Table 1. Herein, the $S_1 \leftarrow S_0$ electronic transition mainly comes from HOMO to LUMO (absorption process). In the process of $S_1 \leftarrow S_0$ electronic transition, charges transfer from the conjugation section of homocyclic rings along the polymeric axis to TBT section as shown in the HOMO and LUMO diagrams of PBDTTBT in Figure 1S. In comparison of the charge difference densities of the main electronic excited states of PBDTTBT in Figure 2S, we find that the charge transfer takes place from BDT to TBT, whereas the alkyl groups hardly participate in charge transfer.

At the same calculation level, the simulated absorption spectra of the four designed copolymers are given in Figure 4(b). As shown in Figure 4(b), the absorption spectra of monomers for BDTTTP and BDTTTO have two absorption bands in the range of 300–800 nm, especially the absorption bands (Q band) near to 700 nm, thus benefitting to harvesting influx photons from the sun, and the monomers

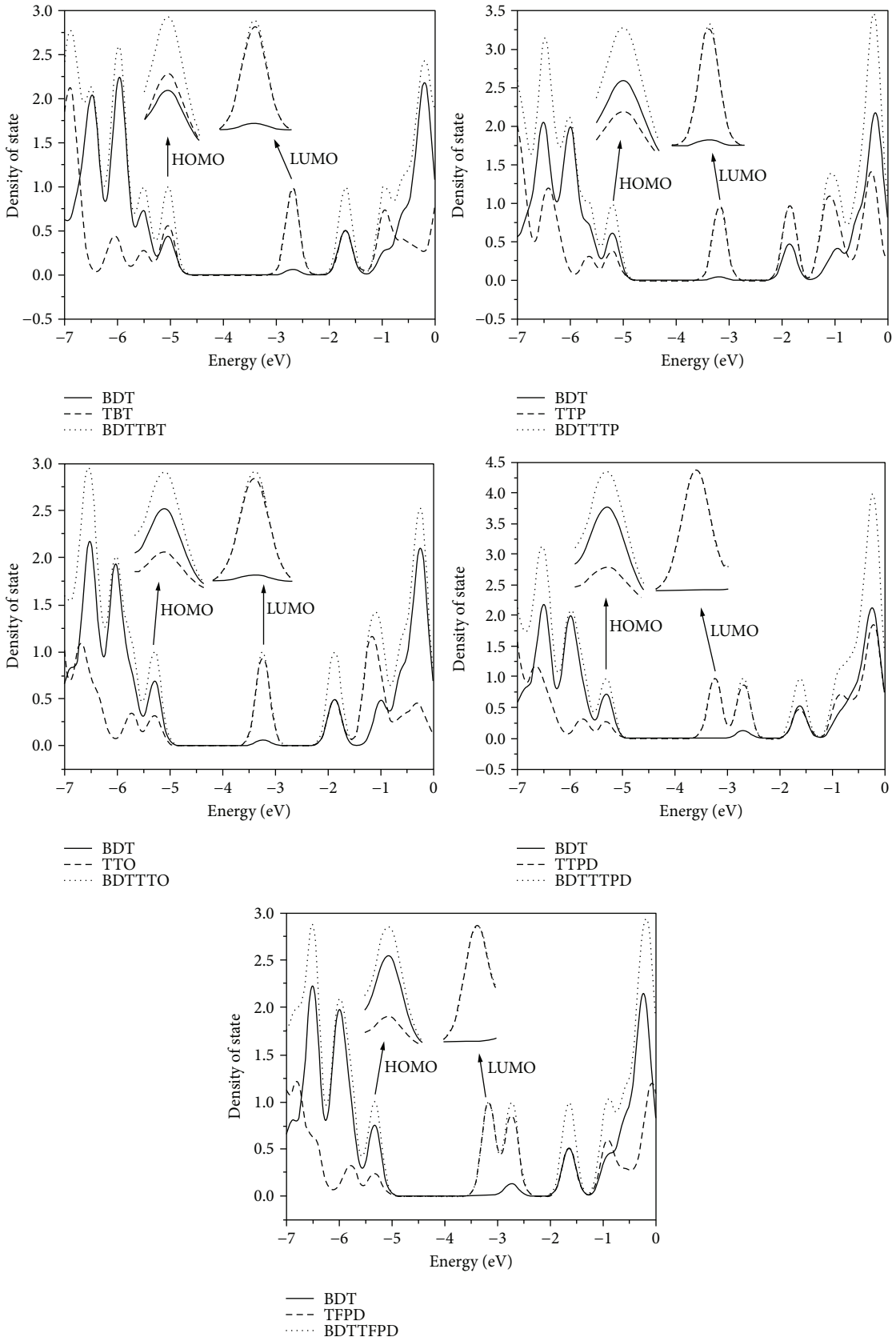

Figure 3: DOS and PDOS of monomers.

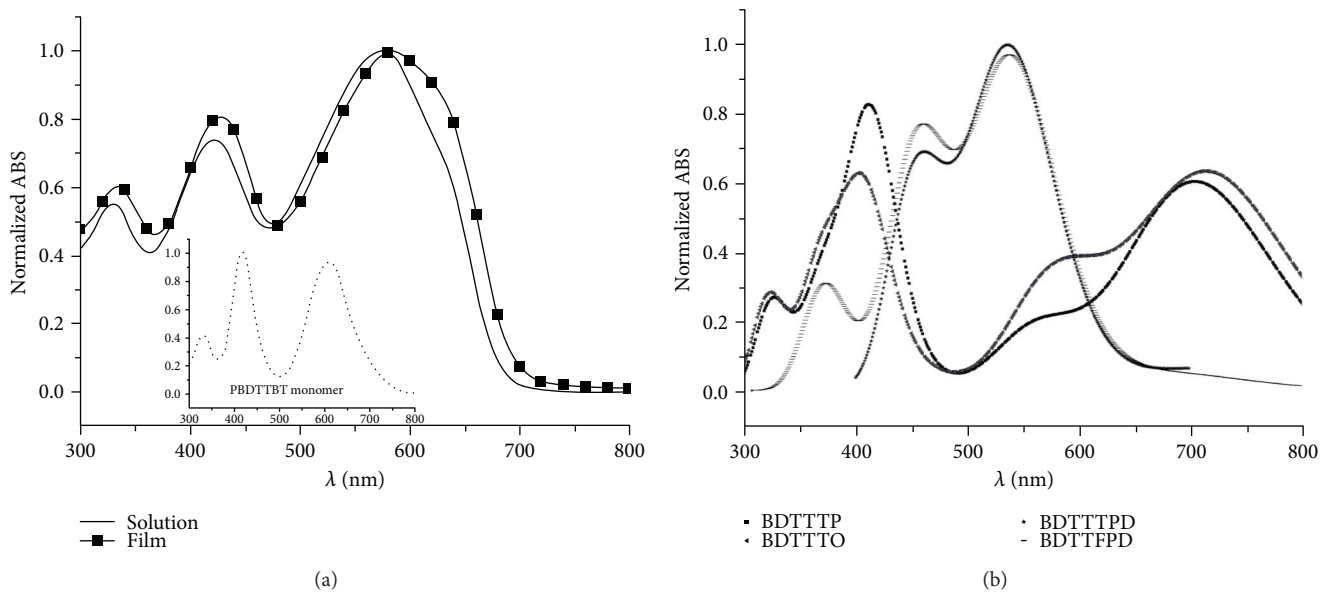

Figure 4: (a) Experimental absorption spectra of PBDTTBT as a film and in chloroform solution [23] and simulated absorption spectra of PBDTTBT monomer (the smaller one) in chloroform solution. (b) Absorption spectra of monomers of the four designed copolymers in chloroform solution.

of BDTTTPD and BDTTFPD have wide absorption bands in the range of 400–600 nm. The above results suggest that the parent molecules of designed copolymers have broad absorption in the visible region.

Moreover, the detailed maximum absorption wavelengths (λ), oscillator strengths (f), the lowest excitation energy (E^{ex}), and the main configuration of monomers are given in Table 1. In Table 1, the maximum absorption peaks of BDTTTP and BDTTTO belonging to Q bands are red-shifted compared with BDTTBT and the E^{ex} values decrease, thus benefitting electronic transition, whereas, these of BDTTTPD and BDTTFPD are blue-shifted. Generally speaking, the larger oscillator strengths (f), the larger electronic transition probability. As shown in Table 1, the oscillator strengths (f) of all the studied monomers are larger than 0.61, and that of BDTTTPD is the largest one (0.96) of all the f. Combining Figure 4 and Table 1, we find that the main configurations with the maximum wavelength of the parent molecules belong to single electron transitions and originate from HOMO to LUMO mainly assigned to $\pi \rightarrow \pi^*$ transition; as shown in Figure 1S, the electrons transfer from donor (BDT) to acceptors (TBT, TTP, TTO, TTPD, and TFPD).

In comparison to the experimental and theoretical absorption spectra of BDTTBT, we find that the PBDTTBT has wide and strong absorption spectra. Moreover, the designed copolymers have wide and strong absorption, and they have smaller transition energy in the visible region. Therefore, these designed copolymers also have the favorable ability of harvesting the flux photons from the sun.

3.4. Frontier Molecular Orbitals. The properties of frontier molecular orbitals (FMOs) of polymers seriously affect stable and photovoltaic properties. In order to harvest the maximum of the photon flux from the sun and obtain high short-circuit current (J_{SC}), the bandgap (Eg) of the polymers should lie between 1.3 and 1.9 eV [45]. Further, its HOMO energy level should be between −5.2 and− 5.8 eV if the donor can keep stable toward oxidation from air, meanwhile, its LUMO level should be between −3.7 and− 4.0 eV as shown in Figure 5. Rather, the open-circuit voltage (V_{OC}) of PSC is eventually confined by the difference between the HOMO of the donor and the LUMO of the acceptor [12, 46]. It is useful to research the molecular FMOs because the relative levels of the occupied and virtual orbitals can provide reasonable qualitative indications for processes of exciton generation and dissociation.

In the present work, we calculate the LUMO and HOMO energy levels of the five copolymers by exploring several DFT methods. Since only the values at B3LYP/6-31G(d) and B3PW91/6-31G(d) levels get close to the experimental values of PBDTTBT (the detailed calculated results are given in Table 3S in Supplementary materials); therefore, we only list the LUMO and HOMO energy levels based on the above methods in Figure 5.

In Figure 5, we can see that the value at the B3LYP/6-31G(d) level (−5.01 eV) is higher than the one at B3PW91/6-31G(d) level (−5.11 eV), and the two calculated values are higher than the experimental one (−5.31 eV). The difference between experimental and calculated values is about 0.2–0.3 eV, and the different environments between experiment and calculation should be responsible for the difference. As to the designed copolymers, the HOMO levels from B3LYP/6-31G(d) level are higher than the corresponding ones from B3PW91/6-31G(d) level as the PBDTTBT; moreover, all the HOMO levels of designed copolymers are lower than the one in PBDTTBT at the same calculated level; therefore, we predict that the experimental HOMO levels of the designed copolymers are lower than the experimental one of PBDTTBT (−5.31 eV), and the designed copolymers have stronger antioxidation properties than PBDTTBT.

Table 1: Maximum absorption wavelengths (λ), oscillator strengths (f), the lowest excitation energies, and main configuration of monomers.

Monomer	λ (nm)	f	E^{ex} (eV)	Main configuration
BDTTBT	607	0.81	2.04	HOMO → LUMO (99%)
BDTTTP	706	0.61	1.76	HOMO → LUMO (99%)
BDTTTO	718	0.63	1.73	HOMO → LUMO (100%)
BDTTTPD	538	0.96	2.30	HOMO → L + 1 (97%)
BDTTFPD	540	0.85	2.30	HOMO → L + 1 (83%)

In the formula of power conversion efficiency: $\eta = V_{OC} \times J_{SC} \times FF/P_{in}$, the three parameters, V_{OC}, JSC, and FF, determine the solar cell performance directly. The parameter, open-circuit voltage (V_{OC}) formed in the process of carrier transport, is popularly used to estimate the maximum PCE [9]. As shown in Figure 5, the experimental V_{OC} (exp) is gained when the J_{SC} is equal to zero in J-V curves. There are two models to describe theoretical V_{OC}: one is the metal-insulator-metal (MIM) model [47], the other model is the HOMO^D-LUMO^A offset model [9, 48]. Moreover, Lo et al. suggest that V_{oc} is described by a combined MIM model with HOMO^D-LUMO^A offset model; in that model, they find that when the work function deviation ($\Delta\phi_{electrodes}$) of ITO from Al electrode is in the range− 3 and 0 eV, V_{oc} enlarges linearly with $\Delta\phi_{electrodes}$ as prescribed by the MIM model. Outside this range V_{oc} depends on HOMO^D-LUMO^A offset model [49]. In the work, we assume that $\Delta\phi_{electrodes}$ is outside the range −3 and 0 eV; thus, we employed the HOMO^D-LUMO^A offset model, and the V_{oc} of a conjugated polymer-PC$_{70}$BM solar cell can be estimated by [9]

$$V_{oc} = \frac{1}{e}\left(\left|E^{\text{Donor}}\text{HOMO}\right| - \left|E^{\text{PCBM}}\text{LUMO}\right|\right) - 0.3\,\text{V}, \quad (1)$$

where e is the elementary charges, E^{PCBM}LUMO is equal to −4.3 eV (PC$_{70}$BM), and the 0.3 V is an empirical factor to offset the exciton binding energy [50]. In comparison with the experimental and simulated V_{OC} values of PBDTTBT, the simulated V_{OC} is lower than the measured one by 0.51 (at the B3LYP/6-31G* level) and 0.41 eV (at the B3PW91/6-31G* level), which primarily originates from the HOMO level difference between simulation and experiment. For the sake of comparing the V_{OC} size of designed polymers with PBDTTBT, we also simulate the V_{OC} values of designed polymers by HOMO^D-LUMO^A offset model. As shown in Figure 5, the V_{oc} of the designed copolymers are larger than the one of PBDTTBT based on either B3LYP or B3PW91 functional resulting from the deeper HOMO levels of designed copolymers. Therefore, the four designed copolymers are promising to improve the V_{oc} relative to PBDTTBT in the experiment.

3.5. Charge Transfer Properties. On the basis of band-like theory, the bandwidth (BW) and electron effective mass (m^*) are beneficial parameters for predicting the hole and electron-transporting ability of polymers [51–53]. The effective mass of carrier at the band edge representing mobility was gained as the square of $\hbar$ multiplied by the reciprocal of the curvature from $E(k)$ with k, and the formulation is defined as

$$\frac{1}{m^*} = \frac{1}{\hbar}\left(\frac{\partial^2 E(k)}{\partial k^2}\right). \quad (2)$$

The kinetic model of mobility (μ) is given by the following formula:

$$\mu = \frac{eT}{m^*}. \quad (3)$$

The BW and m^* data are given in Table 2. According to the band theory, the wider the BW, the smaller the effective mass, and the larger the kinetic model of mobility [54]. The data in Table 2 investigate that PBDTTBT has wide valence band (0.25 eV) and small m^* (-4.45×10^4). By using the same methods as PBDTTBT, we calculate the bandwidths and effective masses for designed polymers and list the data in Table 2.

The data in Table 2 investigate that all the designed polymers have wider valence bands (PBDTTTP: 0.38 eV, PBDTTTO: 0.34 eV, PBDTTTPD: 0.33 eV, and PBDTTFPD: 0.30 eV) and smaller m^* (PBDTTTP: -2.91×10^4, PBDTTTO: -2.91×10^4, PBDTTTPD: -2.91×10^4, and PBDTTFPD: -3.29×10^4) in comparison of PBDTTBT. Moreover, PBDTTTP and PBDTTTO also have wider conduction bands and smaller m^* than PBDTTBT; however, PBDTTTPD and PBDTTFPD have narrower conduction bandwidths and valence bandwidths through comparing PBDTTBT. The above investigations indicate that all the designed polymers have better hole transport properties than PBDTTBT; further, PBDTTTP and PBDTTTO have better electron transport properties than PBDTTBT through conduction band properties.

3.6. Exciton Dissociation. After exciton formation, excitons transport to the donor-acceptor interface. In the interface, exciton dissociation competes with possible recombination. The rates of exciton dissociation and charge recombination are evaluated using the Marcus theory [55]:

$$K = \sqrt{\frac{4\pi^3}{h^2 \lambda k_B T}}\left|V_{DA}\right|^2 \exp\left(-\frac{(\Delta G + \lambda)^2}{4\lambda k_B T}\right), \quad (4)$$

where λ is the reorganization energy, V_{DA} is the electronic coupling between donor and acceptor, ΔG is the free energy change for the electron transfer reaction, k_B is the Boltzmann constant, h is the Planck's constant, and T is the temperature (we set $T = 298$ K in our calculations). In the exciton dissociation and charge recombination, $\Delta G = \Delta G_{CT}$ and $\Delta G = \Delta G_{CR}$, respectively. The electronic coupling can be calculated through employing the generalized Mulliken-Hush (GMH) model [56]. In the work, we calculate the ratio of exciton dissociation rate (K_{CT}) and charge recombination rate (K_{CR}); therefore, the parameters λ, ΔG_{CT}, and ΔG_{CR} are mainly studied.

The reorganization energy λ is composed of inner and outer reorganization energy. The inner originates from the

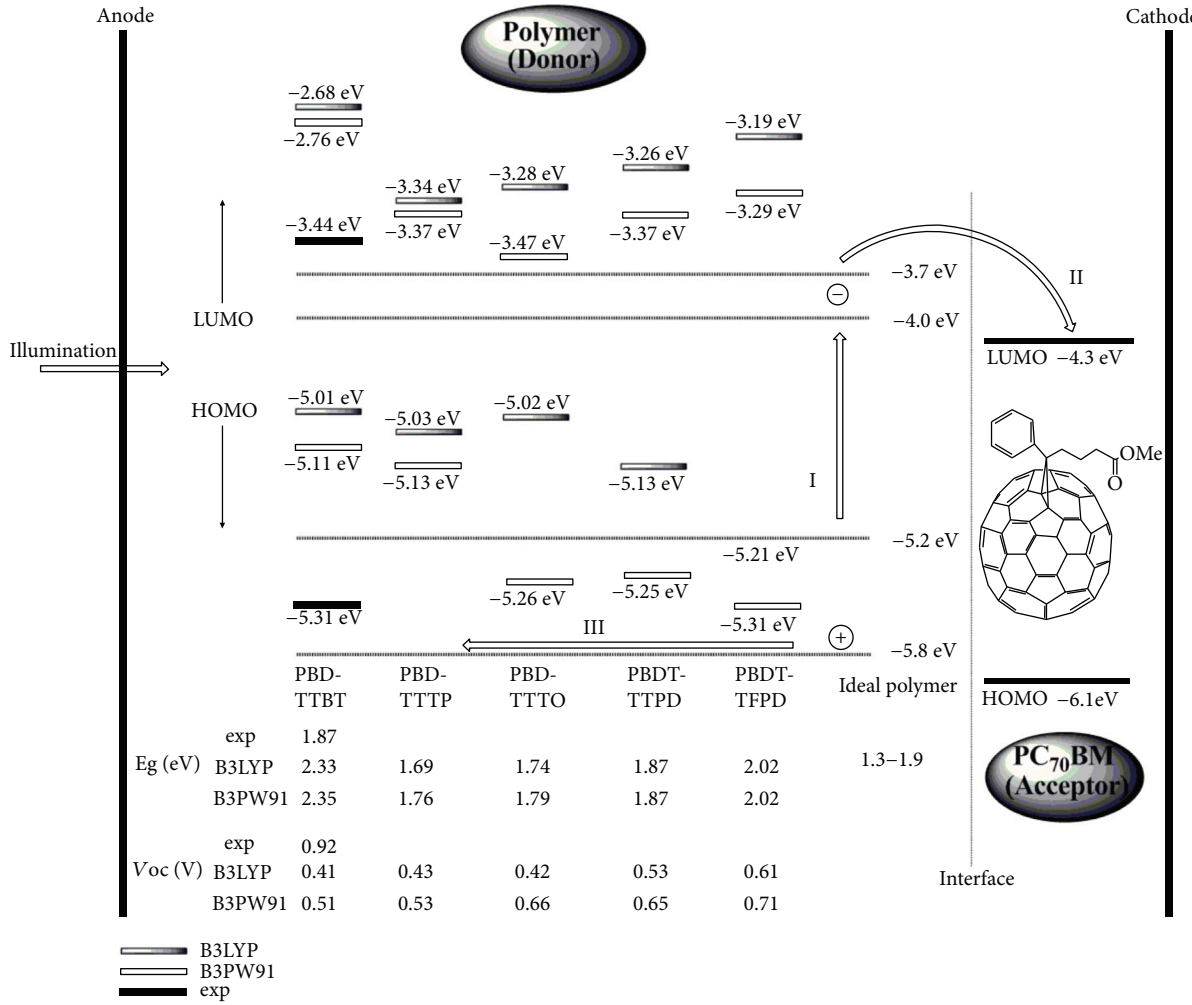

Figure 5: Photoelectric conversion process diagram and energy levels of polymers. (exp represents the values of the experimental measures).

Table 2: Bandwidth (eV) and effective mass (m^*).

Polymer	Conduction band		Valance band	
	BW	$m^*(\times 10^4)$	BW	$m^*(\times 10^4)$
PBDTTBT	0.08	9.45	0.25	−4.45
PBDTTTP	0.13	5.82	0.38	−2.91
PBDTTTO	0.16	5.04	0.34	−2.91
PBDTTTPD	0.03	12.6	0.33	−2.91
PBDTTFPD	0.03	12.6	0.30	−3.29

change in equilibrium geometry of the donor (D) and acceptor (A) sites consecutive to the gain or loss of electronic charge upon electron transfer. The outer arises from electronic and nuclear polarization/relaxation of the surrounding medium. The inner is composed of two terms

$$\lambda = \lambda_1(\mathrm{A}) + \lambda_2(\mathrm{D}), \tag{5}$$

$$\lambda_1(\mathrm{A}) = E(\mathrm{A}^-) - E(\mathrm{A}), \tag{6}$$

$$\lambda_2(\mathrm{D}) = E(\mathrm{D}) - E(\mathrm{D}^+), \tag{7}$$

Here, $E(\mathrm{A}^-)$ and $E(\mathrm{A})$ are the energies of the neutral acceptor A at the anionic geometry and optimal ground-state geometry, respectively, and $E(\mathrm{D})$ and $E(\mathrm{D}^+)$ are, accordingly, the energies of the radical cation at the neutral geometry and optimal cation geometry. In the condition of corrole-fullerene dyads in nonpolar solvent, the overall reorganization energy is 0.5 eV. Therefore, we assume here a value of 0.5 eV for the overall reorganization energy in our calculations. All the reorganization energies of researched polymers are given in Table 3. The reorganization energy of PBDTTBT, PBDTTTP, PBDTTTO, and PBDTTFPD is 0.69 eV except for 0.67 eV of PBDTTTPD. The ΔG_{CR} can be estimated with

$$\Delta G_{CR} = EI_P(\mathrm{D}) - E_{EA}(\mathrm{A}), \tag{8}$$

where $E_{IP}(\mathrm{D})$ and $E_{EA}(\mathrm{A})$ are the ionization potential of the donor and electron affinity of the acceptor, respectively. The calculated ΔG_{CR} values are successively −1.76 eV, −1.92 eV, −2.10 eV, −2.09 eV, −2.15 eV for PBDTTBT, PBDTTTP, PBDTTTO, PBDTTTPD, PBDTTFPD shown in Table 3.

Table 3: Reorganization (λ), exciton dissociation energy (ΔG_{CT}), charge recombination energy (ΔG_{CR}), the ratio of exciton dissociation rate and charge recombination rate ($K_{CT}:K_{CR}$), and external quantum efficiency (EQE).

Polymer	PBDTTBT	PBDTTTP	PBDTTTO	PBDTTTPD	PBDTTFPD
λ (eV)	0.69	0.69	0.69	0.67	0.69
ΔG_{CR} (eV)	−1.76	−1.92	−2.10	−2.09	−2.15
ΔG_{CT} (eV)	−0.31	−0.14	−0.29	−0.21	−0.15
$K_{CT}:K_{CR}$	1.62×10^{6}	2.36×10^{7}	2.13×10^{11}	1.90×10^{11}	2.70×10^{11}
EQE	1.3%	4.1%	3.8%	3.7%	3.6%

As shown in Table 3, we also estimated the ΔG_{CT} values in accordance with Rehm-Weller equation [57]

$$\Delta G_{CT} = -\Delta G_{CR} - \Delta E_{0-0} - E_b \quad (9)$$

where ΔE_{0-0} is the energy of the lowest excited state of free-base donor and E_b is the exciton binding energy. The calculated ΔG_{CT} are depicted in Table 3, and they are −0.31 eV (PBDTTBT), −0.14 eV (PBDTTTP), −0.29 eV (PBDTTTO), −0.21 eV (PBDTTTPD), and −0.15 eV (PBDTTFPD). According to the estimated values of λ, ΔG_{CR}, and ΔG_{CT}, we calculate the ratio of exciton dissociation rate and charge recombination rate ($K_{CT}:K_{CR}$), and the data of $K_{CT}:K_{CR}$ listed in Table 3 indicate that PBDTTBT has large $K_{CT}:K_{CR}$ (1.62×10^{6}). Moreover, the designed polymers PBDTTTP, PBDTTTO, PBDTTPD, and PBDTTFPD have larger $K_{CT}:K_{CR}$ values (2.36×10^{7}, 2.13×10^{11}, 1.90×10^{11}, and 2.70×10^{11}, resp.) than PBDTTBT, which suggest that the designed polymers have better exciton abilities than PBDTTBT.

3.7. External Quantum Efficiency. According to the studies of Scharber et al. in 2006 [9], the external quantum efficiency (EQE) of solar cell is related to the bandgap energy and frontier molecular orbital energy levels under the assumptions that any contribution to the short-circuit current from photons absorbed by the fullerene is neglected and the *FF* is set to 65%. The calculated EQE data of all the studied polymers are listed in Table 3. From Table 3, we can see that the EQE values of all the designed polymers are larger than 3.5% (especially PBDTTTP: 4.1%) and larger than that of PBDTTBT (1.3%).

In a word, the designed polymers, especially PBDTTTP, have better photovoltaic properties than PBDTBT; therefore, the designed polymers are the promising candidates for polymer BHJ.

4. Conclusions

In this contribution, density functional theory (DFT) and time-dependent DFT (TD-DFT) calculations have been employed to model PBDTTBT to rationalize the relationship between the experimentally observed properties and the structural features in polymer BHJ. Besides, according to PBDTTBT, we design four benzodithiophene-like copolymers, PBDTTTP, PBDTTTO, PBDTTTPD, and PBDTTFPD. In order to investigate their potentials as donors in polymer BHJ based on PC70BM, several parameters of determining the performance of solar cells, structural properties, absorption spectra, frontier molecular orbitals, charge transfer properties, and external quantum efficiency have been researched. PBDTTBT's well conjugation benefits its good stability, and its well photovoltaic performance mainly results from its strong absorption spectra in the range of visible light, appropriate FMO levels, well charge transport, and favorable exciton dissociation. Comparing the four designed copolymers with PBDTTBT, we conclude that the four designed copolymers have stronger exciton dissociation ability and larger open-circuit voltage and external quantum efficiencies. Consequently, the four designed copolymers are promising candidates for polymer BHJ solar cells.

Data Availability

The data used to support the findings of this study are available from the corresponding author upon request.

Conflicts of Interest

The authors declare that they have no conflicts of interest.

Acknowledgments

This work was supported by the Research Project from Chongqing Committee of Education (KJ15012020), "Chunhui Plan" Cooperating Project from the Ministry of Education (Z2015143), Natural Science Foundation of Yangtze Normal University (Grant no.2103XJQN007), and Chinese Scholarship Council. The authors are grateful to the anonymous referees for their suggestions.

Supplementary Materials

Table 1S: BCP properties, Wiberg bond index, and electronic configurations for bonding orbitals of central bonds. Table 2S: NICS for polymers at RCPs. Table 3S: HOMO and LUMO energy levels and bandgaps from the experiment and calculation for PBDTTBT. Figure 1S: HOMO (H) and LUMO (L) diagrams for monomers and dimers. Figure 2S: charge difference densities of the main electronic excited states of PBDTTBT. Figure 3S: orbital interaction diagrams (B3LYP/6-31G *) for dimers. *(Supplementary Materials)*

References

[1] F. C. Krebs, M. Jorgensen, K. Norrman et al., "A complete process for production of flexible large area polymer solar cells entirely using screen printing—first public demonstration,"

Solar Energy Materials and Solar Cells, vol. 93, no. 4, pp. 422–441, 2009.

[2] F. C. Krebs, "Polymer solar cell modules prepared using roll-to-roll methods: knife-over-edge coating, slot-die coating and screen printing," *Solar Energy Materials and Solar Cells*, vol. 93, no. 4, pp. 465–475, 2009.

[3] F. C. Krebs, S. A. Gevorgyan, and J. Alstrup, "A roll-to-roll process to flexible polymer solar cells: model studies, manufacture and operational stability studies," *Journal of Materials Chemistry*, vol. 19, no. 30, pp. 5442–5451, 2009.

[4] F. C. Krebs, "All solution roll-to-roll processed polymer solar cells free from indium-tin-oxide and vacuum coating steps," *Organic Electronics*, vol. 10, no. 5, pp. 761–768, 2009.

[5] B. C. Thompson and J. M. J. Fréchet, "Polymer–fullerene composite solar cells," *Angewandte Chemie International Edition*, vol. 47, no. 1, pp. 58–77, 2008.

[6] C. Liang, Y. Wang, D. Li, X. Ji, F. Zhang, and Z. He, "Modeling and simulation of bulk heterojunction polymer solar cells," *Solar Energy Materials and Solar Cells*, vol. 127, no. 4, pp. 67–86, 2014.

[7] A. Hadipour, B. de Boer, J. Wildeman et al., "Solution-processed organic tandem solar cells," *Advanced Functional Materials*, vol. 16, no. 14, pp. 1897–1903, 2006.

[8] J. Y. Kim, K. Lee, N. E. Coates et al., "Efficient tandem polymer solar cells fabricated by all-solution processing," *Science*, vol. 317, no. 5835, pp. 222–225, 2007.

[9] M. C. Scharber, D. Mühlbacher, M. Koppe et al., "Design rules for donors in bulk-heterojunction solar cells—towards 10% energy-conversion efficiency," *Advanced Materials*, vol. 18, no. 6, pp. 789–794, 2006.

[10] E. Bundgaard and F. C. Krebs, "Low band gap polymers for organic photovoltaics," *Solar Energy Materials and Solar Cells*, vol. 91, no. 11, pp. 954–985, 2007.

[11] M. M. Wienk, J. M. Kroon, W. J. H. Verhees et al., "Efficient methano[70]fullerene/MDMO-PPV bulk heterojunction photovoltaic cells," *Angewandte Chemie International Edition*, vol. 42, no. 29, pp. 3371–3375, 2003.

[12] C. J. Brabec, A. Cravino, D. Meissner et al., "Origin of the open circuit voltage of plastic solar cells," *Advanced Functional Materials*, vol. 11, no. 5, pp. 374–380, 2001.

[13] S. A. Backer, K. Sivula, D. F. Kavulak, and J. M. J. Frechet, "High efficiency organic photovoltaics incorporating a new family of soluble fullerene derivatives," *Chemistry of Materials*, vol. 19, no. 12, pp. 2927–2929, 2007.

[14] F. B. Kooistra, J. Knol, F. Kastenberg et al., "Increasing the open circuit voltage of bulk-heterojunction solar cells by raising the LUMO level of the acceptor," *Organic Letters*, vol. 9, no. 4, pp. 551–554, 2007.

[15] A. J. Campbell, D. D. C. Bradley, and H. Antoniadis, "Dispersive electron transport in an electroluminescent polyfluorene copolymer measured by the current integration time-of-flight method," *Applied Physics Letters*, vol. 79, no. 14, pp. 2133–2135, 2001.

[16] Y. J. Cheng, S. H. Yang, and C. S. Hsu, "Synthesis of conjugated polymers for organic solar cell applications," *Chemical Reviews*, vol. 109, no. 11, pp. 5868–5923, 2009.

[17] J. Hou, H.-Y. Chen, S. Zhang et al., "Synthesis of a low band gap polymer and Its application in highly efficient polymer solar cells," *Journal of the American Chemical Society*, vol. 131, no. 43, pp. 15586-15587, 2009.

[18] H.-Y. Chen, J. Hou, S. Zhang et al., "Polymer solar cells with enhanced open-circuit voltage and efficiency," *Nature Photonics*, vol. 3, no. 11, pp. 649–653, 2009.

[19] H. Pan, Y. Li, Y. Wu et al., "Low-temperature, solution-processed, high-mobility polymer semiconductors for thin-film transistors," *Journal of the American Chemical Society*, vol. 129, no. 14, pp. 4112-4113, 2007.

[20] H. Pan, Y. Wu, Y. Li et al., "Benzodithiophene copolymer—a low-temperature, solution-processed high-performance semiconductor for thin-film transistors," *Advanced Functional Materials*, vol. 17, no. 17, pp. 3574–3579, 2007.

[21] J. Hou, M.-H. Park, S. Zhang, L.-M. Chen, J.-H. Li, and Y. Yang, "Bandgap and molecular energy level control of conjugated polymer photovoltaic materials based on benzo[1,2-*b*:4,5-*b*′]dithiophene," *Macromolecules*, vol. 41, no. 16, pp. 6012–6018, 2008.

[22] L. Huo, J. Hou, H.-Y. Chen et al., "Bandgap and molecular level control of the low-bandgap polymers based on 3,6-Dithiophen-2-yl-2,5-dihydropyrrolo[3,4-*c*]pyrrole-1,4-dione toward highly efficient polymer solar cells," *Macromolecules*, vol. 42, no. 17, pp. 6564–6571, 2009.

[23] L. Huo, J. Hou, S. Zhang, H.-Y. Chen, and Y. Yang, "A polybenzo[1,2-b:4,5-*b*′]dithiophene derivative with deep HOMO level and its application in high-performance polymer solar cells," *Angewandte Chemie International Edition*, vol. 49, no. 8, pp. 1500–1503, 2010.

[24] I. T. Lima, L. Sousa, R. d. S. Freitas, L. A. Ribeiro Junior, R. T. de Sousa Júnior, and D. A. de Silva Filho, "A DFT study of a set of natural dyes for organic electronics," *Journal of Molecular Modeling*, vol. 23, no. 12, p. 343, 2017.

[25] T. Mohr, V. Aroulmoji, R. S. Ravindran et al., "DFT and TD-DFT study on geometries, electronic structures and electronic absorption of some metal free dye sensitizers for dye sensitized solar cells," *Spectrochimica Acta Part A: Molecular and Biomolecular Spectroscopy*, vol. 135, pp. 1066–1073, 2015.

[26] Y. Li, T. Pullerits, M. Zhao, and M. Sun, "Theoretical characterization of the $PC_{60}BM$:PDDTT Model for an organic solar cell," *The Journal of Physical Chemistry C*, vol. 115, no. 44, pp. 21865–21873, 2011.

[27] X. H. Xie, W. Shen, R. X. He, and M. Li, "A density functional study of furofuran polymers as potential materials for polymer solar cells," *Bulletin of the Korean Chemical Society*, vol. 34, no. 10, pp. 2995–3004, 2013.

[28] G. Parr and W. Yang, *Density-Functional Theory of Atoms and Molecules*, University Press, Oxford, NY, USA, 1989.

[29] A. D. Becke, "Density-functional thermochemistry. III. The role of exact exchange," *The Journal of Chemical Physics*, vol. 98, no. 7, pp. 5648–5652, 1993.

[30] C. Lee, W. Yang, and R. G. Parr, "Development of the Colle-Salvetti correlation-energy formula into a functional of the electron density," *Physical Review B*, vol. 37, no. 2, pp. 785–789, 1988.

[31] K. N. Kudin and G. E. Scuseria, "Linear-scaling density-functional theory with Gaussian orbitals and periodic boundary conditions: efficient evaluation of energy and forces via the fast multipole method," *Physical Review B*, vol. 61, no. 24, pp. 16440–16453, 2000.

[32] J. P. Perdew, *Electronic Structure of Solids '91*, P. Ziesche and H. Eschrig, Eds., Akademie Verlag, Berlin, 1991.

[33] M. J. Frisch, G. W. Trucks, H. B. Schlegel et al., *Gaussian 09, Revision A. 02*, Gaussian, Inc., Wallingford, CT, USA, 2009.

[34] R. F. W. Bader, *Atoms in Molecules, A Quantum Theory; International Series of Monographs in Chemistry*, vol. 22, Oxford University Press, Oxford, UK, 1990.

[35] P. v. R. Schleyer, C. Maerker, A. Dransfeld, H. Jiao, and N. J. R. van Eikema Hommes, "Nucleus-independent chemical shifts: a simple and efficient aromaticity probe," *Journal of the American Chemical Society*, vol. 118, no. 26, pp. 6317-6318, 1996.

[36] W. Shen, M. Li, R. He, J. Zhang, and W. Lei, "The electronic and structural properties of nonclassical bicyclic thiophene: monomer, oligomer and polymer," *Polymer*, vol. 48, no. 13, pp. 3912–3918, 2007.

[37] J. E. Carpenter and F. Weinhold, "Analysis of the geometry of the hydroxymethyl radical by the "different hybrids for different spins" natural bond orbital procedure," *Journal of Molecular Structure: THEOCHEM*, vol. 169, pp. 41–62, 1988.

[38] A. E. Reed, L. A. Curtiss, and F. Weinhold, "Intermolecular interactions from a natural bond orbital, donor-acceptor viewpoint," *Chemical Reviews*, vol. 88, no. 6, pp. 899–926, 1988.

[39] J. P. Foster and F. Weinhold, "Natural hybrid orbitals," *Journal of the American Chemical Society*, vol. 102, no. 24, pp. 7211–7218, 1980.

[40] A. E. Reed, R. B. Weinstock, and F. Weinhold, "Natural population analysis," *The Journal of Chemical Physics*, vol. 83, no. 2, pp. 735–746, 1985.

[41] S. I. Gorelsky and A. B. P. Lever, "Electronic structure and spectra of ruthenium diimine complexes by density functional theory and INDO/S. Comparison of the two methods," *Journal of Organometallic Chemistry*, vol. 635, no. 1-2, pp. 187–196, 2001.

[42] Y. Fu, W. Shen, and M. Li, "Theoretical analysis on the electronic structures and properties of PPV fused with. Electron-withdrawing unit: monomer, oligomer and polymer," *Polymer*, vol. 49, no. 10, pp. 2614–2620, 2008.

[43] P. von Ragué Schleyer, H. Jiao, N. J. R. van Eikema Hommes, V. G. Malkin, and O. L. Malkina, "An evaluation of the aromaticity of inorganic rings: refined evidence from magnetic properties," *Journal of the American Chemical Society*, vol. 119, no. 51, pp. 12669-12670, 1997.

[44] P. Rague von Schleyer and H. Jiao, "What is aromaticity?," *Pure and Applied Chemistry*, vol. 68, no. 2, pp. 209–218, 1996.

[45] R. Kroon, M. Lenes, J. C. Hummelen, P. W. M. Blom, and B. de Boer, "Small bandgap polymers for organic solar cells (*polymer material development in the last 5 years*)," *Polymer Reviews*, vol. 48, no. 3, pp. 531–582, 2008.

[46] L. J. A. Koster, V. D. Mihailetchi, R. Ramaker, and P. W. M. Blom, "Light intensity dependence of open-circuit voltage of polymer:fullerene solar cells," *Applied Physics Letters*, vol. 86, no. 12, pp. 123509/1–123509/3, 2005.

[47] V. D. Mihailetchi, P. W. M. Blom, J. C. Hummelen, and M. T. Rispens, "Cathode dependence of the open-circuit voltage of polymer: fullerene bulk heterojunction solar cells," *Journal of Applied Physics*, vol. 94, no. 10, pp. 6849–6854, 2003.

[48] C. W. Bauschlicher Jr. and J. W. Lawson, "Current-voltage curves for molecular junctions: the effect of substituents," *Physical Review B*, vol. 75, article 115406, 2007.

[49] M. F. Lo, T. W. Ng, T. Z. Liu et al., "Limits of open circuit voltage in organic photovoltaic devices," *Applied Physics Letters*, vol. 96, no. 11, p. 113303, 2010.

[50] J. L. Bredas, D. Beljonne, V. Coropceanu, and J. Cornil, "Charge-transfer and energy-transfer processes in π-conjugated oligomers and polymers: a molecular picture," *Chemical Reviews*, vol. 104, no. 11, pp. 4971–5004, 2004.

[51] R. C. Haddon, T. Siegrist, R. M. Fleming, P. M. Bridenbaugh, and R. A. Laudise, "Band structures of organic thin-film transistor materials," *Journal of Materials Chemistry*, vol. 5, no. 10, pp. 1719–1724, 1995.

[52] J. Cornil, J. P. Calbert, and J. L. Brédas, "Electronic structure of the pentacene single crystal: relation to transport properties," *Journal of the American Chemical Society*, vol. 123, no. 6, pp. 1250-1251, 2001.

[53] Y. C. Cheng, R. J. Silbey, D. A. da Silva Filho, J. P. Calbert, J. Cornil, and J. L. Brédas, "Three-dimensional band structure and bandlike mobility in oligoacene single crystals: a theoretical investigation," *The Journal of Chemical Physics*, vol. 118, no. 8, pp. 3764–3774, 2003.

[54] J. G. Zhu, W. X. Zheng, J. G. Zheng, X. S. Sun, and H. T. Wang, *Solid Physics*, Science Press, Beijing, China, 2005.

[55] R. A. Marcus, "Electron transfer reactions in chemistry: theory and experiment (Nobel lecture)," *Angewandte Chemie International Edition*, vol. 32, no. 8, pp. 1111–1121, 1993.

[56] A. A. Voityuk, "Estimation of electronic coupling in π-stacked donor-bridge-acceptor systems: correction of the two-state model," *The Journal of Chemical Physics*, vol. 124, no. 6, article 064505, 2006.

[57] G. J. Kavarnos and N. J. Turro, "Photosensitization by reversible electron transfer: theories, experimental evidence, and examples," *Chemical Reviews*, vol. 86, no. 2, pp. 401–449, 1986.

Hindawi
International Journal of Polymer Science
Volume 2018, Article ID 8190190, 10 pages
https://doi.org/10.1155/2018/8190190

Research Article

Thermal and Electrical Conductivity of Unsaturated Polyester Resin Filled with Copper Filler Composites

Kemal Yaman and Özer Taga

The Scientific and Technological Research Council of Turkey, Defense Industries Research and Development Institute (TÜBİTAK SAGE), 06261 Ankara, Turkey

Correspondence should be addressed to Kemal Yaman; kemal.yaman@tubitak.gov.tr

Received 28 December 2017; Revised 19 February 2018; Accepted 11 March 2018; Published 29 April 2018

Academic Editor: Zhiyuan Xiong

Thermal and electrical conductivity of unsaturated polyester resin with copper filler composite material are investigated both theoretically and experimentally. In the experiments, polyester matrix is combined with dendrite-shape copper to determine the effects of both filler size and content on thermal and electrical conductivity, respectively. It is observed that the increase in the concentration causes the thermal and electrical conductivity of composite mixture to grow up. It has also been observed that the both thermal and electrical conductivity increase with increasing filler particle size.

1. Introduction

Nowadays in many applications, thermal and electrically conductive polymer-based composites can replace metals. This technology is widely used because it introduces a new material that includes the thermal, insulation, and electrical properties of polymer materials. The advantages of polymers over metals are low density, corrosion and oxidation resistance, lightness, electromagnetic interference (EMI) protection, higher chemical resistance, and higher producibility. These superior features can be easily adjusted to different and widely applications [1, 2].

Too many studies in the literature are investigating the addition of nonpolymeric fillers to improve the physical properties of polymer. The addition of fillers with high thermal and electrical properties increases the thermal and electrical conductivity beyond the neat resin of the composite but cannot reach the level of pure filler material. The main motivation in this study is the theoretical and experimental investigation of the effects of particle size and concentration of dendritically shaped copper particles used as filler materials on thermal and electrical conductivity. Some of the existing studies examined in this subject are summarized as follows.

In a similar study, Choi et al. [1] investigate the thermal conductivity of polyacrylate matrix aluminum and multiwalled carbon nanotube filled composites. For the fixed filler concentration, the composite loaded with 13 μm aluminum dust had a higher thermal conductivity than the 3 μm powder, and the composite filled with the two powder mixtures showed a synergistic effect on the thermal conductivity. The thermal conductivity of the composites strongly depended on the size and content of fillers. Moreira et al. [3] used unsaturated polyester resin (UPR) as binder and alumina and tenorite (copper oxide) as conductive particles in nanosize. The results showed that the thermal conductivity increases with particle concentration, as expected.

Agrawal and Satapathy [4] have proposed a new theoretical method to calculate the one-dimensional heat conduction, and thermal conductivity of typical particulate filled polymer composite systems. In their experimental work, epoxy binder was applied with aluminum nitrite filler material. The thermal conductivity of the composite increases with the addition of filler particle and the rate of increase of thermal conductivity is rapid for high volume fraction, that is, above 35% as compared with low volume fraction. In another study in which both thermal and electrical conductivities were examined together, Zhou et al. [5] reported that the thermal and electrical conductivity are related to the particulate shape and size as well as the added particle concentration. At higher filler loads, the thermal conductivity

has increased dramatically. Heat-conductive aluminum particles encapsulated by a polymer matrix could not contact each other at a low filler loading, resulting in the low thermal conductivity. This result is due to the high interfacial thermal contact resistance between the filler powder and the polymer matrix. The thermal and electrical conductivities of PVDF with flaky Al mixture composite is higher than spherical shape filler one. The thermal conductivity of the composite was found to be four times higher than the neat matrix for nickel-HDPE matrix composite [6].

The measurement of some parameters of the materials, such as thermal diffusivity, thermal conductivity, and thermal expansion coefficient, is very important for applications used especially in the manufacturing of devices. The thermal diffusivity given in Section 3.1, α (m^2s^{-1}), is an important thermophysical parameter that measures how effectively the phonons carry heat from the sample. However, the measurement of heat exchange or thermal impedance for a given material's heat exchange is essentially determined by the thermal effusivity, e ($Ws^{1/2}\,m^{-2}\,K^{-1}$). The e is another important thermophysical parameter for quenching operations as much as for surface heating or cooling processes. These quantities are defined by $\alpha = \lambda/\rho c$ and $e = \sqrt{\lambda \rho c}$, where λ is the thermal conductivity, c is the specific heat capacity, and ρ is the bulk density. The known thermal conductivity of α and e can be obtained from $\lambda = e\sqrt{\alpha}$ [7]. The variation of these parameters with respect to filler content will be given in Section 3.1 in more detail.

Considering the theoretical background of thermal conductivity, some predictive models of thermal conductivity emerge. The Maxwell Theoretical Model is the main focal point for most of these models. This model uses potential theory to obtain a precise solution for the conductivity of a system with spherical, noninteracting particles in a continuous matrix state [3–5, 8–10].

$$\lambda_c = \lambda_m \left[\frac{\lambda_f + 2\lambda_m + 2\Phi_f \left(\lambda_f - \lambda_m\right)}{\lambda_f + 2\lambda_m - \Phi_f \left(\lambda_f - \lambda_m\right)} \right], \tag{1}$$

where λ_c, λ_m, and λ_f are the thermal conductivities of the composite, matrix, and filler respectively, and Φ_f is the volume fraction of filler. The Hashin-Shtrikman model is described as one of the best ways to estimate the lower limit when no information is available about the particle distribution in the matrix [6]. This lower limit can be expressed by the following equation:

$$\lambda_c = \lambda_m + \frac{\Phi_f}{1/\left(\lambda_f - \lambda_m\right) + \left(1 - \Phi_f\right)/3\lambda_m}, \tag{2}$$

where λ_c, λ_m, and λ_f are the thermal conductivities of the composite, matrix, and filler, respectively, and Φ_f is the volume fraction of filler.

Budiansky has provided a consistent way called "self-consistent" to calculate λ_c for composites. This model can be related to the calculation of a similar electrostatic problem. The model allows us to determine the thermal conductivities of the N-component system, which knows only the thermal conductivities of pure materials (λ_i) and volume parts (Φ_i) with respect to (4) [11]:

$$\sum_{i=1}^{N} \Phi_i \left[\frac{2}{3} + \frac{1}{3} \left(\frac{\lambda_i}{\lambda_c} \right) \right]^{-1} = 1. \tag{3}$$

For a seconder system consisting of matrix and filler, (2) can be rewritten to the form given by (3)–(6):

$$\lambda_c = \frac{-b + \sqrt{b^2 - 4ac}}{2a} \tag{4}$$

$$a = 2 \tag{5}$$

$$b = \lambda_{f-} 2\lambda_m - 3\left(\lambda_f - \lambda_m\right)\Phi_f \tag{6}$$

$$c = -\lambda_f \lambda_m. \tag{7}$$

The Lewis–Nielsen model is defined by (8) and (9) for various shapes of fillers, as shown as follows [3, 4, 8, 11–13]:

$$\lambda_c = \lambda_m \frac{1 + AB\Phi_f}{1 - B\psi\Phi_f}, \tag{8}$$

where

$$\begin{aligned} \psi &= 1 + \frac{(1 - \Phi\max)\,\Phi_f}{\Phi_{\max}^2} \\ B &= \frac{\lambda_f/\lambda_m - 1}{\lambda_f/\lambda_m + A}. \end{aligned} \tag{9}$$

A is a variable which depends on the shape of the particles and $\Phi_{\max}$ is the maximum insertion fraction. Various values A and $\Phi_{\max}$ have been reported in the literature in different forms and different packing geometries (e.g., hexagonal, face and body centered cubic, simple cubic, and random). It is difficult to select correct values for A and $\Phi_{\max}$ in order to calculate the thermal conductivities with respect to the filler content.

In the study of Krupa, the Lewis–Nielsen theoretical model reveals experimental data significantly. The above parameters obtained by adaptation of experimental data have the following values: $A = 5.5 \pm 0.7$ and $\Phi_{\max} = 0.6$ ($R^2 = 0.982$) [6]. According to the Tavman [14], A and $\Phi_{\max}$ are taken as 3 and 0.64, respectively. The Budiansky and the Maxwell model give the closest tendency with our experimental data for the lower concentrations. The comparison results will be given in Section 3.

2. Experimental Study

Dendrite-shape copper powder with 75 μm average particle size is used as conductive filler material. The copper powder is sieved into 15–25 μm, 25–32 μm, 32–45 μm, 45–53 μm, 53–63 μm, 63–75 μm, 75–90 μm, 90–106 μm, 106–120 μm, 120–150 μm, and 150–180 μm fractional size groups (See in Figure 2) in order to test the effect of particle size on thermal and electrical conductivity. The SEM image of dendritic-shaped copper particle is shown in Figure 1. As can be seen

Table 1: Properties of UPR given by the manufacturer.

Pure UPR properties					
Physical properties		Hardening characteristics		Mechanical properties	
Viscosity	600–700 cps	Gelling time	7 ± 2 min	Microhardness	18.62 HV
Monomer	Styrene (35%)	Peak temp.	150 ± 5°C	Elong. at break	20%
Acid number	28 ± 2 mg/KOH/g	Peak temp. dur. time	12 min	Tensile stress	45.26 MPa
Density	1.2 ± 0.01 g/cm^3	Tot. peak temp. reach time	20 min	Tensile modulus	1.177 GPa

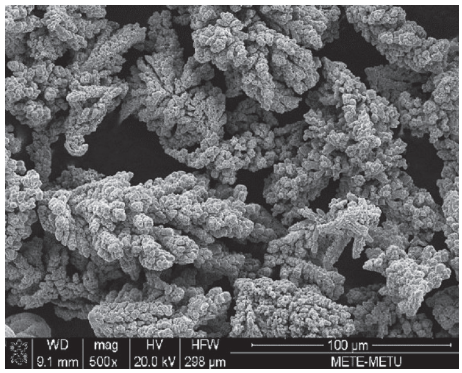

Figure 1: Dendrite-shape copper particle (×500).

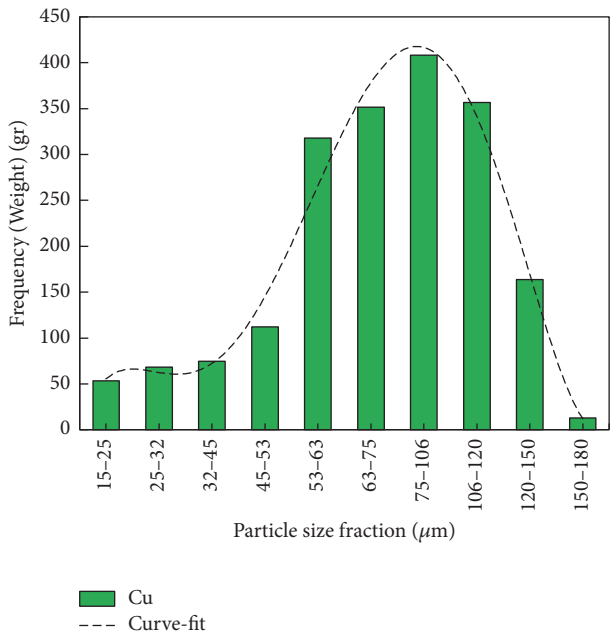

Figure 2: Copper powder particle size distribution.

in SEM image, the dendritic-shaped particle structure has much more contact surface area than the spherical and flake structures.

Unsaturated polyester (orthophthalic type UPR), including 35% ± 2 styrene as reactive diluent, with a brand name of CE 92-N8 was obtained from Cam Elyaf A.Ş. (Istanbul, Turkey). Methyl ethyl ketone peroxide used as initiator and cobalt naphthenate used as an accelerator were obtained from Akzo-Nobel (USA). In Table 1 pure UPR properties are given by the manufacturer.

Table 2: Component physical properties of composite (matrix and filler) materials.

Physical properties	UPR resin (CE 92-N8)	Copper filler
Average particle size (d, μm)	-	75
Density (ρ, g/cm^3)	1.20	8.92
Melting temperature (T_m, °C)	280	1084.62
Thermal conductivity (λ, Wm^{-1}K^{-1})	0.22	385

The total volume of UPR and the filler, 30 cm^3, is mixed after 1.5 g of the accelerator catalyst is added at the calculated ratios using a small mechanical mixer for about 15 minutes (at 40–60 rpm). Then, the mixture is stirred for 5 minutes after adding 5 g of hardener. The composite mixture in a viscous form is cast into a mold and left for 15 minutes for initial curing. In total, the hardened sample is obtained in about 35 minutes. The specimens are cured in a furnace for 4 hours at 150°C [12]. The cured specimens are machined to disc shape with 20 mm diameter and 8 mm thickness. The thermal conductivity is measured using a thermal conductivity analyzer (C-Therm TCi) by modified transient plane source technique in characterizing the thermal conductivity and effusivity of tested materials. The measurements are carried out at 24 ± 1°C with a 17 mm diameter flat probe. The thermal stability of the samples is measured by thermogravimetric analysis (TGA) using a HITACHI TG/DTA 6300 thermogravimetric analyzer. The TGA analysis was performed under flowing nitrogen. Mass loss was traced as samples were heated at a rate of 10°C min^{-1} from room temperature to 700°C. The morphology of the inner state of composites was examined by scanning electron microscopy. The physical properties of component of the composite materials are given in Table 2.

After the preparation of 15 mm in diameter and 2 mm in thickness disc shaped samples the electrical resistance was measured by the two-point contact (pin) method [13, 15] using a KEITHLEY-619 direct current electrometer which has the measuring range of 0.1–2.0E13 ohm.

3. Results and Discussion

This section consists of three subsections; thermal conductivity, mechanical properties, and electrical conductivity. The results of experimental work in each section are presented.

Table 3: Thermal conductivity, effusivity, and diffusivity change with filler content.

Φ_f %	P/C, λ [$Wm^{-1}K^{-1}$]	P/C effusivity [$Ws^{1/2}m^{-2}K^{-1}$]	P/C diffus. [m^2s^{-1}]
16	1.577	1759.90	$8.0E-07$
23	1.837	1904.51	$9.3E-07$
30	2.193	2096.59	$1.1E-06$
37	2.536	2275.42	$1.2E-06$
43	2.827	2422.27	$1.4E-06$
47	3.363	2682.83	$1.6E-06$
50	3.475	2735.61	$1.6E-06$
52	3.682	2831.80	$1.7E-06$
55	3.898	2930.33	$1.8E-06$
57	4.722	3290.23	$2.1E-06$

3.1. Thermal Conductivity. Thermal conductivity measurements of the polyester-copper (P/C) composites with various filler loadings are displayed and comparison of the theoretical models is given in this section. The Hashin-Strikman and the Lewis–Nielsen models give the closest tendency with the experimental data. The overall trend for all composites is that λ increases with higher filler content. These results were expected and were consistent with other studies [1, 3–11, 14]. Thermal conductivity and effusivity results are tabulated in Table 3. The conductivity and effusivity of composite materials increase with increasing copper filler content. The thermal conductivity probe measures the effusivity of a material (Figure 3), which is

$$\text{Effusivity}\,(E) = \sqrt{\lambda \rho c_p}, \tag{10}$$

$$\text{Diffusivity}\,(D) = \frac{\lambda}{\rho c_p} \tag{11}$$

$$D = \left(\frac{\lambda}{E}\right)^2, \tag{12}$$

where λ is the thermal conductivity (W/m K), ρ is the density (g/cm^3 or kg/m^3), and c_p is the heat capacity (J/kg K). Diffusivity can be derived (12).

The thermal effusivity defined (10) is an important thermophysical property, which characterizes the thermal impedance of matter [7, 16]. Figure 3 compares the effusivity and calculated diffusivity of composite mixtures with copper filler volumetric content. The effusivity values of P/C composites are increasing with volume filler fraction.

Comparing the measured values of λ for P/C composites, it can be observed that P/C system was more effective than proposed theoretical models (Figure 4) as in literature [3, 5, 17]. This result could be attributed to the more suitable packing of copper particulates. The fillers would be able to bridge gaps among them and create a more extensive three-dimensional thermal conductivity network throughout the UPR matrix. The P/C composites do not obey the given theoretical models at higher concentrations.

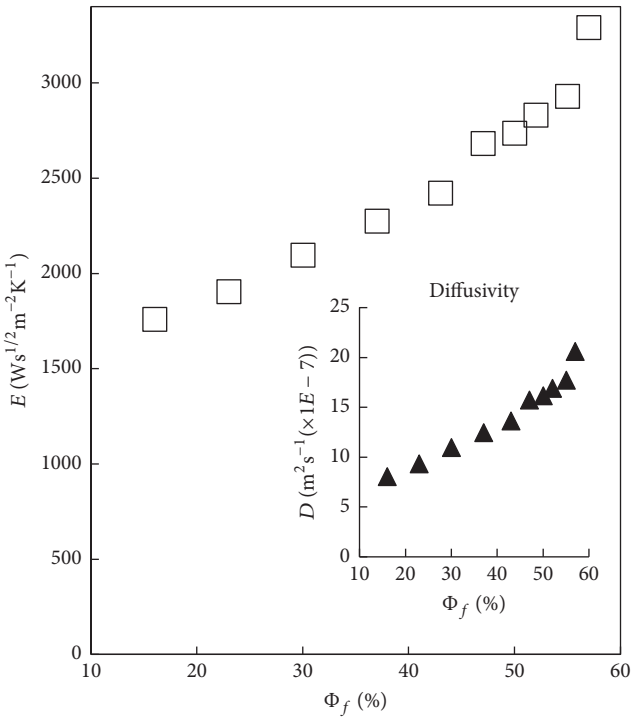

Figure 3: Measured effusivity and calculated diffusivity of P/C versus copper filler content.

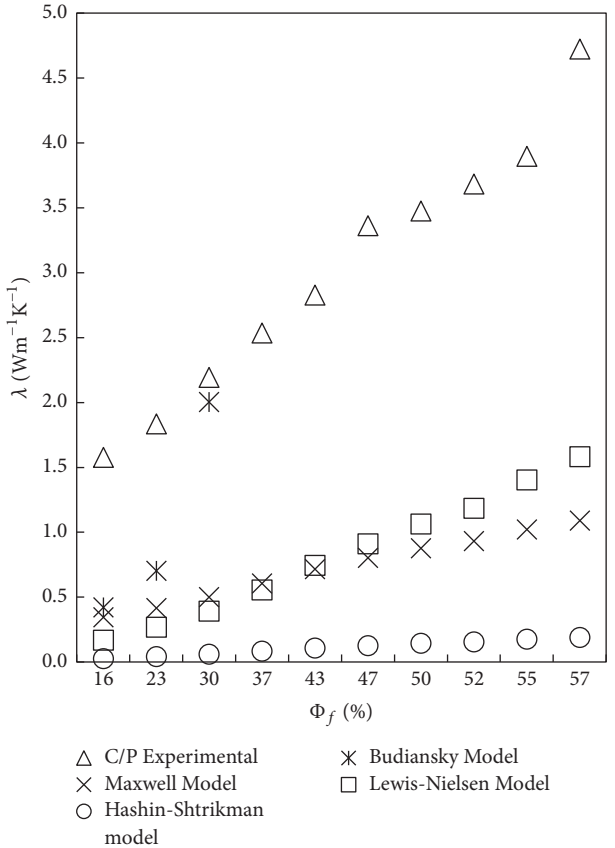

Figure 4: Variation of thermal conductivity of composite versus volume content of filler and comparison of the theoretical models.

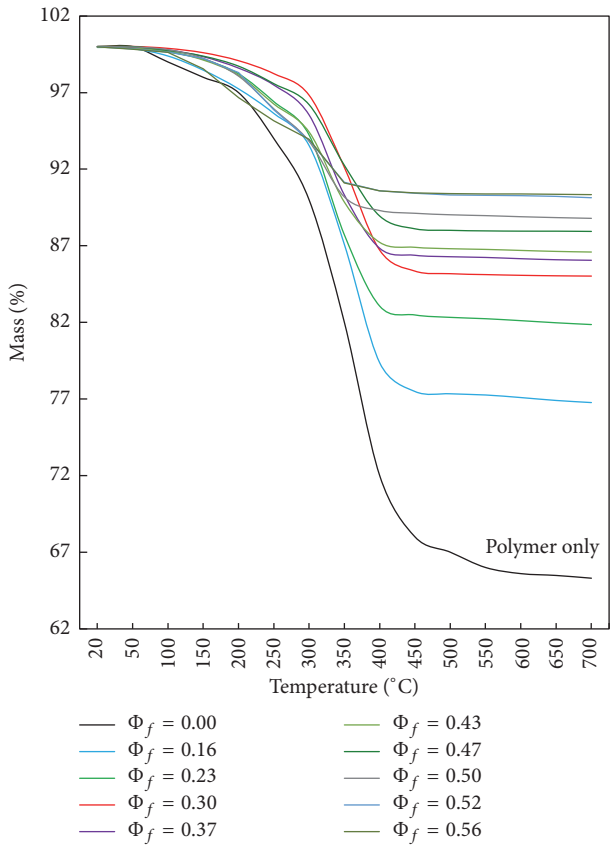

Figure 5: TGA curves of P/C powder composite specimens for different weight percentage of copper filler.

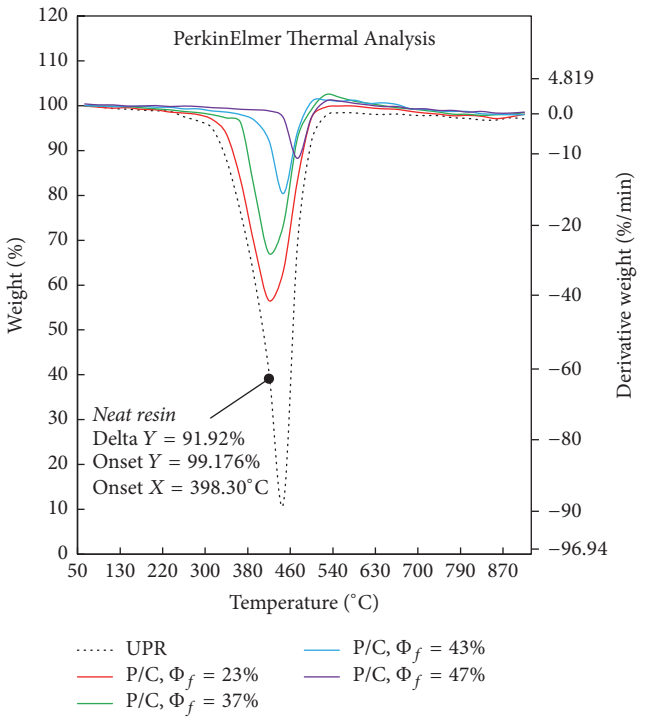

Figure 6: DTA curves of P/C composites as various amounts of Cu content.

However, Maxwell and Budiansky models give closer results below 37% filler content. As can be seen from the result, the addition of copper into the UPR matrix increased the thermal conductivity over 21 times that of neat UPR. The composite mixture saturates at a volumetric concentration of about 55–60% when copper is added. The TGA curves of P/C composites are given in Figure 5. There is a significant increase in the thermal stability of the UPR with increasing Cu% content. This can be explained by the higher heat capacity and thermal conductivity of the copper, which causes heat absorption. This causes the UPR chains to start to decompose at higher temperatures [18, 19].

In the TGA curve of UPR, initial weight loss occurs at a temperature of 250°C approximately. In almost all samples, the complete degradation of the polymer (weight loss) is completed about 420°C. The major degradation temperature of UPR was found to be improved from 230 to 400°C incorporating the P/C. The P/C composites have shown better thermal stability compared to neat resin. The dynamic DTA curves of the decomposition of UPR and composites with different copper filler concentrations are plotted in Figure 6. The maximum weight loss occurs at the temperature interval of 400–440°C. This analysis reveals that the thermal stability of composites increases with increasing of the copper content [20].

The perfection of the crystalline domains of pure UPR is degraded by the interaction between the pure UPR and the Cu filler, and the filler particles could cause a more pronounced effect on crystallinity as the filler concentration is increased [19, 21].

In the experiments of filler particle size effect, the average copper filler (25–32 μm, 32–45 μm, 45–53 μm, 53–63 μm, 63–75 μm, 75–90 μm, 90–106 μm, 106–120 μm, and 120–150 μm) fractional particle size specimen groups having 43% Φ_f (median value) are tested. Thermal conductivity-particle size relationship is given in Figure 7.

The thermal conductivity increases slightly with particle size. In other words, larger filler particles should result in a lower thermal barrier (thermal resistivity). Figure 7 shows the thermal conductivity of copper filled UPR composites for different particle size distributions. In the study of Biswas et al., the same results were achieved for Cu/UPR composite system. They reported that the addition of Cu filler to the UPR increased the thermal and electrical conductivity. According to this result, the electrical conductivity obeys the same trends as thermal conductivity [21].

3.2. Mechanical Properties. The addition of Cu into the polyester matrix material has a significant effect on the mechanical characters of the composite due to its dendritic shape and excellent mechanical strength. The stress-strain curves representing the neat UPR and its composites in various filler loadings are shown in Figure 8. The mechanical properties of the compound mixture have been found to be significantly increased compared to pure UPR [14, 17, 19–21]. The slope of the curves increases with increasing Cu content. Based on the slope of the elastic zone, the tensile modulus

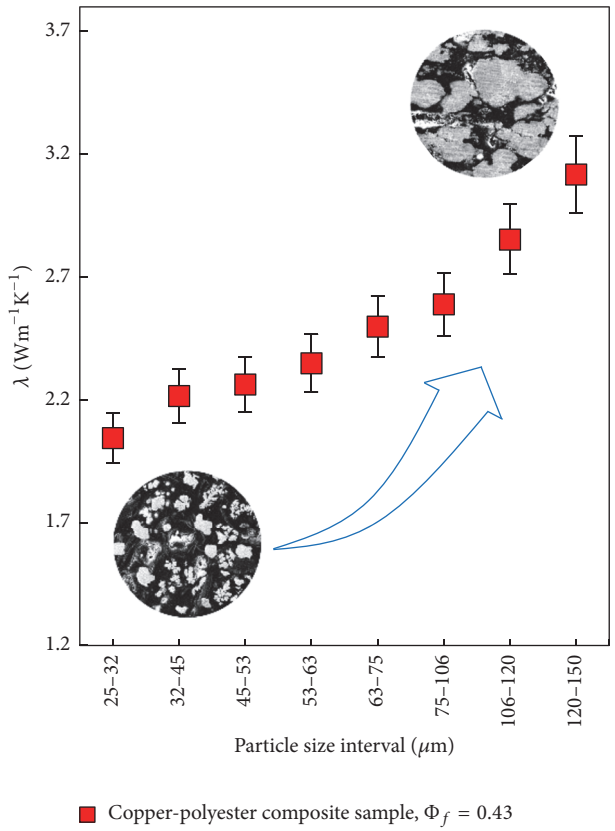

Figure 7: The copper filler particle size effect on thermal conductivity.

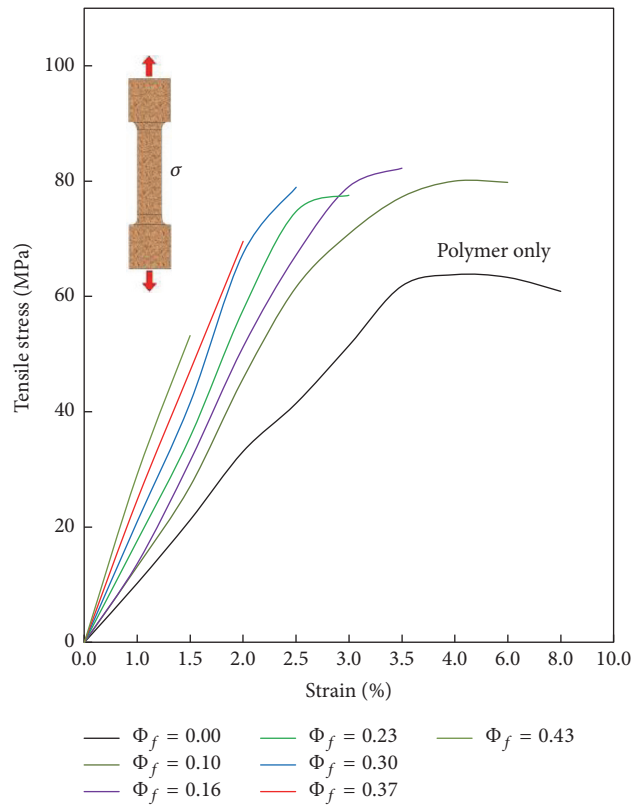

Figure 8: Stress-strain curves of the composites with various Cu loadings.

values are calculated and their variations through Φ_f% are shown in Figure 9.

Tensile properties were tested according to ASTM Standard D-638 (Standard Test Method for Tensile Properties of Plastics). The tests were carried out at a temperature of 23°C and 2 [mm/min] tensile speed using a microcontrolled universal testing machine (model WDW 50 E). The tensile strength and percentage of elongation of P/C composites are shown in Figure 9.

The elongation at break value for neat UPR given by the manufacturer is at about 20%. The neat resin samples prepared in this study are baked at 150°C for 4 hours. The postcure resultant internal structure becomes more brittle and elongation at break falls to 8–12%.

The average tensile strength for pure UPR resin is 45.26 [MPa]. The tensile strength values were found to increase with increasing Cu loading up to 16%. After this value, the copper content tends to decrease gradually as the copper content increases.

The P/C composite structure has reached the highest tensile stress value with a volume load of 16% Cu. The maximum tensile strength value is 82.23 [MPa], which corresponds to an improvement of about 129% (maximum tensile stress, 63.78 [MPa]) when compared to neat resin. This increased tensile property can be attributed to the good dispersion of the filler in the polymer matrix. The maximum elongation was approximately 0.8 mm (8%) at break for neat UPR.

On the other hand, a gradual decrease in the elongation at break of the composites was observed with increasing Cu content. The fracture elongation for Φ_f = 43% Cu loading decreased from 79.88% to 20.83% for pure polymer. The metal particles dispersed in the matrix restrict the movement of the polymer chains, which tend to move due to temperature changes or mechanical forces. Similar evaluations can be found in the literature [2, 14, 17, 22].

Hardness is another indication of the ability of a material to resist deformation [22]. Addition of Cu fillers increased significantly the hardness of neat UPR as shown in Figure 10.

The bar chart shows experimental microhardness (HV) of composites as a function of Cu. As Cu content increases, microhardness of composites increases with respect to pure UPR matrix. Namely, the filler material incorporated into the UPR increases the microhardness of the resin around 18 HV by about ten times (180 HV).

In literature, the studies of Goyal et al. [22], Pargi et al. [23], and Teh et al. [24] reported the same result that the hardness and strength of composite mixture increase with increasing copper filler.

3.3. Electrical Conductivity. The easiest way to produce conductive polymer composites is to fill an insulating polymer having good mechanical properties with highly conductive particles, that is, metal powders. Electrical conductivity of metal filled polymers has evidenced the known classical

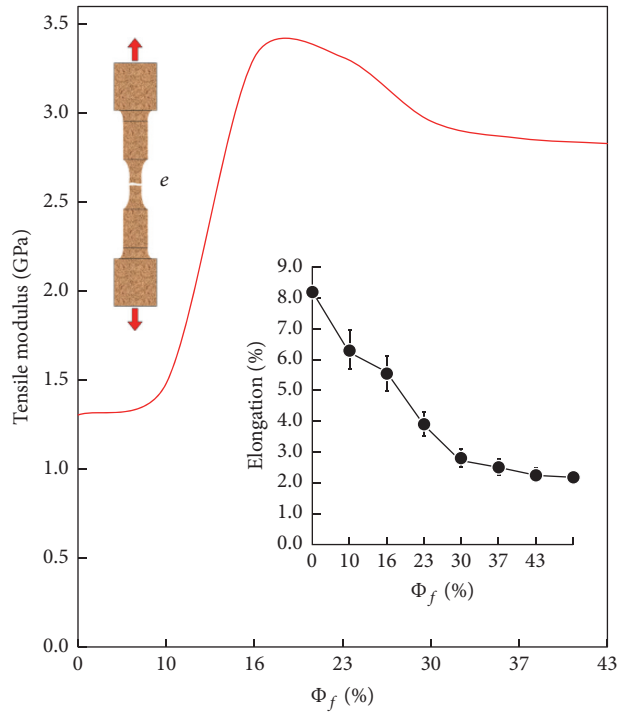

FIGURE 9: Tensile modulus and elongation for Φ_f % curves of the composites mixture.

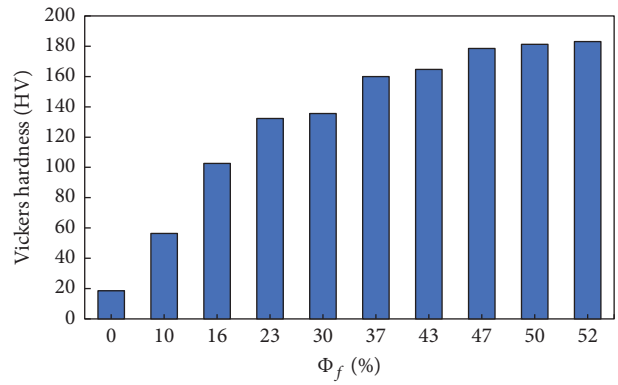

FIGURE 10: Hardness as a function of vol.% of Cu in UPR matrix.

Insulating to Conducting Transition (ICT). The behavior of this property depends strongly on the filler concentration. It increases when the concentration of metal increases and the transition occurs at a fixed fraction called threshold of percolation. In percolation theory, the relationship between the electrical conductivity of the mixture and the volume fraction of the conductive filler is given by (1) [25]:

$$\sigma = \sigma_f \left(\Phi_f - \Phi_c\right)^t. \tag{13}$$

Conductivity of the composite mixture depends primarily on the concentration of conducting elements. In expression (10) Φ_c is the critical volumetric content (percolation threshold) meaning a minimal volume fraction of conducting filler at which a continuous conducting network of macroscopic length appears in the system, so the equation is applied only above the percolation threshold, Φ_f is the volume portion of the filler, σ_f is the conductivity of the conducting component or conductivity of conducting phase, and t is a parameter determining the power of the conductivity increase above Φ_c [25]. Roldughin and Vysotskii [26] obtained higher σ for mixture of nickel powder (8 μm average filler size) with ED-20 epoxy resin hardened at 100°C temperature. They reported that σ increases with increasing nickel content Φ_f and particle radius. Furthermore, it is claimed that lower viscosity of matrix material has a positive effect on the formation of conductive chains during curing.

In El-Tantawy et al.'s work [27], the relationship between the electrical conductivity and carbon black content under precure and postcure conditions was investigated. In experiments, epoxy resin and 20 μm average size filler powder were mixed at different ratios and cured for 3 hours and 1 week at 80°C. They found that conductivity increased with volumetric filler rate of graphite. The dielectric properties of the low-density polyethylene- (LDPE-) matrix composites with the different conducting fillers (carbon fiber (CF), copper (Cu), and nickel (Ni) powders) were studied by Dang et al. [28] over a broad range of frequency and volume fraction of fillers. The electrical conductivity increases with an increase in frequency and the amount of fillers. Wu et al. showed the filler size effect on percolation threshold of isotopically conductive adhesive (ICA). Ag particles with 50 nm average diameter were used as filler. The results show that the percolation threshold of ICAs depends strongly on the filler sizes, which reaches 63% wt. Results obtained by theoretical calculation are in good agreement with the experimental results [29].

In our study, logarithmic σ of the copper filled electrodes increases with increasing copper concentration Φ_f. In the P/C composite mixture, the conductivity chain is established at about 20% copper Φ_f value which is percolation threshold of C/P composite system. As can be also seen from Figure 11, the solution reaches saturation at about 55% volume fraction.

In the experiments of filler particle size effect, the average filler fractional particle size specimen groups having 46% Φ_f are tested. It is observed that the electrical conductivity increases with increasing particle size exponentially [12]. In other words, larger filler particles should result in a lower composite resistivity. Figure 12 shows the conductivity of C/P composites for different particle size distributions.

The scanning electron micrograph (SEM) photographs of 86% wt copper-polyester composite with ×1000 magnification are given in Figures 13(a)-13(b). The microphotographs of composites are also shown in Figures 13(d)–13(f) as 60% wt, 70% wt, and 90% wt-Cu, respectively.

In the SEM images, the formation of agglomerates of the copper filler in the resin can be observed. As can be seen from Figure 13, the addition of higher volumetric rate of filler material brings the particles closer to one another and even provides contact. The samples obtained by mixing copper filler with UPR give very high electrical conductivity values compared to the matrix material alone. Because of this

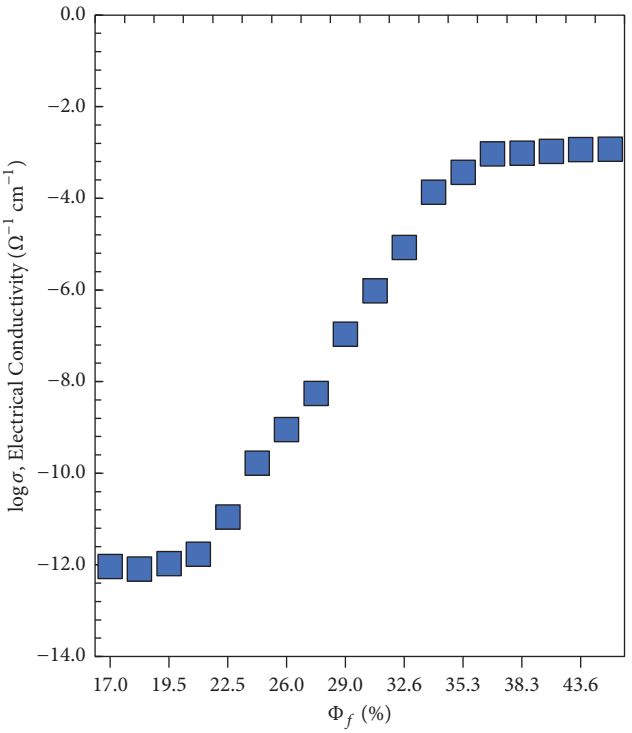

FIGURE 11: Variation of electrical conductivity of composite specimens versus filler rate.

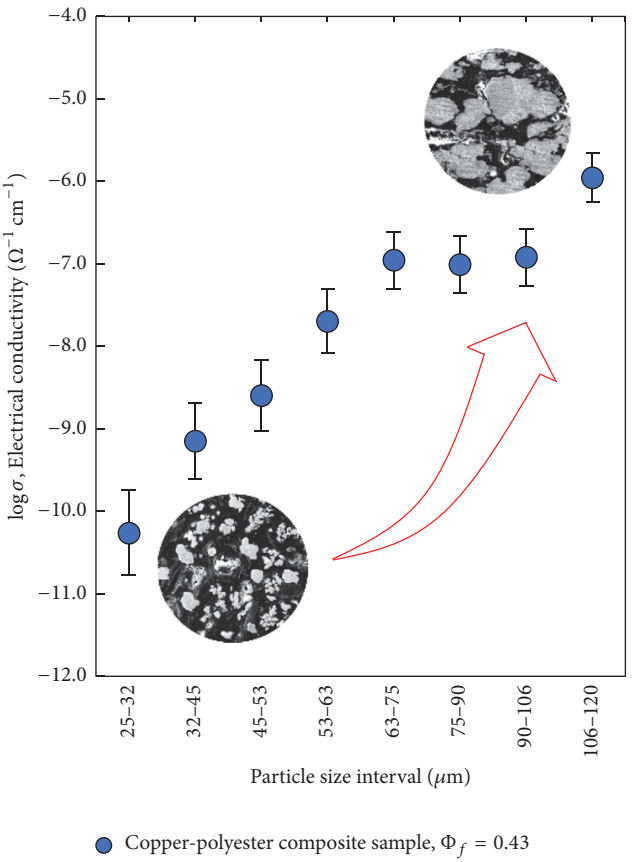

FIGURE 12: The copper filler particle size effect on electrical conductivity.

high level of electrical conductivity, Yaman and Çoğun used this composite material as electrodes for machining SAE1040 steel material by a die-sinker electrical discharge machine successfully.

Figure 14 shows the machined metallic material and used electrode images. They compared the electrical conductivity of their novel electrode with respect to the copper filler content. They found out that the electrical conductivity of composite electrodes increases with increasing the copper filler content [12].

As a consequence, studies in the literature show that both thermal and electrical conductivity increase with increasing filler content and size [1–13, 15–31]. It is also understood that the filling material particle shape is another important factor [30, 31]. Similar to the results obtained by Wang et al., this study suggests that dendrite shaped particles are a significant contributor to the thermal and electrical conductivity of the composite structure. At any filler concentration, particles with large dimensions (aspect ratio) may form better conductive paths towards heat and electrical flow. This causes significant increases in the thermal and electrical conductivity of the composite structure.

4. Conclusions

This paper presents theoretical and experimental investigation on thermal and electrical conductivity in a polymeric composite composed of UPR matrix with dendrite shaped copper particles as fillers. The thermal conductivity was found to increase along with filler content. P/C was found to be more effective in promoting both the thermal and electrical conductivity of the material when compared to theoretical systems. Thermogravimetric analysis (TGA) and differential thermogravimetric analysis (DTA) also showed an increment in thermal stability after the addition of filler in UPR. The maximum thermal conductivity value of composite sample is obtained as 4.72 [Wm^{-1} K^{-1}] experimentally so the addition of copper into the matrix increased the thermal conductivity over 21 times that of neat UPR. The Hashin-Strikman and the Lewis–Nielsen models give the similar tendency with the experimental data. However, particularly for lower (below 37% volumetric) filler content, Maxwell and Budiansky models exhibit convergence to the experimental results.

The next portion of the study focused on the effect of particle size of filler on conductivity. The results show that the larger particle size causes relatively higher thermal conductivity. The electrical conductivity results obey the same trends as thermal conductivity. The electrical conductivity increases with increasing filler content exponentially. It is also observed that the electrical conductivity increases with increasing particle size.

Conflicts of Interest

The authors declare that there are no conflicts of interest regarding the publication of this paper.

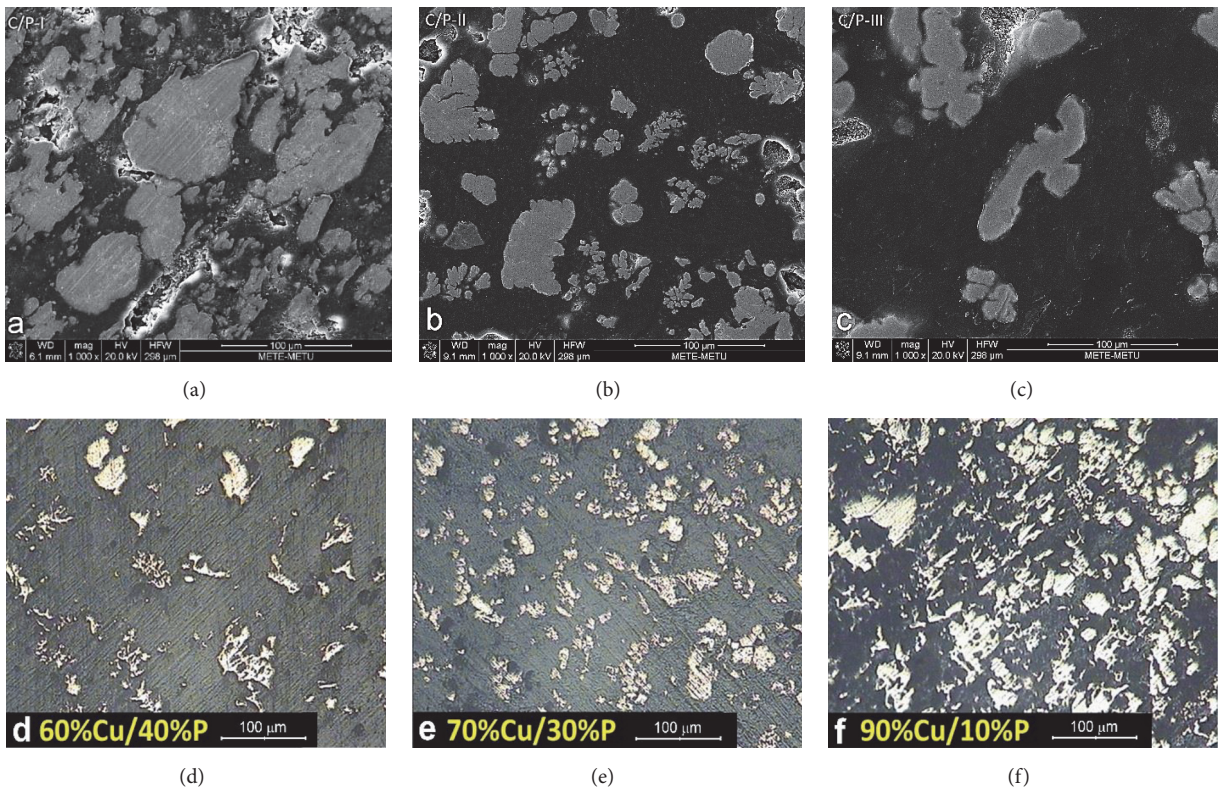

Figure 13: SEM (×1000)/Micro (×100) images of (a) Cu 86% wt, (b) Cu 75% wt, (c) Cu 60% wt, (d) Cu 60% wt, (e) Cu 70% wt, and (f) Cu 90% wt-polyester composite mixture.

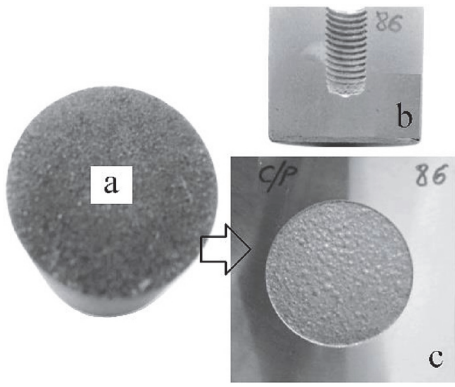

Figure 14: Electrode and machined workpiece produced from a P/C composite material with a copper content of 86% wt: (a) machine surface of electrode, (b) electrode cross section, and (c) machined SAE 1040 steel material.

Acknowledgments

The authors wish to thank the TÜBİTAK SAGE for their motivations and valuable supports.

References

[1] W. C. Choi, K. H. Yoon, and S. S. Jeong, "Morphology and thermal conductivity of polyacrylate composites containing aluminum/multi-walled carbon nanotubes," *Composites Part A*, vol. 45, pp. 1–5, 2013.

[2] M. H. Al-Saleh, G. A. Gelves, and U. Sundararaj, "Copper nanowire/polystyrene nanocomposites: lower percolation threshold and higher EMI shielding," *Composites Part A*, vol. 42, no. 1, pp. 92–97, 2011.

[3] D. C. Moreira, L. A. Sphaier, J. M. L. Reis, and L. C. S. Nunes, "Experimental investigation of heat conduction in polyester-Al2O3 and polyester-CuO nanocomposites," *Experimental Thermal and Fluid Science*, vol. 35, no. 7, pp. 1458–1462, 2011.

[4] A. Agrawal and A. Satapathy, "Development of a heat conduction model and investigation on thermal conductivity enhancement of AlN/Epoxy composites," *Procedia Engineering*, vol. 51, pp. 573–578, 2013.

[5] W. Zhou, J. Zuo, and W. Ren, "Thermal conductivity and dielectric properties of Al/PVDF composites," *Composites Part A: Applied Science and Manufacturing*, vol. 43, no. 4, pp. 658–664, 2012.

[6] I. Krupa, V. Cecen, A. Boudenne, J. Prokes, and I. Novak, "The mechanical and adhesive properties of electrically and thermally conductive polymeric composites based on high density polyethylene filled with nickel powder," *Materials and Corrosion*, vol. 51, pp. 620–628, 2013.

[7] T. A. El-Brolossy and S. S. Ibrahim, "Photoacoustic measurement of thermal properties of polystyrene metal oxide composites," *Thermochimica Acta*, vol. 509, no. 1-2, pp. 46–49, 2010.

[8] M. Shen, Y. Cui, J. He, and Y. Zhang, "Thermal conductivity model of filled polymer composites," *International Journal of Minerals, Metallurgy and Materials*, vol. 18, no. 5, pp. 623–631, 2011.

[9] L. Kowalski, J. Duszczyk, and L. Katgerman, "Thermal conductivity of metal powder-polymer feedstock for powder injection moulding," *Journal of Materials Science*, vol. 34, no. 1, pp. 1–5, 1999.

[10] F. Danes, B. Garnier, and T. Dupuis, "Predicting, Measuring, and Tailoring the Transverse Thermal Conductivity of Composites from Polymer Matrix and Metal Filler," *International Journal of Thermophysics*, vol. 24, no. 3, pp. 771–784, 2003.

[11] B. Budiansky, "Thermal and Thermoelastic Properties of Isotropic Composites," *Journal of Composite Materials*, vol. 4, no. 3, pp. 286–295, 1970.

[12] K. Yaman and C. Çogun, "An experimental work on using conductive powder-filled polymer composite cast material as tool electrode in EDM," *The International Journal of Advanced Manufacturing Technology*, vol. 73, no. 1-4, pp. 535–543, 2014.

[13] W. Guoquan, "Electrical resistance measurement of conductive network in short carbon fibre-polymer composites," *Polymer Testing*, vol. 16, no. 3, pp. 277–286, 1997.

[14] I. H. Tavman, "Thermal and mechanical properties of copper powder filled poly(ethylene) composites," *Powder Technology*, vol. 91, no. 1, pp. 63–67, 1997.

[15] A. R. Blythe, "Electrical resistivity measurements of polymer materials," *Polymer Testing*, vol. 4, no. 2-4, pp. 195–209, 1984.

[16] A. Boudenne, L. Ibos, M. Fois, J. C. Majeste, and E. Gehin, "Electrical and thermal behavior of polypropylene filled with copper particles," *Composites Part A: Applied Science and Manufacturing*, vol. 36, no. 11, pp. 1545–1554, 2005.

[17] A. S. Luyt, J. A. Molefi, and H. Krump, "Thermal, mechanical and electrical properties of copper powder filled low-density and linear low-density polyethylene composites," *Polymer Degradation and Stability*, vol. 91, no. 7, pp. 1629–1636, 2006.

[18] V. Cecen, Y. Seki, M. Sarikanat, and I. H. Tavman, "FTIR and SEM analysis of polyester- and epoxy-based composites manufactured by VARTM process," *Journal of Applied Polymer Science*, vol. 108, no. 4, pp. 2163–2170, 2008.

[19] C. Bora, P. Bharali, S. Baglari, S. K. Dolui, and B. K. Konwar, "Strong and conductive reduced graphene oxide/polyester resin composite films with improved mechanical strength, thermal stability and its antibacterial activity," *Composites Science and Technology*, vol. 87, pp. 1–7, 2013.

[20] A. Ansari and M. J. Akhtar, "Investigation on electromagnetic characteristics, microwave absorption, thermal and mechanical properties of ferromagnetic cobalt-polystyrene composites in the X-band (8.4-12.4 GHz)," *RSC Advances*, vol. 6, no. 17, pp. 13846–13857, 2016.

[21] B. Biswas, S. Chabri, B. C. Mitra, K. Das, N. R. Bandyopadhyay, and A. Sinha, "Effect of Copper/Graphite Addition on Electrical Conductivity and Thermal Insulation of Unsaturated Polyester/Jute Composites," *Journal of The Institution of Engineers (India): Series D*, vol. 98, no. 1, pp. 19–25, 2017.

[22] R. K. Goyal, K. R. Kambale, S. S. Nene, B. S. Selukar, S. Arbuj, and U. P. Mulik, "Fabrication, thermal and electrical properties of polyphenylene sulphide/copper composites," *Materials Chemistry and Physics*, vol. 128, no. 1-2, pp. 114–120, 2011.

[23] M. N. F. Pargi, T. P. Leng, S. Husseinsyah, and C. K. Yeoh, "The Effect of Coarse Particle Size on the Properties of Recycled Copper-Filled Epoxy Composites," *Polymer—Plastics Technology and Engineering*, vol. 54, no. 3, pp. 265–269, 2015.

[24] P. L. Teh, H. T. Ng, and C. K. Yeoh, "Recycled copper as the conductive filler in polyester composites," *Malaysian Polymer Journal*, vol. 6, pp. 98–108, 2011.

[25] Y. P. Mamunya, V. V. Davydenko, P. Pissis, and E. V. Lebedev, "Electrical and thermal conductivity of polymers filled with metal powders," *European Polymer Journal*, vol. 38, no. 9, pp. 1887–1897, 2002.

[26] V. I. Roldughin and V. V. Vysotskii, "Percolation properties of metal-filled polymer films, structure and mechanisms of conductivity," *Progress in Organic Coatings*, vol. 39, no. 2-4, pp. 81–100, 2000.

[27] F. El-Tantawy, K. Kamada, and H. Ohnabe, "Electrical properties and stability of epoxy reinforced carbon black composites," *Materials Letters*, vol. 57, no. 1, pp. 242–251, 2002.

[28] Z. M. Dang, Y. H. Zhang, and S. C. Tjong, "Dependence of dielectric behavior on the physical property of fillers in the polymer-matrix composites," *Synthetic Metals*, vol. 146, no. 1, pp. 79–84, 2004.

[29] H. P. Wu, X. J. Wu, M. Y. Ge, G. Q. Zhang, Y. W. Wang, and J. Z. Jiang, "Effect analysis of filler sizes on percolation threshold of isotropical conductive adhesives," *Composites Science and Technology*, vol. 67, no. 6, pp. 1116–1120, 2007.

[30] H. Chen, V. V. Ginzburg, J. Yang et al., "Thermal conductivity of polymer-based composites: Fundamentals and applications," *Progress in Polymer Science*, vol. 59, pp. 41–85, 2016.

[31] X. Wang, L. Zhang, and L. Pei, "Thermal conductivity augmentation of composite polymer materials with artificially controlled filler shapes," *Journal of Applied Polymer Science*, vol. 131, no. 8, 2014.

Hindawi
International Journal of Polymer Science
Volume 2018, Article ID 1416531, 9 pages
https://doi.org/10.1155/2018/1416531

Research Article

Polyaniline/Polystyrene Blends: In-Depth Analysis of the Effect of Sulfonic Acid Dopant Concentration on AC Conductivity Using Broadband Dielectric Spectroscopy

Noora Al-Thani, Mohammad K. Hassan, and Jolly Bhadra

Center for Advanced Materials, Qatar University, P.O. Box 2713, Doha, Qatar

Correspondence should be addressed to Mohammad K. Hassan; mohamed.hassan@qu.edu.qa

Received 2 January 2018; Accepted 25 February 2018; Published 4 April 2018

Academic Editor: Renbo Wei

This work presents an in-depth analysis of the alternating current (AC) conductivity of polyaniline-polystyrene (PANI-PS) blends doped with camphor sulfonic acid (CSA) and prepared using an in situ dispersion polymerization technique. We prepared the blends using fixed ratios of PS to PANI while varying the concentration of the CSA dopant. The AC conductivity of the blends was investigated using broadband dielectric spectroscopy. Increasing CSA resulted in a decrease in the AC conductivity of the blends. This behaviour was explained in terms of the availability of a lone pair of electrons of the NH groups in the polyaniline, which are typically attacked by the electron-withdrawing sulfonic acid groups of CSA. The conductivity is discussed in terms of changes in the dielectric permittivity storage (ε'), loss (ε''), and modulus (M'') of the blends over a wide range of temperatures. This is linked to the glass transition temperature of the PANI. Dielectric spectra at low frequencies indicated the presence of pronounced Maxwell-Wagner-Sillars (MWS) interfacial polarization, especially in samples with a low concentration of CSA. Electrical conduction activation energies for the blends were also calculated using the temperature dependence of the direct current (DC) conductivity at a low frequency (σ_{dc}), which exhibit an Arrhenius behaviour with respect to temperature. Scanning electron microscopy revealed a fibrous morphology for the pure PANI, while the blends showed agglomeration with increasing CSA concentrations.

1. Introduction

In the last few decades, intensive research has focused on intrinsic electrically conductive polymers (ICP) because of their possible applications in light-emitting diodes, batteries, electromagnetic shielding, antistatic coating, and gas sensors [1–5]. Lack of processability in the doped state hinders the ability of ICPs to be blended with industrial polymers. Because of a synergic combination of mechanical properties of conventional insulating polymers with electrical properties of the conducting polymers, blending is of great technological importance. In terms of the percolation threshold of the conductive materials in any blend, polymeric materials have better properties than the inorganic conductive phase like carbon black or metal particles.

In the conducting polymers family, polyaniline (PANI) has excellent tunable electrical conductivity desired for electrical and electronic industries. Upon protonation by Lewis acid, these polymers can be switched to a wide conductivity range [6]. Since the last two decades, a lot of researches have been carried out to improve the PANI processability by maintaining the electrical properties. Different methods of composite preparation, such as blending, doping with acids, and copolymerization, have been adopted to obtain processable PANI, and these efforts have resulted in many research publications [7–10]. PANI in a modified, processable form has wide applications in the electrical and electronics industries [11, 12].

Various methods currently exist to make PANI processable. These include doping with organic acids, such as dodecyl benzene sulfonic acid (DBSA) [13] or camphor sulfonic acid (CSA) [14]. These sulfonated acids have long tails that enable the PANI to dissolve in nonpolar or weakly polar common organic solvents, which can cosolubilize most commercial polymers. This method has been utilized to prepare a number of PANI blends in which both PANI

complexes and preferred polymers are soluble in the same solvent. PANI has poor mechanical properties and it is generally procured in powder form. Of various processes used, blending of PANI with other polymers (thermoplastic or thermosetting) is one of the most commonly used techniques to enhance its mechanical strength. Using this method, the synergic combination of improved electrical properties from PANI and enhanced mechanical properties from conventional polymers can be amalgamated to produce a material with more potential applications in the electronics industry [15]. Blending of PANI with different types of conventional polymers, such as polyacrylonitrile [16], polyvinyl alcohol (PVA), and polystyrene (PS) [17, 18], have been investigated. PS has some useful features, such as good thermal stability, a degradation temperature above 400°C, good chemical resistance, and significant mechanical toughness.

Dielectric spectroscopy, also known as impedance spectroscopy (IS), is a powerful tool to study the effects of interactions between electromagnetic radiation and the chemical or physical properties of the materials [19, 20]. All matter consists of molecules and atoms with electric charges that respond whenever an electric field is applied to them. These responses are in the form of translational or rotational motion and they give rise to macroscopic electrical or dielectric behaviours in the material. Information regarding dielectric behaviours is useful for a variety of fields, such as electrical engineering, physical chemistry, electronic physics, and material science. Thus, using impedance spectroscopy, we can efficiently study polymer chain motion and different dispersion modes of fillers inside a polymer blend, which are related to the chemical composition, molecular structure, and phase morphology.

In order to investigate the electrical transport properties of any complex system, impedance spectroscopy (IS) is one of the most convenient tools used in solid state electronic system [21, 22]. In our previous works, we studied effect of sulfonic acid dopants on the CSA-doped PANI-PS blends for the gas sensor application [6]. This study concluded that the gas sensitivity and reversibility of the blends have a strong correlation with their conductivity. However, not many details on the electrical transport properties were done in our previous work. Therefore, herein and as a continuation to our prior study, we use broadband dielectric spectroscopy to present a detailed, in-depth investigation of the electrical transport behaviour of CSA-doped into PANI-PS blends and how this correlates with CSA concentrations.

2. Experimental

2.1. Experimental Section. The polymers and chemicals used for experiments were acquired from Merck and Sigma chemical companies and these were of very high purity (99.9%). Further purification of aniline was performed by repeated distillation in a vacuum following preservation at a low temperature prior to use. The oxidant (ammonium persulphate), toluene, and acid (CSA) were used as obtained. During the synthesis, all solutions were prepared using double-distilled water.

PANI was obtained using dispersion polymerization with conventional techniques described previously [23, 24]. A solution of aniline and CSA in aqueous medium was prepared by stirring them for 1 hour. Following a polymerization step, ammonium persulphate was added dropwise with constant stirring. The whole system was maintained at a temperature of 0–5°C. Upon completion of the oxidant addition process, the reaction was constantly stirred for an additional 24 hours. The reaction turned into a bluish-green homogeneous mixture, indicating the completion of the polymerization reaction. The resulting precipitate was then filtered and washed with deionized water and methanol until the filtrate became colourless to remove any oligomer or unreacted oxidant. PANI powder was then dried under reduced pressure at 40°C for 24 hours. The PANI-PS blend was prepared by following the above process except for replacing water and using predissolved PS in toluene by stirring for 1 hour instead. Four different concentrations of dopants (0.2 M, 0.3 M, 0.4 M, and 0.5 M) were used for the blend preparation. Finally, the blend solution was used to cast films on glass slides and interdigitate finger electrode thick film (gold, 15 mm × 15 mm) on an alumina substrate (250 μm online/spaces).

2.2. Characterization Techniques. Dielectric measurements were performed using a Novocontrol GmbH Concept 40 broadband dielectric spectrometer, and the data were collected over the frequency range 0.1 Hz–3 MHz at fixed temperatures in the range of −70 to 180°C. Samples were prepared and dried directly on 40 mm diameter stainless steel electrodes, and another 20 mm diameter stainless steel electrode was used as a top electrode during testing. The AC conductivity was calculated with the Novocontrol Win DETA software by using the measured values of dielectric permittivity and the dielectric loss factor.

The morphologies of the synthesized CSA-doped into PANI-PS blends were observed with scanning electron microscopy (SEM) using a nano-SEM Nova 450. In order to detect the glass transition temperatures of the composites, differential scanning calorimetry (DSC) tests were performed using a Perkin Elmer DSC 8500.

3. Results and Discussion

3.1. Dielectric Spectroscopy Measurements. Broadband dielectric spectroscopy is a powerful tool to interrogate polymeric material characteristics because both the conductivity and chain motion can be monitored in the same spectra. However, in the case of samples containing conducting polymers, such as PANI, the dielectric loss (ε'') and storage (ε') spectra are dominated by electrode polarization and conductivity effects [25–28]. In this case, conductivity overwhelms the relaxation peaks related to the glass transition and other secondary motions, which makes their analysis difficult. The conductivity engulfing pattern is clearly indicated by the high values of ε' and ε'' at different temperatures (Figures 1(a)-1(b)). Consequently, researchers suggested using complex electric modulus $M^*(\omega)$ and conductivity $\sigma^*(\omega)$ functions to

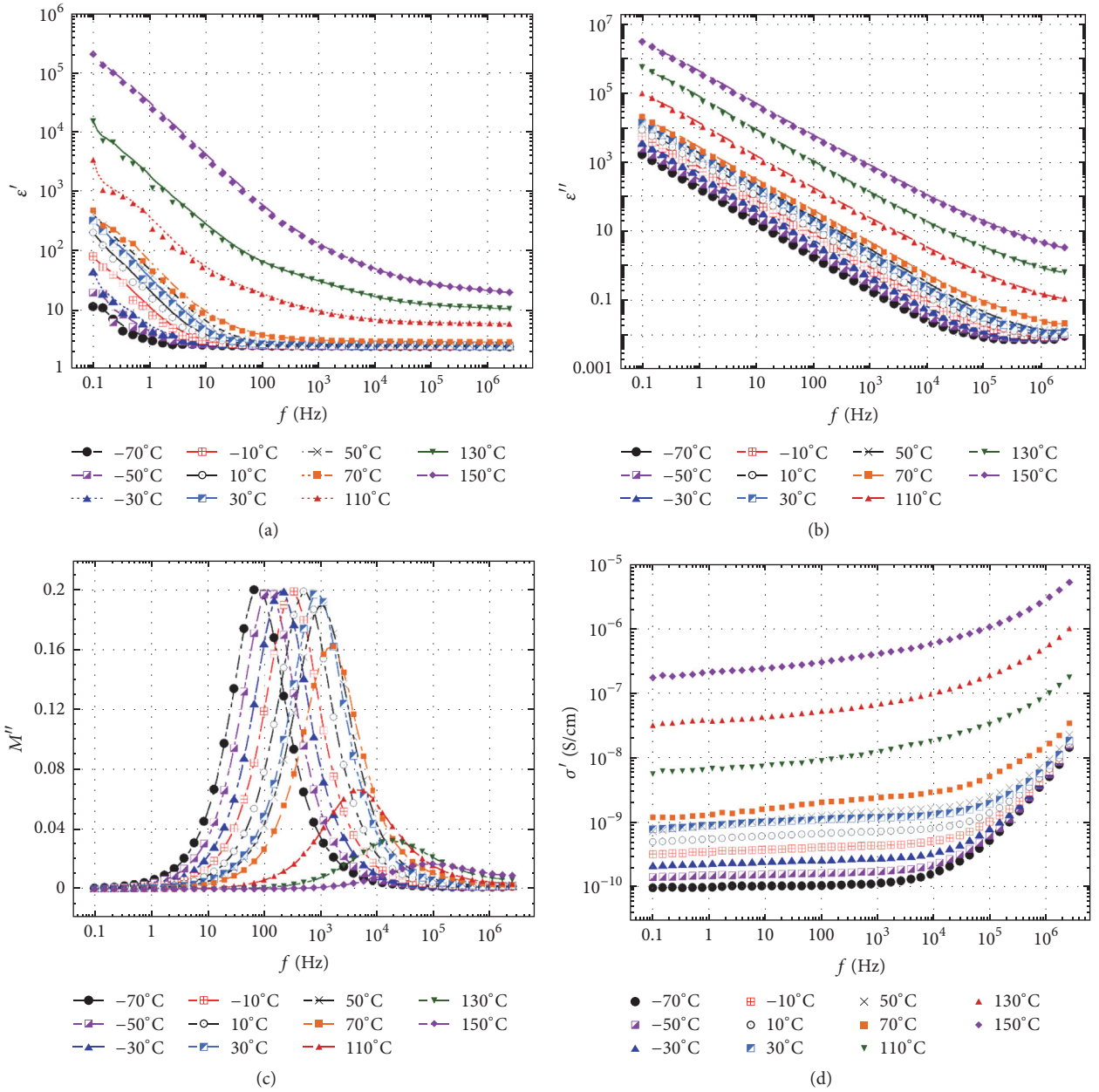

Figure 1: Dielectric permittivity storage (a), loss (b), electrical modulus (c), and AC conductivity (d) for the PANI-PS-0.2 CSA sample at different temperatures.

analyse the dielectric spectra of the conductive materials [25–29]. These functions are related via the equation:

$$M^*(\omega) = \frac{1}{\varepsilon^*(\omega)} = \frac{1}{(\varepsilon' - i\varepsilon'')} = \frac{i\varepsilon_o\omega}{\sigma^*(\omega)}, \quad (1)$$

where $\sigma^* = \sigma' + i\sigma''(\sigma' = \varepsilon_o\omega\varepsilon''; \sigma'' = \varepsilon_o\omega\varepsilon')$ and $M^* = M' + iM''(M' = \varepsilon'/(\varepsilon'^2 + \varepsilon''^2); M'' = \varepsilon''/(\varepsilon'^2 + \varepsilon''^2))$.

The conductivity relaxation peak shifts to lower frequencies as the temperature decreases, indicating slower charge motion (Figure 1(c)). Additionally, the intensity of the M'' relaxation peak increases with cooling and reaches a constant value once the glass transition of PANI (around 40°C) [30, 31] is reached. No other relaxation modes are evident in the M'' spectra of this sample (PANI-PS-0.2 CSA). The AC conductivity (σ') of the PANI-PS-0.2 CSA sample is shown (Figure 1(d)). AC conductivity exhibits a typical behaviour for polymers and disordered solids. It has frequency independence at low frequencies and then upsurges monotonically with the s-the power of frequency, where s ranges from 0.7 to 1.0 [32]. Conductivity plateaus at a low frequency corresponding to the DC conductivity, and the

frequency at which it becomes frequency-dependent is called the relaxation frequency, ω_s. DC conductivity increases and the plateau widens to include the entire frequency range at higher temperatures.

In order to study the contribution of the CSA dopant to the electron transport performance of the samples, comparative 3D isochronal diagrams (M'' versus temperature and frequency, f) for the all-PANI-PS blends and pure PANI films were developed (Figure 2). Two relaxations were noted: namely, the conductivity and the PANI or PS T_g-related peaks. The pure PANI and 0.2 M CSA-doped samples exhibited strong conductivity relaxation and some features around 50°C, which could be related to the long-range T_g motions of the PANI and PS chains. In these two samples, high conduction resulting from multiple electron hopping events completely overwhelmed the polarizability attained from the dipolar chain motion. However, in the 0.3–0.5 M CSA-doped samples, electron hopping events were comparatively low, and the conduction relaxation peaks were weaker compared to those arising from the dipolar chain motions. This change in behaviour associated with increased concentrations of CSA dopant in the blends was further illustrated by the dielectric permittivity loss (ε'') versus f spectra at 20°C. Very high ε'' values at low f were observed for pure PANI, and a rapid drop as the CSA content increased in the blend was evident (Figure 3). High values of ε'' at a low f corresponded to the DC electrical conductivity, σ_{dc}, which resulted from free charge polarization within the material [33]. This charge polarization completely overwhelmed the PANI polymer chain relaxation, which was evident for the samples containing 0.3 M, 0.4 M, and 0.5 M CSA.

AC conductivity behaviour at 20°C for all samples was examined (Figure 4). The DC conductivity increased, and the plateau widened to include most of the measured frequency ranges for only pure PANI and the 0.2 M CSA-doped samples. For CSA concentrations above 0.2 M, the conductivity did not show any plateaus and its gradual increase with increasing frequency was mainly due to the motion of the PANI and PS chain dipoles (relaxation region) [34]. The temperature dependence of DC conductivity indicated that the observed metallic DC conductivity was due to only a small fraction of delocalized carriers, which are primarily present in metallic islands. Furthermore, this is the achievable conductivity for such systems when the entire charge carrier density participates are very high [6]. It has also been shown that the relaxation of the charge carrier system is attributed to the charge hopping of mobile carriers, which can lead to both short-range σ_{ac} and long-range σ_{dc}. Saravanan et al. reported the attachment of sulfonic acid group to the lone pair of electrons on the NH groups in the polyaniline chain without altering the aromatic ring (Figure 5) [19]. Therefore, increasing PANI loading should increase AC conductivity, which was reported by Belaabed et al. for the PANI/epoxy composites. This is because of two reasons. First, increasing the PANI content will lead to an increased charge carrier concentration, making it easier for better interparticle contact and, thus, the formation of a conducting network. Second, differences in the dielectric constant and conductivity of PANI and the surrounding epoxy matrix may lead to the Maxwell-Wagner-Sillars (MWS) interfacial polarization effect because of the accumulation of mobile charges at the interfaces between the two matrices [34, 35]. PANI dipole density, mobility of the dipoles, and the mobility of the surrounding matrix polymer chains are some of the important parameters required for the MWS polarization phenomena to occur. In our system, however, the amount of PANI is fixed for all samples, and the CSA content is the only variable among the composite samples. Therefore, the availability of the NH groups' electrons is the only parameter that governs the conductivity behaviour exhibited in Figure 4.

Table 1: Conduction activation energies for the pure PANI and PANI-PS blends containing various concentrations of CSA.

Samples	Activation energy (eV)	R^2 value
Pure PANI	0.023	0.9847
PANI-PS-CSA-0.2	0.055	0.9877
PANI-PS-CSA-0.3	0.587	0.9816
PANI-PS-CSA-0.4	0.521	0.9829
PANI-PS-CSA-0.5	0.721	0.9629

The temperature dependence of the dc DC conductivity (σ_{dc}) is presented (Figure 6). Plateau values of the AC conductivity at low frequency (Figure 4) were used to obtain the σ_{dc} values, which accounted for the long-range hopping of the charge carriers of the NH groups [36, 37]. Charge carriers typically accomplish more simple hops before the applied electric field reverses at low frequency, resulting in the DC conduction effect. These hops are also facilitated above the matrix T_g because of the increased segmental mobility of the polymer chains, which causes the charge carriers to become more mobile [33]. The observed temperature dependence of σ_{dc} (Figure 6) exhibited Arrhenius behaviour according to the equation:

$$\sigma_{dc} = \sigma_o \exp\left(-\frac{E_a}{k_B T}\right), \tag{2}$$

where σ_o is the per-exponent factor, k_B is the Boltzmann constant, and E_a is the activation energy for the conduction process. Conduction activation energy values were calculated from the slopes of the linear correlations (Figure 6, Table 1). The conduction activation energy is the minimum energy required to overcome the potential barrier in polymeric systems. As expected, pure PANI had the lowest activation energy, and the values increased with increasing concentrations of CSA in the blends, confirming the attachment of sulfonic acid groups to the electrons of the NH groups, which was noted above. This low energy barrier for pure PANI and the 0.2 M CSA-doped samples reflected metallic or narrow band-gap semiconducting behaviour and it was close to the values previously reported for other conductive polymer composites [37]. Only these two samples showed DC conduction, which was indicated by the plateau in the σ' versus the f plots over a wide range of temperatures starting at −70°C. However, samples with higher CSA doping started to show this type of conduction only at 50°C, which is greater than the T_g of polyaniline [30, 31].

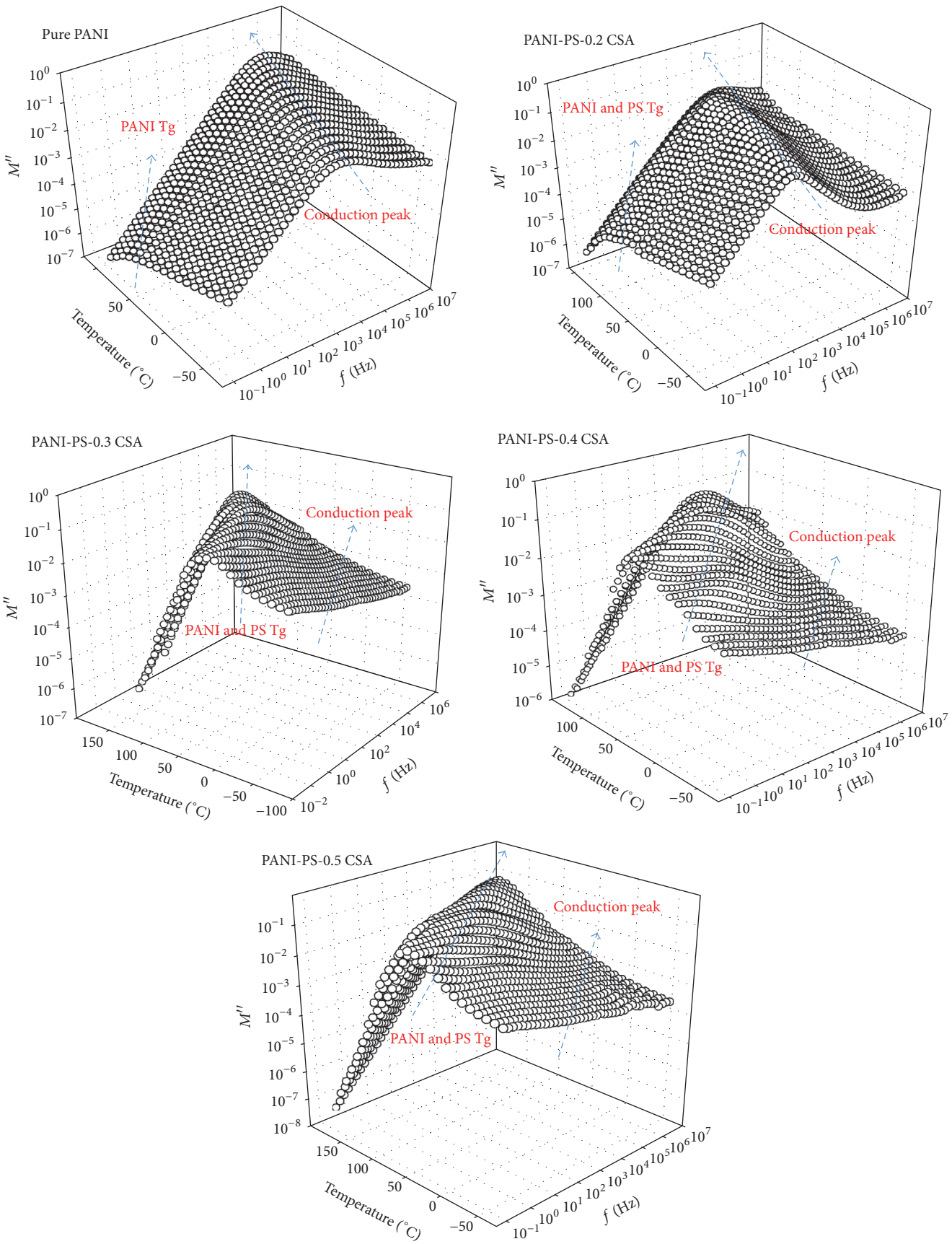

Figure 2: 3D plots of the electrical modulus versus temperature and frequency for the samples.

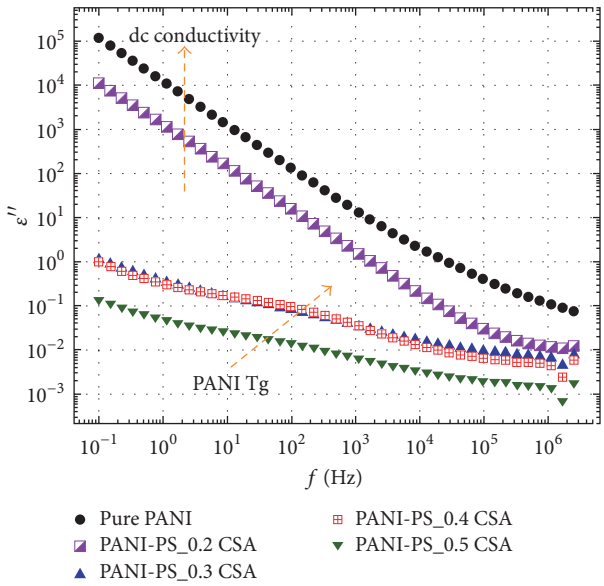

Figure 3: ε'' versus f at 20°C for the pure PANI and PANI-PS blends containing variable CSA concentrations.

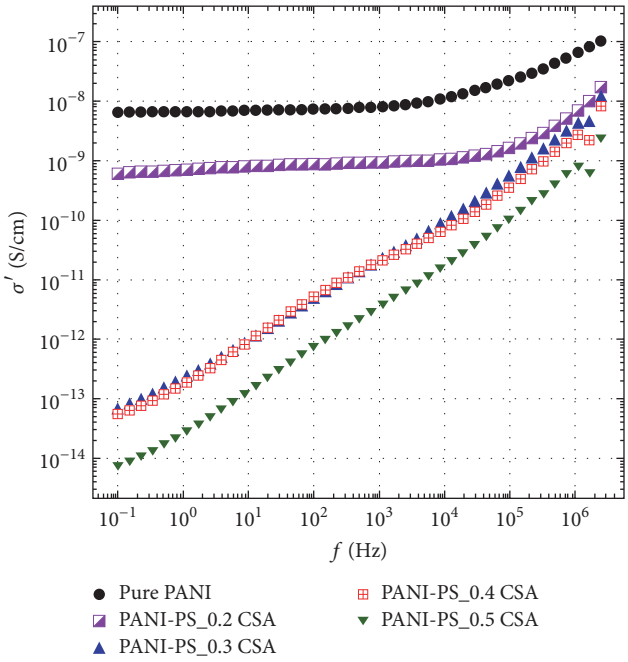

Figure 4: AC conductivity versus frequency at 20°C for pure PANI and PANI-PS blends samples with different composition.

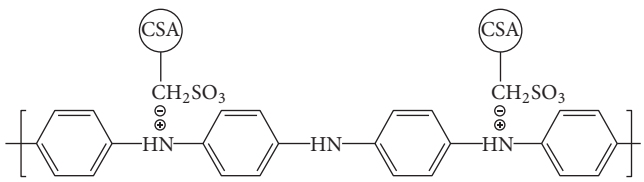

Figure 5: Interaction of the camphor sulfonic acid with polyaniline.

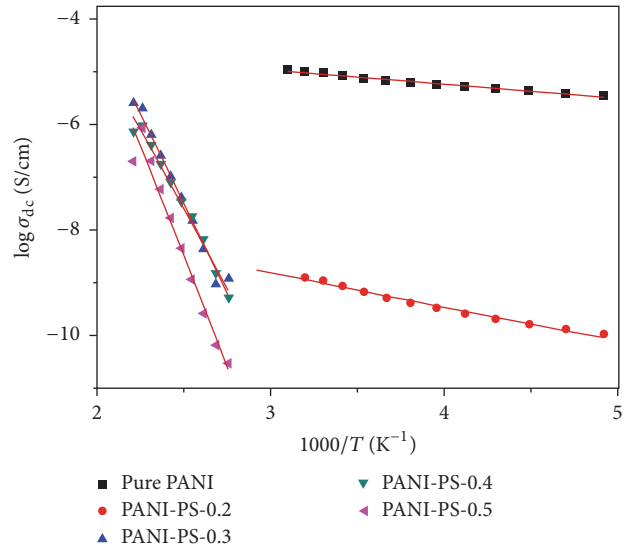

Figure 6: Temperature dependence of σ_{dc} for the pure PANI and PANI-PS blends of different compositions.

3.2. SEM Analysis. SEM was performed on the pure PANI and four CSA-doped PANI-PS blends (Figure 7). The pure PANI sample displayed a fibrous morphology of nanodimension, whereas the blends showed some agglomeration that increased with higher dopant concentrations. A chemical blending method was used for sample preparation of PANI and PS for the miscible and phased materials.

3.3. DSC Analysis. A DSC analysis was used to examine the changes in glass transition temperatures of the blends as the CSA concentrations varied. Because not many significant changes were seen for all the steps except the second heating of the DSC thermogram, only the second heating curves are shown (Figure 8). No T_g was observed for pure HCl-doped PANI as expected from the literature [30, 31]. Nevertheless, in all the CSA-doped PANI-PS blends, we observed T_g at about 90°C, which was also observed in the dielectric results above. There was not much difference in T_g with regard to the concentration of the dopant in the blends.

4. Conclusion

Broadband dielectric spectroscopy was used to examine the AC conductivity of PANI-PS blends containing different concentrations of the CSA dopant. The electrical conduction response of the samples strongly correlated with the CSA concentration in the blend. Samples containing only pure PANI or a small concentration of CSA showed very high values for dielectric loss (ε'') and storage (ε'), which suggested the existence of electrode polarization and Maxwell-Wagner-Sillars interfacial polarization effects, especially at low frequencies and higher temperatures. These samples clearly display strong conductivity relaxation, which overwhelmed the dipolar relaxation associated with the long-range glass transition-related motions of the PANI and PS chains. However, as the CSA concentration increased, the conduction relaxation

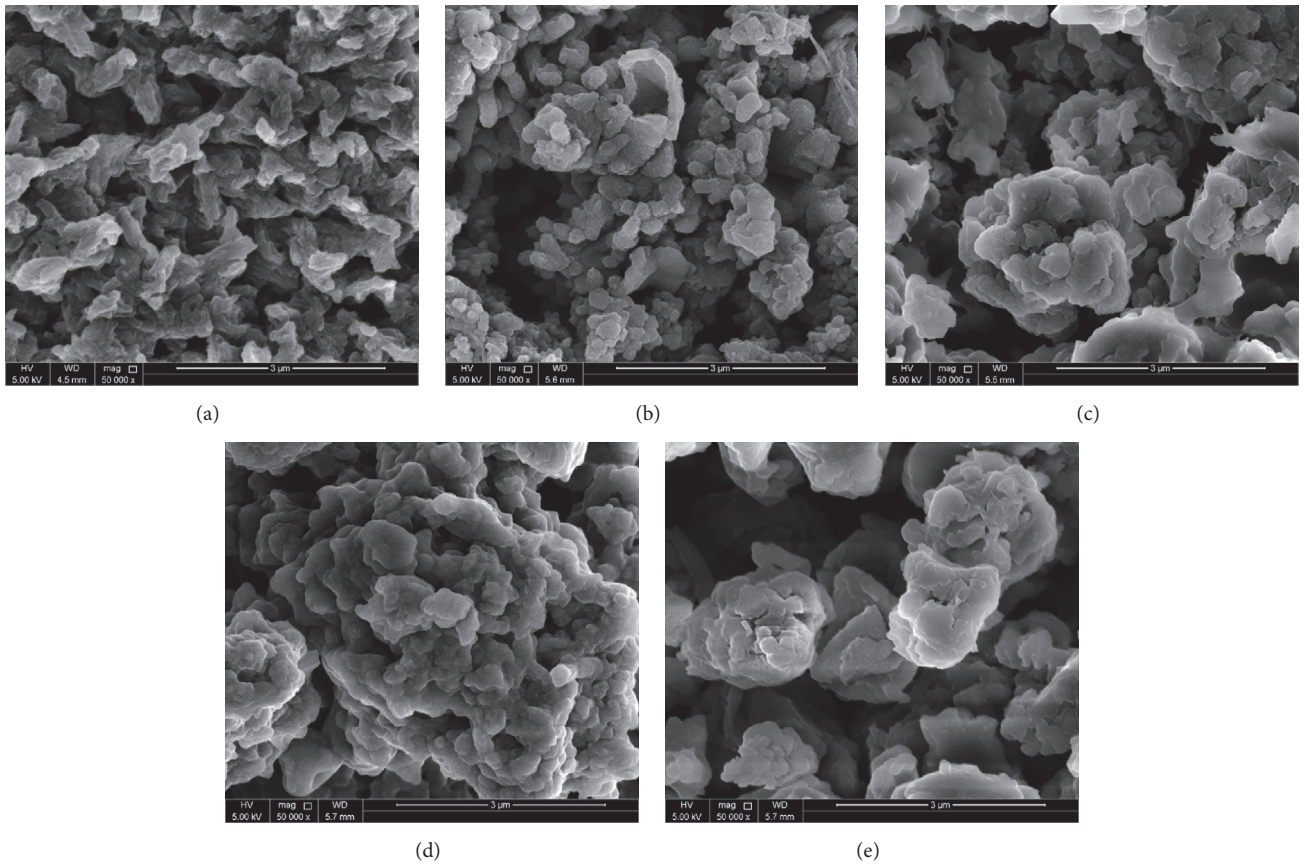

Figure 7: SEM images of pure PANI and CSA-doped PANI-PS blends. (a) Pure PANI, (b) PANI-PS 0.2 M CSA, (c) PANI-PS 0.3 M CSA, (d) PANI-PS 0.4 M CSA, and (e) PANI-PS 0.5 M CSA.

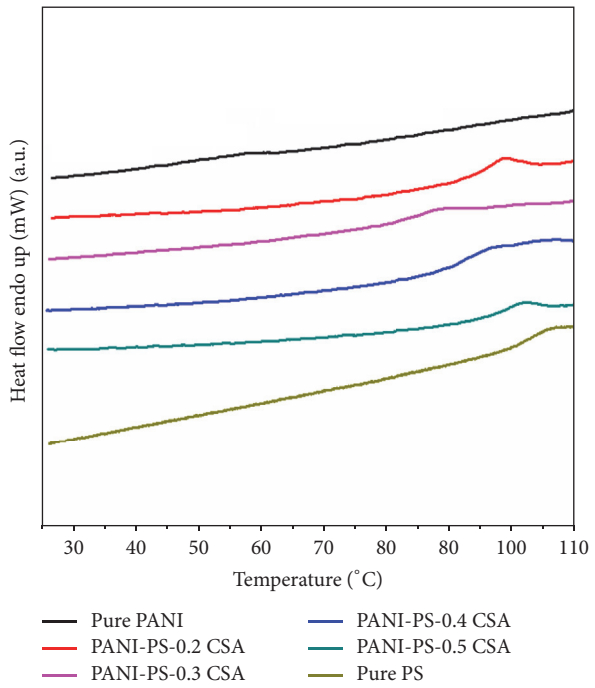

Figure 8: DSC analysis of the pure PANI and PANI-PS blends.

peaks became weaker and could be easily distinguished from the dipolar chain motion peaks. This is thought to be due to the unavailability of the electron pairs of the NH groups, which become progressively attached to the increased population of the electron-withdrawing sulfonic acid groups at higher CSA concentrations. All samples displayed a strong Arrhenius behaviour for the log σ_{dc} versus temperature plots with different values of activation energies, and this correlates well with the concentration of the CSA in the blends.

Data Availability

The data used to support the findings of this study are available from the corresponding author upon request.

Conflicts of Interest

The authors declare that they have no conflicts of interest.

Acknowledgments

The authors would like to acknowledge the financial support of the Qatar University Grant no. QUST-CAM-SPR-2017-6.

References

[1] K. C. Persaud, "Polymers for chemical sensing," *Materials Today*, vol. 8, no. 4, pp. 38–44, 2005.

[2] Y. S. Negi and P. V. Adhyapak, "Development in polyaniline conducting polymers," *Journal of Macromolecular Science*, vol. 42, no. 1, pp. 35–53, 2002.

[3] A. Kumar, V. Kumar, and K. Awasthi, "Polyaniline-carbon nanotube composites: preparation methods, properties, and applications," *Polymer-Plastics Technology and Engineering*, vol. 57, no. 2, pp. 70–97, 2017.

[4] H. Khatoon and S. Ahmad, "A review on conducting polymer reinforced polyurethane composites," *Journal of Industrial and Engineering Chemistry*, vol. 53, pp. 1–22, 2017.

[5] M. A. Kamarudin, S. R. Sahamir, R. S. Datta, B. D. Long, M. F. M. Sabri, and S. M. Said, "A review on the fabrication of polymer-based thermoelectric materials and fabrication methods," *The Scientific World Journal*, vol. 2013, Article ID 713640, 17 pages, 2013.

[6] J. Bhadra, N. J. Al-Thani, N. K. Madi, and M. A. Al-Maadeed, "Preparation and characterization of chemically synthesized polyaniline-polystyrene blends as a carbon dioxide gas sensor," *Synthetic Metals*, vol. 181, pp. 27–36, 2013.

[7] G. Kaur, R. Adhikari, P. Cass, M. Bown, and P. Gunatillake, "Electrically conductive polymers and composites for biomedical applications," *RSC Advances*, vol. 5, no. 47, pp. 37553–37567, 2015.

[8] D. Nguyen and H. Yoon, "Recent advances in nanostructured conducting polymers: from synthesis to practical applications," *Polymer*, vol. 8, no. 4, article 118, 38 pages, 2016.

[9] T. Kobayashi, H. Yoneyama, and H. Tamura, "Polyaniline film-coated electrodes as electrochromic display devices," *Journal of Electroanalytical Chemistry*, vol. 161, no. 2, pp. 419–423, 1984.

[10] M. G. Han, S. K. Cho, S. G. Oh, and S. S. Im, "Preparation and characterization of polyaniline nanoparticles synthesized from DBSA micellar solution," *Synthetic Metals*, vol. 126, no. 1, pp. 53–60, 2002.

[11] S. Bhadra, D. Khastgir, N. K. Singha, and J. H. Lee, "Progress in preparation, processing and applications of polyaniline," *Progress in Polymer Science*, vol. 34, no. 8, pp. 783–810, 2009.

[12] J. Wu, Q. Li, L. Fan et al., "High-performance polypyrrole nanoparticles counter electrode for dye-sensitized solar cells," *Journal of Power Sources*, vol. 181, no. 1, pp. 172–176, 2008.

[13] T. S. Chew, R. Daik, and M. A. A. Hamid, "Thermal conductivity and specific heat capacity of dodecylbenzenesulfonic acid-doped polyaniline particles-water based nanofluid," *Polymer*, vol. 7, no. 7, pp. 1221–1231, 2015.

[14] Y. Zhou, Y. Wang, D. He et al., "Synthesis and properties of nano-polyaniline films doped with camphor sulfonic acid," *Journal of Nanoscience and Nanotechnology*, vol. 14, no. 5, pp. 3417–3421, 2014.

[15] W. E. Jones Jr., J. Chiguma, E. Johnson, A. Pachamuthu, and D. Santos, "Electrically and thermally conducting nanocomposites for electronic applications," *Materials* , vol. 3, no. 2, pp. 1478–1496, 2010.

[16] B. Fryczkowska, Z. Piprek, M. Sieradzka, R. Fryczkowski, and J. Janicki, "Preparation and properties of composite PAN/PANI membranes," *International Journal of Polymer Science*, vol. 2017, Article ID 3257043, 14 pages, 2017.

[17] J. Laska, K. Zak, and A. Proń, "Conducting blends of polyaniline with conventional polymers," *Synthetic Metals*, vol. 84, no. 1–3, pp. 117-118, 1997.

[18] Y. Roichman, G. I. Titelman, M. S. Silverstein, A. Siegmann, and M. Narkis, "Polyaniline synthesis: Influence of powder morphology on conductivity of solution cast blends with polystyrene," *Synthetic Metals*, vol. 98, no. 3, pp. 201–209, 1999.

[19] S. Saravanan, M. R. Anantharaman, and S. Venkatachalam, "Structural and electrical studies on tetrameric cobalt phthalocyanine and polyaniline composites," *Materials Science and Engineering: B Advanced Functional Solid-State Materials*, vol. 135, no. 2, pp. 113–119, 2006.

[20] M. Kaiser, "Electrical conductivity and complex electric modulus of titanium doped nickelzinc ferrites," *Physica B: Condensed Matter*, vol. 407, no. 4, pp. 606–613, 2012.

[21] G. Turky, J. R. Sangoro, M. A. Rehim, and F. Kremer, "Secondary relaxations and electrical conductivity in hyperbranched polyester amides," *Journal of Polymer Science Part B: Polymer Physics*, vol. 48, no. 14, pp. 1651–1657, 2010.

[22] G. Turky, S. S. Shaaban, and A. Schöenhals, "Broadband dielectric spectroscopy on the molecular dynamics in different generations of hyperbranched polyester," *Journal of Applied Polymer Science*, vol. 113, no. 4, pp. 2477–2484, 2009.

[23] D. K. Moon, K. Osakada, T. Maruyama, and T. Yamamoto, "Preparation of polyaniline by oxidation of aniline using H_2O_2 in the presence of an iron(II) catalyst," *Macromolecular Chemistry and Physics*, vol. 193, pp. 1723–1728, 1992.

[24] I. Yu. Sapurina and M. A. Shishov, "Oxidative polymerization of aniline: molecular synthesis of polyaniline and the formation of supramolecular structures," in *New Polymers for Special Applications*, A. De Souza Gomes, Ed., InTech, 2012.

[25] S. Saravanan, C. Joseph Mathai, M. R. Anantharaman, S. Venkatachalam, and P. V. Prabhakaran, "Investigations on the electrical and structural properties of polyaniline doped with camphor sulphonic acid," *Journal of Physics and Chemistry of Solids*, vol. 67, no. 7, pp. 1496–1501, 2006.

[26] N. Rajeswari, S. Selvasekarapandian, S. Karthikeyan et al., "Conductivity and dielectric properties of polyvinyl alcohol-polyvinylpyrrolidone poly blend film using non-aqueous medium," *Journal of Non-Crystalline Solids*, vol. 357, no. 22-23, pp. 3751–3756, 2011.

[27] N. Bohli, A. Belhadj Mohamed, V. Vignéras-Lefèbvre, and J.-L. Miane, "Dielectric and rheological properties of polyaniline organic dispersions," *The European Physical Journal Applied Physics*, vol. 46, no. 2, Article ID 20405, 2009.

[28] R. Bosisio, C. Gorini, G. Fleury, and J.-L. Pichard, "Gate-modulated thermopower of disordered nanowires: II. Variable-range hopping regime," *New Journal of Physics* , vol. 16, Article ID 095005, 2014.

[29] H. Abdalla, K. Van De Ruit, and M. Kemerink, "Effective temperature and universal conductivity scaling in organic semiconductors," *Scientific Reports*, vol. 5, Article ID 16870, 2015.

[30] L. F. Malmonge, S. Do Carmo Langiano, J. M. M. Cordeiro, L. H. C. Mattoso, and J. A. Malmonge, "Thermal and mechanical properties of PVDF/PANI blends," *Materials Research*, vol. 13, no. 4, pp. 465–470, 2010.

[31] K. Adrjanowicz, K. Kaminski, M. Dulski et al., "Dynamic glass transition and electrical conductivity behavior dominated by proton hopping mechanism studied in the family of hyperbranched Bis-MPA polyesters," *Macromolecules* , vol. 47, no. 16, pp. 5798–5807, 2014.

[32] R. Khazaka, M. L. Locatelli, S. Diaham, P. Bidan, L. Dupuy, and G. Grosset, "Broadband dielectric spectroscopy of BPDA/ODA

polyimide films," *Journal of Physics D: Applied Physics*, vol. 46, no. 6, Article ID 065501, 2013.

[33] B. M. Greenhoe, M. K. Hassan, J. S. Wiggins, and K. A. Mauritz, "Universal power law behavior of the AC conductivity versus frequency of agglomerate morphologies in conductive carbon nanotube-reinforced epoxy networks," *Journal of Polymer Science Part B: Polymer Physics*, vol. 54, no. 19, pp. 1918–1923, 2016.

[34] B. Belaabed, S. Lamouri, N. Naar, P. Bourson, and S. O. S. Hamady, "Polyaniline-doped benzene sulfonic acid/epoxy resin composites: Structural, morphological, thermal and dielectric behaviors," *Polymer Journal*, vol. 42, no. 7, pp. 546–554, 2010.

[35] A. Choudhury, "Polyaniline/silver nanocomposites: dielectric properties and ethanol vapour sensitivity," *Sensors and Actuators B: Chemical*, vol. 138, no. 1, pp. 318–325, 2009.

[36] A. K. Jonscher, "Dielectric relaxation in solids," *Journal of Physics D: Applied Physics*, vol. 32, no. 14, pp. R57–R70, 1999.

[37] P. Sobolčiak, A. Ali, M. K. Hassan et al., "2D Ti3C2Tx (MXene)-reinforced polyvinyl alcohol (PVA) nanofibers with enhanced mechanical and electrical properties," *PLoS ONE*, vol. 12, no. 8, Article ID e0183705, 2017.

Hindawi
International Journal of Polymer Science
Volume 2018, Article ID 4541937, 10 pages
https://doi.org/10.1155/2018/4541937

Research Article

Dielectric Properties of Azo Polymers: Effect of the Push-Pull Azo Chromophores

Xuan Zhang,[1] Ziqi Wen,[1] Hongxing Zhang,[2] Weihua Han,[2] Jinyi Ma,[2] Renbo Wei,[2] and Xiufu Hua[3]

[1]*Department of Chemical Engineering, Northwest University, Xi'an 710069, China*
[2]*Center for Applied Chemistry, University of Electronic Science and Technology of China, Chengdu 610054, China*
[3]*Department of Scientific Research and Development, Tsinghua University, Beijing 100084, China*

Correspondence should be addressed to Renbo Wei; weirb10@uestc.edu.cn and Xiufu Hua; huaxf@mail.tsinghua.edu.cn

Received 12 December 2017; Accepted 16 January 2018; Published 12 February 2018

Academic Editor: Hossein Roghani-Mamaqani

The relationship between the structure and the dielectric properties of the azo polymers was studied. Four azo polymers were synthesized through the azo-coupling reaction between the same precursor (PAZ) and diazonium salts of 4-aminobenzoic acid ethyl ester, 4-aminobenzonitrile, 4-nitroaniline, and 2-amino-5-nitrothiazole, respectively. The precursor and azo polymers were characterized by ^{1}H NMR, FT-IR, UV-vis, GPC, and DSC. The dielectric constant and dielectric loss of the samples were measured in the frequency range of 100 Hz–200 kHz. Due to the existence of the azo chromophores, the dielectric constant of the azo polymers increases compared with that of the precursor. In addition, the dielectric constant of the azo polymers increases with the increase of the polarity of the azo chromophores. A random copolymer (PAZ-NT-PAZ) composed of the azo polymer PAZ-NT and the precursor PAZ was also prepared to investigate the content of the azo chromophores on the dielectric properties of the azo polymers. It showed that the dielectric constant increases with the increase of the azo chromophores. The results show that the dielectric constant of this kind of azo polymers can be controlled by changing the structures and contents of azo chromophores during the preparation process.

1. Introduction

Dielectric materials which can be used to control and/or store charge and electric energy play an important strategic role in modern electronic and power systems. With the rapid development of the electric industry, dielectric materials have been intensively investigated in recent years owing to their fascinating properties and potential applications in electronic devices [1, 2]. Up to now, the most used dielectric materials are the inorganic dielectric materials (inorganic piezoelectric ceramic materials) including titanium dioxide [3], calcium titanate [4], magnesium titanate [5], barium titanate [6, 7], mica [8], boron nitride [9], aluminum oxide [10], among others. Although the inorganic dielectric materials usually show higher dielectric constant which is critical for its application, its fragility and high processing temperature limit its further application. With the development of information technology and microelectronics industry, the miniaturization, integration, and intellectualization of new devices such as dielectric substrate, dielectric antenna, and embedded thin film capacitor require that the dielectric materials not only show excellent dielectric properties but also have good mechanical properties and processing properties [11, 12].

The dielectric materials including the polypropylene (PP) [13], biaxially oriented polypropylene (BOPP) [14], polyethylene terephthalate (PET) [15], poly(vinylidene fluoride) (PVDF) [16, 17], and polyarylene ether nitrile (PEN) [18–22], among others, have recently attracted considerable attention from the material research community. In comparing with the inorganic dielectric materials, the dielectric materials especially the polymeric dielectric materials exhibit the advantages of low intrinsic density, excellent

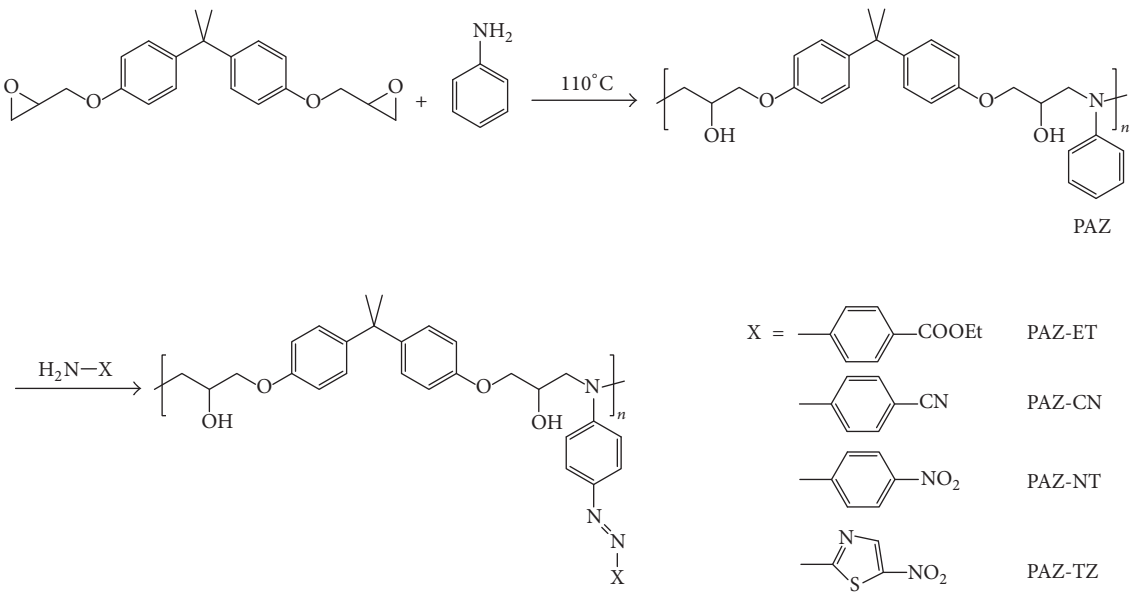

Figure 1: Synthetic route for the azo polymers.

performance, easy processing, long serving life, and even recyclability [11]. However, pure polymer material suffers from the defect of low dielectric constant [21, 22]. As a result, preparing polymer-based composite which combines the advantages of polymer material and inorganic additive has been intensively investigated in recent years [23–25]. However, the addition of the inorganic additive also results in the increment of the dielectric loss of the system [23, 24]. Another method to improve the dielectric constant of a polymer is to increase the polar groups in the polymer, as the dielectric constant indicates how easily a material can become polarized by imposition of an electric field on an insulator [21]. For example, PEN is widely used as dielectric materials for its high dielectric constant attributing to the polar cyano groups as the side-chains on the backbone [18–21]. PVDF is also one of the mostly used dielectric materials due to its high dielectric constant resulting from the asymmetrical fluorine [16, 17].

Azobenzene as a functional group has been widely used to design materials with photoresponsive property [26–29]. When irradiated with appropriate light, polymers containing azobenzene groups (azo polymers for short) will show different photoresponsive properties attributing to the reversible photoinduced *trans-cis* isomerization of the azo chromophores [30–33]. The photoresponsive properties and applications of azo polymers include photoinduced birefringence [34], dichroism [35], surface-relief-grating [36, 37], spontaneous surface pattern [38], and contraction and bending [39–41], among others. On the other hand, the azobenzene, usually as organic dyes, possesses conjugated molecular structures with large dipole moments resulting from the terminal electron donors and acceptors. Consequently, the azobenzene can be potentially used as the polar groups to fabricate organic dielectric materials [42]. In addition, resulting from the high efficiency of the azo-coupling reaction, azo polymers containing different push-pull azo chromophores can be easily obtained [43–46]. As a result, the relationship between the structure and the dielectric properties of the azo polymers can be systematically investigated.

In this work, the relationship between the structure and the dielectric properties of the azo polymers was studied. An epoxy-based precursor was firstly synthesized by condensation polymerization from bisphenol A diglycidyl ether and aniline. Then, a series of azo polymers with different substituents at $4'$-positions of the azobenzene units were prepared by the azo-coupling reaction from that precursor. The azo polymers were characterized by ^{1}H NMR, FT-IR, UV-vis, GPC, and DSC. The influences of the molecular structures on the dielectric properties of the azo polymers were investigated in detail.

2. Experimental Section

2.1. Materials. Bisphenol A diglycidyl ether (80%), aniline (99%), 2-amino-5-nitrothiazole (97%), and 4-aminobenzonitrile (98%) were purchased from Alfa Aesar, Tianjin, China. 4-Aminobenzoic acid ethyl ester (98%) and 4-nitroaniline (98%) were purchased from J&K chemicals, Beijing, China. Tetrahydrofuran (THF) was purified by distillation with sodium and benzophenone. Deionized water was obtained from a Milli-Q water purification system. All of the other reagents and solvents were purchased commercially and used as received without further purification.

2.2. PAZ. As shown in Figure 1, the precursor polymer (PAZ) and the azo polymers (PAZ-R, R = ET, CN, NT, and TZ) were prepared according to the literature [37]. Bisphenol A

diglycidyl ether (18.8 g, 0.1 mol) and aniline (4.7 g, 0.05 mol) were homogeneously mixed before polymerizing and then polymerized at 110°C for 20 h. The production was dissolved in a $CHCl_3/CH_3OH$ solvent mixture (4 : 1, 200 mL) followed by precipitation in 800 mL of acetone. The polymer was collected by filtration and dried under vacuum for 24 h. ^{1}H NMR (DMSO-d_6): δ = 7.07 (6H, d), 6.82 (4H, d), 6.72 (2H, d), 6.54 (1H, m), 5.27 (1H, d), 5.18 (1H, d), 4.03 (2H, m), 3.87 (4H, s), 3.34–3.75 (4H, m), and 1.55 (6H, s). FT-IR (KBr, cm^{-1}): 3365 (O-H, s), 2963 and 2926 (C-H, m), 1600, 1508, and 1459 (Benz. ring, s), and 1247 (C-O, s). GPC: $M_n = 2.47 \times 10^4$ and $M_w/M_n = 1.69$. DSC: $T_g = 89.8$°C.

2.3. PAZ-CN. According to the literature [37], PAZ (1.3 g, 3 mmol) was dissolved in DMF (150 mL) at 0°C. A diazonium salt of 4-aminobenzonitrile was prepared by adding an aqueous solution of sodium nitrite (0.37 g, 5.5 mmol in 3 mL of water) into a solution of 4-aminobenzonitrile (0.54 g, 4.5 mmol) in a homogeneous mixture of 1.3 mL of sulfuric acid and 18 mL of glacial acetic acid. The mixture was stirred at 0°C for 30 min and then was added dropwise into the solution of PAZ. The solution was stirred at 0°C for another 12 h. Then the solution was poured into plenty of water and the precipitate was collected and dried afterwards. The product was dissolved in 60 mL THF and precipitated into 600 mL petroleum ether. The final product was dried in vacuum at 70°C for 24 h. ^{1}H NMR (DMSO-d_6): δ = 7.93 (2H, d), 7.83 (2H, d), 7.75 (2H, d), 7.06 (4H, d), 6.91 (2H, d), 6.84 (4H, d), 5.40 (H, d), 5.29 (H, d), 4.12 (2H, m), 3.70–4.01 (6H, m), 3.41–3.70 (2H, m), and 1.54 (6H, s). FT-IR (KBr, cm^{-1}): 3400 (O-H, s), 2963 and 2927 (C-H, m), 2227 (C≡N, m), 1600 and 1510 (Benz. ring, s), 1384 (-N=N-, m), and 1247 (C-O, s). GPC: $M_n = 2.96 \times 10^4$ and $M_w/M_n = 1.82$. UV-vis: λ_{max} = 452 nm. DSC: $T_g = 120.5$°C.

2.4. PAZ-ET. PAZ-ET was similarly prepared as mentioned for PAZ-CN. FT-IR (KBr, cm^{-1}): 3397 (O-H, s), 2963 and 2927 (C-H, m), 1713 (C=O, s), 1599, 1510, and 1460 (Benz. ring, s), 1386 (-N=N-, m), and 1241 (C-O, s). ^{1}H NMR (DMSO-d_6): δ = 8.06 (2H, d), 7.82 (2H, d), 7.74 (2H, d), 7.07 (4H, d), 6.90 (2H, d), 6.84 (4H, d), 5.40 (H, d), 5.29 (H, d), 4.30 (2H, t), 4.12 (2H, m), 3.70–4.00 (6H, m), 3.40–3.70 (2H, m), 1.54 (6H, s), and 1.30 (3H, d). GPC: $M_n = 3.16 \times 10^4$ and $M_w/M_n = 1.88$. UV-vis: λ_{max} = 438 nm. DSC: $T_g = 112.7$°C.

2.5. PAZ-NT. PAZ-NT was similarly prepared as mentioned for PAZ-CN. FT-IR (KBr, cm^{-1}): 3420 (O-H, s), 2963 and 2927 (C-H, m), 1602 and 1510 (Benz. ring, s), 1384 (-N=N-, m), and 1243 (C-O, s). ^{1}H NMR (DMSO-d_6): δ = 8 : 32 (2H, d), 7.88 (2H, d), 7.75 (2H, d), 7.06 (4H, d), 6.90 (2H, d), 6.82 (4H, d), 5.40 (H, d), 5.29 (H, d), 4.12 (2H, m), 3.71–4.00 (6H, m), 3.41–3.66 (2H, m), and 1.55 (6H, s). GPC: $M_n = 2.91 \times 10^4$ and $M_w/M_n = 1.78$. UV-vis: λ_{max} = 482 nm. DSC: T_g = 124.8°C.

2.6. PAZ-TZ. PAZ-TZ was prepared according to the literature [44], nitrososulfuric acid was prepared by carefully adding sodium nitrite (0.21 g, 3 mmol) to 2 mL of sulfuric acid at 65°C while stirring. The resulting solution was cooled in an ice bath and diluted with 5 mL of acetic acid. A diazonium salt of 2-amino-5-nitrothiazole was prepared by adding the solid of 2-amino-5-nitrothiazole (0.36 g, 2.5 mmol) directly into the above nitrososulfuric acid solution and stirred at 0°C at least for 2 h. The diazonium salt solution was added dropwise into a solution of PAZ (0.86 g, 2 mmol) in 100 mL DMF at 0°C. The solution was stirred at 0°C for another 12 h. After precipitation of the above solution in water and being dried for 12 h, PAZ-TZ was purified by dissolving in THF and precipitating in petroleum ether and then dried in vacuum for 24 h. FT-IR (KBr, cm^{-1}): 3441 (O-H, s), 3045, 1460, and 753 (thiazole, m), 2964 and 2870 (C-H, m), 1601 and 1508 (Benz. ring, s), 1353 (-N=N-, m), 1340 (N=O, m), and 1240 (C-O, s). ^{1}H NMR (DMSO-d_6): δ = 8.26 (1H, s), 7.80 (2H, d), 7.10 (6H, d), 6.86 (4H, d), 5.40 (H, d), 5.29 (H, d), 4.17 (2H, m), 3.70–4.00 (6H, m), 3.40–3.65 (2H, m), and 1.57 (6H, s). GPC: $M_n = 3.01 \times 10^4$ and $M_w/M_n = 1.84$. UV-vis: λ_{max} = 572 nm. DSC: $T_g = 138.7$°C.

2.7. PAZ-NT-PAZ. PAZ-NT-PAZ would be the random copolymer of PAZ and PAZ-NT, and it was similarly prepared as mentioned for PAZ-NT. However, only 30% of the diazonium salt as preparing PAZ-NT was added to the PAZ solution. ^{1}H NMR (DMSO-d_6): δ = 8.34 (d), 7.89 (d), 7.74 (d), 7.09 (d), 6.90 (d), 6.82 (d), 6.73 (d), 6.54 (m), 5.40 (d), 5.32 (m), 5.18 (d), 4.12 (m), 4.05 (m), 3.87 (s), 3.34–3.75 (m), and 1.55 (s). FT-IR (KBr, cm^{-1}): 3365 (O-H, s), 2963 and 2927 (C-H, m), 1713 (C=O, s), 1600, 1508, and 1459 (Benz. ring, s), 1384 (-N=N-, m), and 1243 (C-O, s). GPC: $M_n = 2.72 \times 10^4$ and $M_w/M_n = 1.75$. UV-vis: λ_{max} = 482 nm. DSC: $T_g = 121.2$°C.

2.8. Characterization. ^{1}H NMR spectroscopy was obtained on a JEOL JNM-ECA300 (300 MHz) or JEOL JNM-ECA400 (400 MHz) NMR spectrometer. FT-IR spectra were collected on a Nicolet 560-IR spectrometer. The molecular weights and molecular weight distributions of the polymers were measured on a gel permeation chromatographic (GPC) instrument which is equipped with a column (PLgel 5 μm Mixed-D) and a refractive index detector (Wyatt Optilab rEX). The temperatures during the measurements were maintained at 35°C and the molecular weights of the polymers were calibrated with polystyrene as standards. Chromatographic THF was used as the eluent agent and the flow rate was controlled to be 1.0 mL/min. The thermal behaviors of the polymers were performed on a TA Instrument DSC-Q100 with a heating rate of 10°C/min from room temperature to 180°C and in a nitrogen atmosphere. The UV-vis spectra of the samples were measured in solution by using a Persee TU-1810SPC UV-vis spectrophotometer, the concentrations of the samples under the concentration of 0.02 mg/mL were obtained by dissolving the corresponding samples in THF

(HP). Dielectric measurements of the azo polymers were carried out by a TH 2819A precision LCR meter. The films of the polymers were firstly obtained by casting the DMF solution of the corresponding polymer on the copper foil and then dried in an oven with the procedure of 80°C for 1 h, 100°C for 1 h, 120°C for 1 h, and 160°C for 2 h. Then, a simple parallel-plate capacitor was fabricated by putting another copper foil on the surface of the polymeric film. The copper foils at both side of the polymeric film were used as the electrodes and the dielectric constant and dielectric loss of the samples were measured at temperature from 100 Hz to 200 kHz.

3. Result and Discussion

In this study, the relationship between the structure and the dielectric properties of the azo polymers was studied. Epoxy-based azo polymers with strong push-pull azo chromophores (PAZ-ET, PAZ-CN, PAZ-NT, and PAZ-TZ) were synthesized from the precursor (PAZ) by azo-coupling reaction [44]. The synthetic route and chemical structure of these polymers are given in Figure 1. The precursor PAZ was synthesized through the condensation polymerization between bisphenol A diglycidyl ether and aniline. According to the GPC results, the number-average molecular weight of PAZ is 2.47×10^4 and the polydispersity index is 1.69. PAZ shows good solubility in polar organic solvents such as tetrahydrofuran, *N*,*N*-dimethylformamide, and *N*,*N*-dimethylacetamide, which is critical for the subsequent azo-coupling reaction. T_g of PAZ is 89.8°C, which is determined by DSC.

The azo polymers (PAZ-ET, PAZ-CN, PAZ-NT, and PAZ-TZ) with strong push-pull azo chromophores were then prepared by the azo-coupling reaction between the precursor PAZ and diazonium salts of 4-aminobenzoic acid ethyl ester, 4-aminobenzonitrile, 4-nitroaniline, and 2-amino-5-nitrothiazole at 0°C in a polar organic solvent such as DMF. The diazonium salts were obtained by adding the solution of sodium nitrite into the acidic aqueous solution of the corresponding amino derivatives or putting the amino derivatives directly into the nitrososulfuric acid at 0°C. The azo-coupling reaction enables introducing various azo chromophores at the final stages of the synthetic route with high yield. As the precursor is the same and excessive diazonium salts were used in the reaction, the only differences between these azo polymers are the azo chromophores linked on the backbone. The azo polymers with strong push-pull azo chromophores are named as PAZ-X, where X is the abbreviations to make the distinction for the different electron-withdrawing groups.

Figure 2 shows the ^{1}H NMR spectra of the precursor and the azo polymers with assignments. For the ^{1}H NMR spectrum of PAZ, the resonance signal at 6.54 ppm is coming from the proton *j* which is on the *para* position of the benzene ring connected to the nitrogen, while the proton *i* on the *ortho* position of the benzene ring connected to the nitrogen shows a resonance peak at 6.72 ppm. The resonance signals at 5.27 and 5.18 ppm are resulting from the protons on hydroxyl groups. After the azo-coupling reaction, PAZ-ET, for example, the resonance signal at 6.54 ppm disappears completely indicating the 100% reaction of the PAZ. In addition, the resonance signals located at 8.06 and 7.82 ppm are coming from the protons on the benzene ring of the azobenzene unit (*k* and *j*). What is more, resonance peaks of the protons on the benzene ring of the azobenzene unit (*h* and *i*) shift to the low field due to the formation of the azobenzene unit. The new resonance peaks at 4.30 (*l*) and 1.30 (*m*) ppm are coming from the methylene and methyl group connected to the ester. For the other azo polymers, the resonance peaks can also be correspondingly assigned which means that the azo polymers are successfully prepared (Figure 2).

The azo polymers were also characterized by FT-IR. In comparing with the FT-IR spectrum of PAZ, a new absorption peak at around 1385 cm^{-1} is observed for all of the azo polymers. This new absorption peak is attributed to the symmetrical stretching vibration of the azo group (-N=N-) [47] which confirms the preparation of the azo polymers. The molecular weights and molecular weight distributions of the polymers were measured by using GPC. The number-average molecular weights of the azo polymers are 3.16×10^4, 2.96×10^4, 2.91×10^4, and 3.01×10^4 for PAZ-ET, PAZ-CN, PAZ-NT, and PAZ-TZ, respectively, which are higher than that of the precursor PAZ. In addition, the molecular weight distributions of the azo polymers are also higher than that of the precursor. The thermal properties of the azo polymers were obtained by using the DSC measurement. Figure 3 shows the DSC curves of the precursor PAZ and the azo polymers PAZ-X. T_g of PAZ is 89.8°C. After the azo-coupling reaction, T_g of the azo polymers increases and is 112.7, 120.5, 124.8, and 138.7°C for PAZ-ET, PAZ-CN, PAZ-NT, and PAZ-TZ respectively. The increment of T_g of the azo polymers is due to the formation of the azobenzene groups and the increasing of the number-average molecular weights of the samples after the azo-coupling reaction.

The UV-vis spectra of the solution of the azo polymers are shown in Figure 4. The concentrations of the solution of the samples are 0.02 mg/mL by dissolving the corresponding solid samples in THF (HP) which is a common solvent for the azobenzene and its derivatives. In comparing with the spectrum of PAZ which shows a weak absorption around 300 nm, the azo polymers show a strong absorption in the visible region and the color of the azo polymers ranges from red to blue. This strong absorption is contributed to azobenzene which also confirms the successfully fabrication of the azo polymers. Azo chromophores are usually classified into azobenzene type, aminoazobenzene type as well as pseudostilbene type based on the spectral feature and isomerization behavior of them [34]. The pseudostilbene type azo chromophores, also known as push-pull type azo chromophores, contain strong electron-donating/electron-withdrawing substituents at the 4 and 4′ positions of the azobenzene moieties which results in the strong absorption bands in the visible light region. According to Figure 4, the position of the absorption band of the azo polymers is

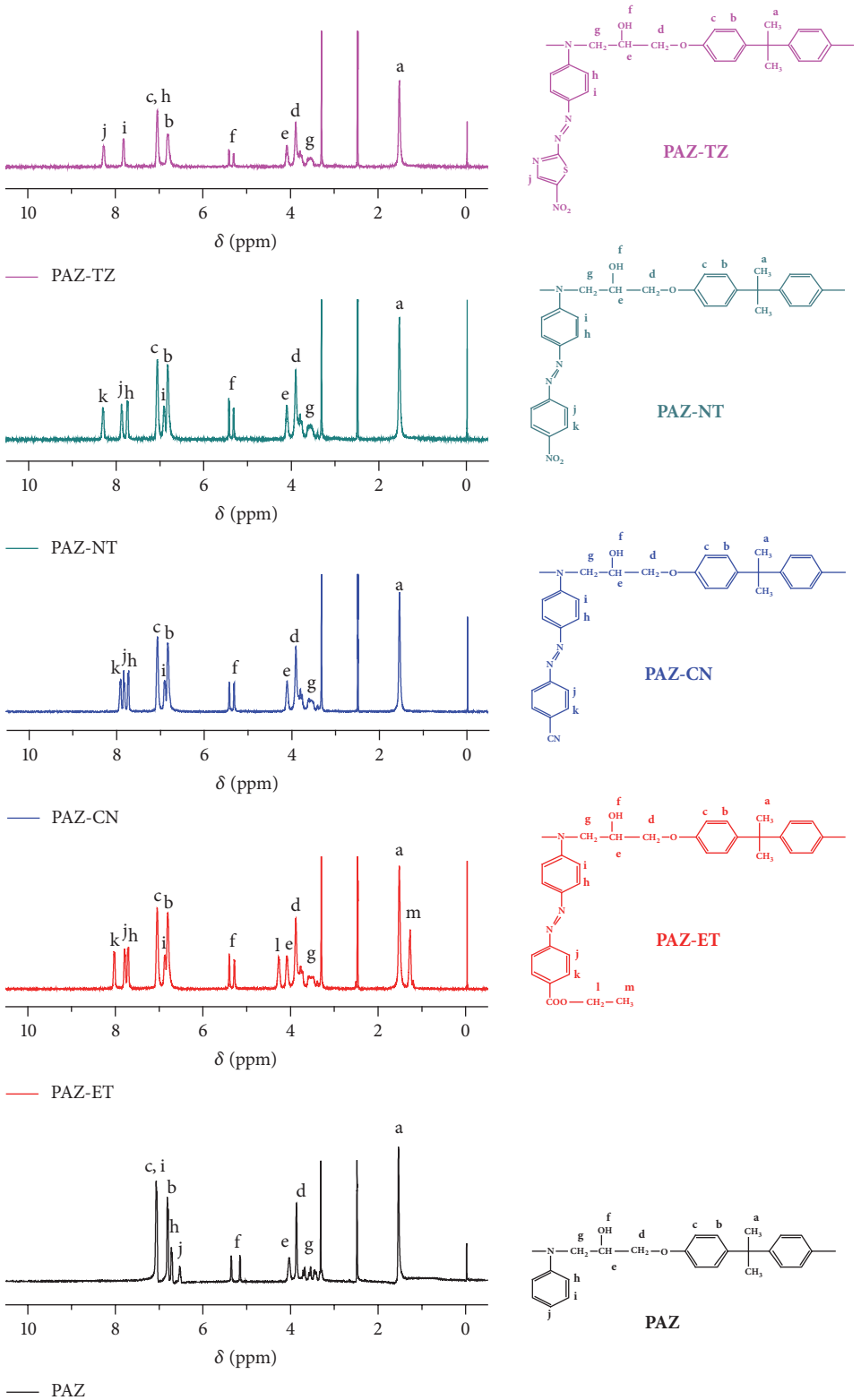

Figure 2: ^{1}H NMR spectra the precursor and the azo polymers.

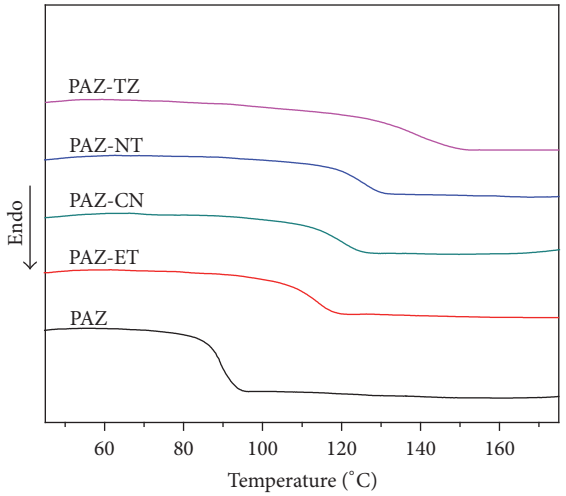

Figure 3: DSC curves of the polymers obtained from the second heating scan.

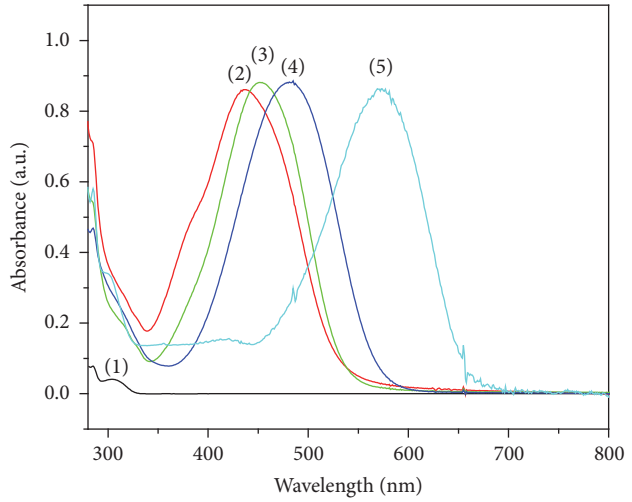

Figure 4: UV-vis spectra of the THF solution (0.02 mg/mL) of the polymers. Curve (1): PAZ, curve (2): PAZ-ET, curve (3): PAZ-CN, curve (4): PAZ-NT, and curve (5): PAZ-TZ.

determined by the electron-withdrawing group on the 4′ positions of azobenzene moieties. The location of the max absorption band (λ_{max}) of the azo polymers is 438, 452, 482, and 572 nm for PAZ-ET, PAZ-CN, PAZ-NT, and PAZ-TZ, respectively. As the azo polymers are made from the same precursor PAZ and have the same electron-donating group on the azobenzene moiety, the red-shift of λ_{max} indicates the polarity of the electron-withdrawing group on the 4′ position of the azobenzene becomes stronger.

The dielectric constant and dielectric loss of the azo polymers and the precursor were measured in the frequency range of 100 Hz–200 kHz. For high performance polymers such as PEN, the dielectric constant, and dielectric loss can be easily measured by using the films of PEN whose surfaces were coated with a thin layer of conductive silver paste to form a plate capacitor [21, 22]. However, as the free standing films of the precursor and the azo polymers cannot be obtained resulting from their poor mechanical property, the samples were firstly cast on the copper foil, and then a simple parallel-plate capacitor was fabricated by putting another copper foil on the surface of the polymeric film. The copper foils at both sides of the polymeric film were used as the electrodes for the measurement of the dielectric constant and dielectric loss. The dielectric constant and dielectric loss of the azo polymers are shown in Figures 5(a) and 5(b). As shown in Figure 5(a), the dielectric constant of the samples decreases slightly with the increasing of measuring frequency. This decrement of the dielectric constant with changing frequency is caused by the effect of the polarization relaxation [21]. The dielectric constant of PAZ is 3.1 at 1 kHz. Due to the existence of the azo chromophores, the dielectric constant of the azo polymers increases compared with that of the precursor. In

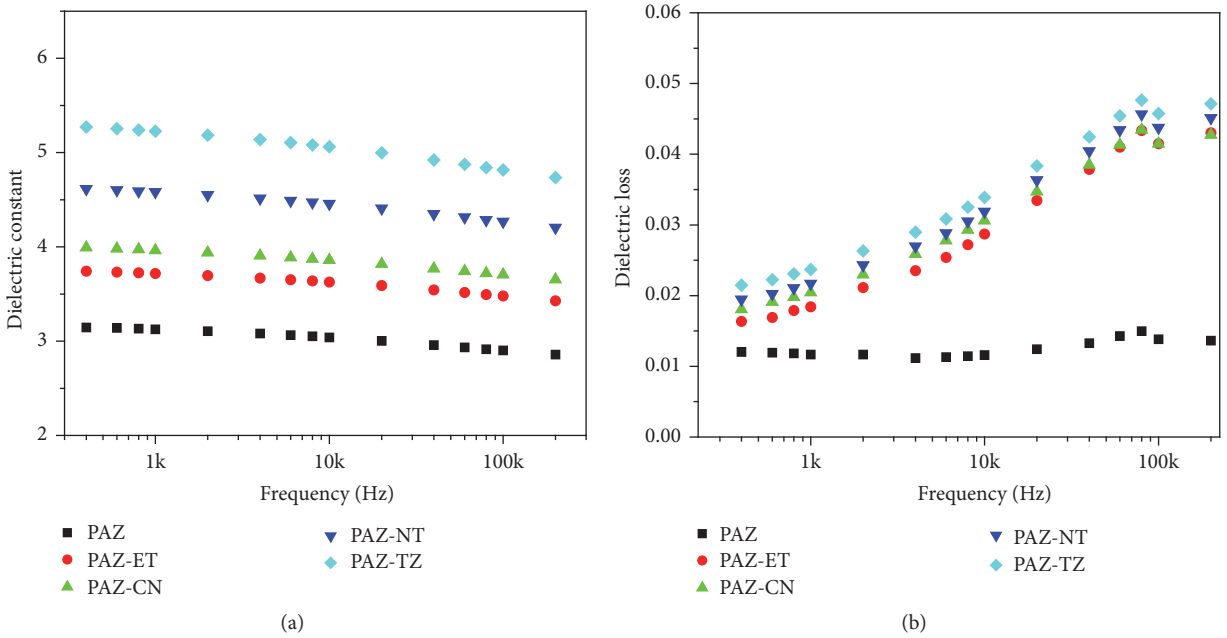

Figure 5: Dielectric constant (a) and dielectric loss (b) of the precursor and the azo polymers.

particular, the dielectric constant of PAZ-ET, PAZ-CN, PAZ-NT, and PAZ-TZ is 3.7, 4.0, 4.6, and 5.2 at 1 kHz, respectively. In addition, the increase of dielectric constant from PAZ-ET to PAZ-TZ would be due to the fact that the electron-withdrawing group on the azobenzene of PAZ-TZ is the strongest. The dielectric loss of the azo polymers is also higher than that of the precursor due to the azo moieties. In addition, as the movement of the polar azobenzene is much easier than the main-chain of the polymers, the dielectric loss increases with the increasing of the frequency. What is more, the dielectric loss increases from PAZ-ET to PAZ-TZ as that of the dielectric constant.

After the study between the structure and the dielectric properties of the azo polymers, the contents of the azo chromophore on the dielectric properties of azo polymers were further studied. Due to the high efficiency of the azo-coupling reaction, the precursor PAZ was 100% reacted to form the azo polymers (PAZ-ET, PAZ-CN, PAZ-NT, and PAZ-TZ) by using excessive diazonium salts, which was confirmed by the ^{1}H NMR spectra. On the other hand, a random copolymer composed of the azo polymer and the precursor would be obtained if inadequate diazonium salt is used. Herein, by using the diazonium salt of the 4-nitroaniline as typical example, PAZ-NT-PAZ which can be seen as the random copolymer of PAZ-NT and PAZ was similarly prepared as mentioned for PAZ-NT. However, only 30% of the diazonium salt as preparing PAZ-NT was added to the PAZ solution when preparing PAZ-NT-PAZ. Figure 6 shows the ^{1}H NMR spectra of PAZ, PAZ-NT-PAZ, and PAZ-NT. In comparing with the ^{1}H NMR spectrum of PAZ-NT, the ^{1}H NMR spectrum of PAZ-NT-PAZ also shows the resonances of the azo chromophore as located at 8.34, 7.89, 7.74, and 6.90 ppm. However, the existence of the resonance peaks at 6.73 and 6.54 ppm indicates the incomplete reaction of the PAZ. In addition, the resonances of the proton from the hydroxyl groups also show the superposition of PAZ and PAZ-NT. According to the integral area of the resonances at 5.40 and 5.18 ppm, it can be calculated that PAZ: PAZ-NT = 6 : 4 in PAZ-NT-PAZ.

The FT-IR spectrum of PAZ-NT-PAZ also shows the absorption peak of the symmetrical stretching vibration of the azo group (-N=N-, 1384 cm^{-1}) which confirms the existence of azo chromophores in PAZ-NT-PAZ. Figure 7 shows the UV-vis spectra of PAZ, PAZ-NT-PAZ, and PAZ-NT in THF at 0.02 mg/mL. In comparing with the UV-vis spectrum of PAZ-NT (curve (3)), the UV-vis spectrum of PAZ-NT-PAZ (curve (2)) shows the same max absorption band at 482 nm. This result indicates the existence of the same azo chromophores in PAZ-NT-PAZ and PAZ-NT. In addition, the intensity of the max absorption band of PAZ-NT-PAZ is about 0.4 to that of the PAZ-NT, the same as the result of the ^{1}H NMR spectra. Combining the ^{1}H NMR spectra and UV-vis spectra, it can be concluded that the ratio of the azo chromophores in PAZ-NT-PAZ with that in PAZ-NT is 0.4.

The dielectric constant and dielectric loss of PAZ-NT-PAZ were also measured in the frequency range of 100 Hz–200 kHz. As shown in Figure 8, the dielectric constant of PAZ-NT-PAZ is 4.1 at 1 kHz which is between that of the PAZ and PAZ-NT. This is because that the content of the azo chromophores which contributes to the increases of the

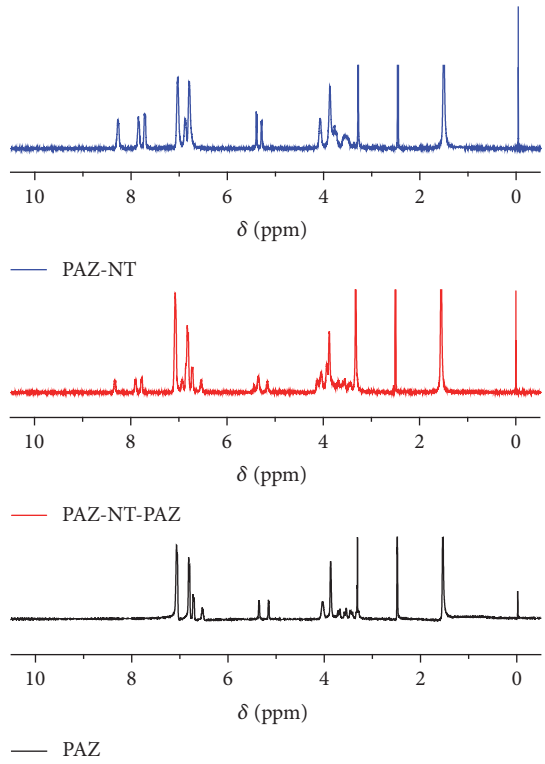

Figure 6: ^{1}H NMR spectra of the PAZ, PAZ-NT, and PAZ-NT-PAZ.

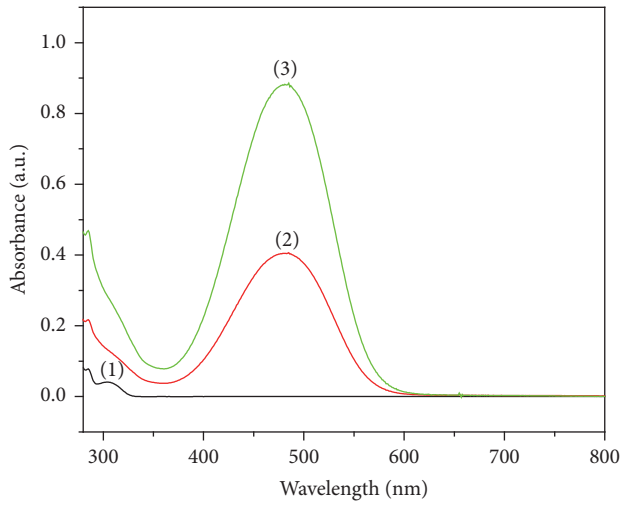

Figure 7: UV-vis spectra of the THF solution (0.02 mg/mL) of the polymers. Curve (1): PAZ, curve (2): PAZ-NT-PAZ, and curve (3): PAZ-NT.

dielectric constant is 0.4 to that of in PAZ-NT. As a result, it can be concluded that the dielectric constant of this kind of azo polymer can be controlled by changing the content of azo chromophores during the preparation process. The dielectric loss of PAZ-NT-PAZ is similar to that of PAZ-NT. However, as the content of azo chromophores is less, the dielectric loss of PAZ-NT-PAZ is lower than that of PAZ-NT at all the tested frequencies.

4. Conclusions

In summary, a series of epoxy-based azo polymers with different substituents at 4′-positions of the azobenzene units were synthesized through the azo-coupling reaction. The ^{1}H NMR spectra indicated the successful preparation of the azo polymers and the UV-vis spectra showed that the max absorption band of the azo polymers red-shifts with the increase of the electron-withdrawing ability of the groups at 4′-positions of the azobenzene unit. The dielectric properties of the azo polymers were obtained by pasting two copper foils which were used as the electrodes during the measurement at both sides of the polymeric film. In comparing with the precursor PAZ, the dielectric constant of the azo polymers increased obviously due to the large dipole moments of the azo chromophore. In addition, the dielectric constant of the azo polymers increased with the increase of the polarity of the azo chromophores and was as high as 5.2 for PAZ-TZ at 1 kHz. A random copolymer PAZ-NT-PAZ composed of PAZ-NT and PAZ was similarly prepared to investigate the content of the azo chromophores on the dielectric properties of the azo polymers. The dielectric constant of PAZ-NT-PAZ was 4.1 at 1 kHz which is between that of PAZ and PAZ-NT. The results showed that the dielectric properties of this kind of azo polymers can be controlled by changing the structures

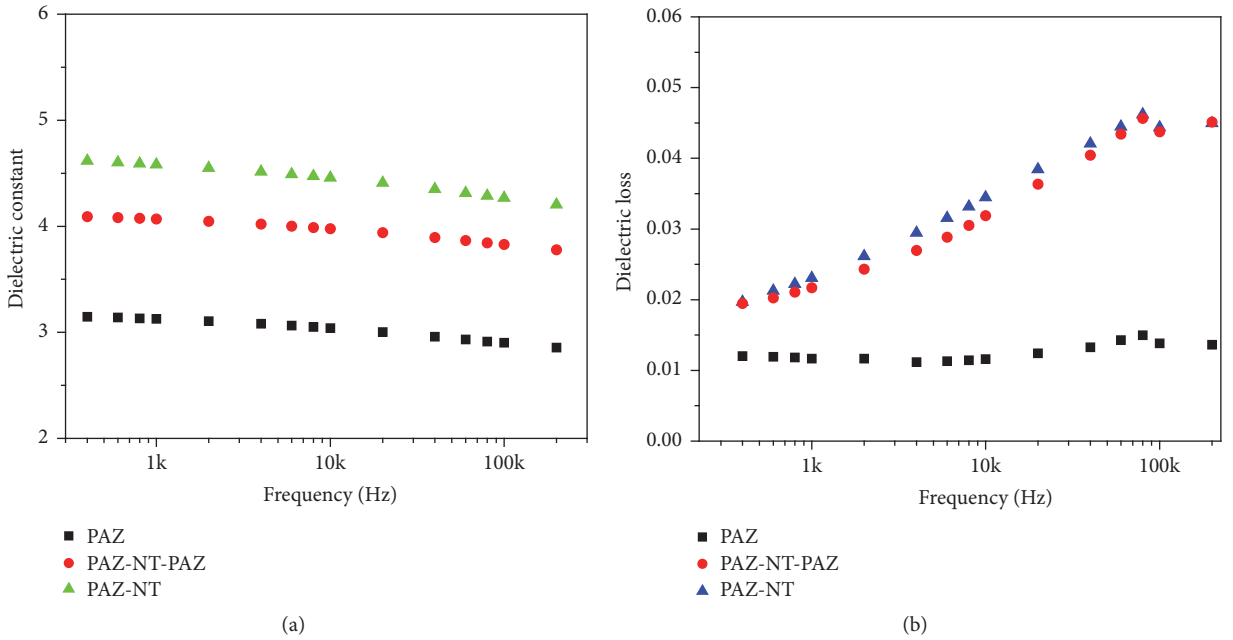

Figure 8: Dielectric constant (a) and dielectric loss (b) of the PAZ, PAZ-NT, and PAZ-NT-PAZ.

and contents of azo chromophores during the preparation process.

Conflicts of Interest

The authors declare that there are no conflicts of interest regarding the publication of this paper.

Acknowledgments

The financial support from National Natural Science Foundation of China (51603029) is gratefully acknowledged.

References

[1] B. Chu, X. Zhou, K. Ren, B. Neese, M. Lin, and Q. Zhang, "A dielectric polymer with high electric energy density and fast discharge peed," *Science*, vol. 313, no. 5785, pp. 334–337, 2006.

[2] P. Brochu and Q. Pei, "Advances in dielectric elastomers for actuators and artificial muscles," *Macromolecular Rapid Communications*, vol. 31, no. 1, pp. 10–36, 2010.

[3] A. Wypych, I. Bobowska, M. Tracz et al., "Dielectric properties and characterisation of titanium dioxide obtained by different chemistry methods," *Journal of Nanomaterials*, vol. 2014, Article ID 124814, 9 pages, 2014.

[4] V. S. Puli, D. K. Pradhan, B. C. Riggs, D. B. Chrisey, and R. S. Katiyar, "Investigations on structure, ferroelectric, piezoelectric and energy storage properties of barium calcium titanate (BCT) ceramics," *Journal of Alloys and Compounds*, vol. 584, pp. 369–373, 2014.

[5] S. Filipović, N. Obradović, J. Krstić et al., "Structural characterization and electrical properties of sintered magnesium-titanate ceramics," *Journal of Alloys and Compounds*, vol. 555, pp. 39–44, 2013.

[6] Y. You, X. Du, H. Mao, X. Tang, R. Wei, and X. Liu, "Synergistic enhancement of mechanical, crystalline and dielectric properties of polyarylene ether nitrile-based nanocomposites by unidirectional hot stretching–quenching," *Polymer International*, vol. 66, no. 8, pp. 1151–1158, 2017.

[7] Y. You, W. Han, L. Tu, Y. Wang, R. Wei, and X. Liu, "Double-layer core/shell-structured nanoparticles in polyarylene ether nitrile-based nanocomposites as flexible dielectric materials," *RSC Advances*, vol. 7, no. 47, pp. 29306–29311, 2017.

[8] Y.-H. Zhang, Z.-M. Dang, J. H. Xin et al., "Dielectric properties of polyimide-mica hybrid films," *Macromolecular Rapid Communications*, vol. 26, no. 18, pp. 1473–1477, 2005.

[9] K. K. Kim, A. Hsu, X. Jia et al., "Synthesis and characterization of hexagonal boron nitride film as a dielectric layer for graphene devices," *ACS Nano*, vol. 6, no. 10, pp. 8583–8590, 2012.

[10] B. Hoex, J. J. H. Gielis, M. C. M. Van De Sanden, and W. M. M. Kessels, "On the c-Si surface passivation mechanism by the negative-charge-dielectric Al2 O3," *Journal of Applied Physics*, vol. 104, no. 11, Article ID 113703, 2008.

[11] R. Yang, R. Wei, K. Li, L. Tong, K. Jia, and X. Liu, "Crosslinked polyarylene ether nitrile film as flexible dielectric materials with ultrahigh thermal stability," *Scientific Reports*, vol. 6, Article ID 36434, 2016.

[12] R. Wei, J. Wang, H. Zhang, W. Han, and X. Liu, "Crosslinked polyarylene ether nitrile interpenetrating with zinc ion bridged graphene sheet and carbon nanotube network," *Polymer*, vol. 9, no. 8, p. 342, 2017.

[13] A. Kahouli, O. Gallot-Lavallée, P. Rain et al., "Structure effect of thin film polypropylene view by dielectric spectroscopy and X-ray diffraction: Application to dry type power capacitors," *Journal of Applied Polymer Science*, vol. 132, no. 39, Article ID 42602, 2015.

[14] Y. Wang, X. Zhou, Q. Chen, B. Chu, and Q. Zhang, "Recent development of high energy density polymers for dielectric capacitors," *IEEE Transactions on Dielectrics and Electrical Insulation*, vol. 17, no. 4, pp. 1036–1042, 2010.

[15] M. F. Galikhanov, A. A. Guzhova, A. A. Efremova, and A. I. Nazmieva, "Effect of aluminum oxide coating on structural, barrier and electret properties of polyethylene terephthalate films," *IEEE Transactions on Dielectrics and Electrical Insulation*, vol. 22, no. 3, pp. 1492–1496, 2015.

[16] M. Sharma, M. P. Singh, C. Srivastava, G. Madras, and S. Bose, "Poly(vinylidene fluoride)-based flexible and lightweight materials for attenuating microwave radiations," *ACS Applied Materials & Interfaces*, vol. 6, no. 23, pp. 21151–21160, 2014.

[17] M. R. Gadinski, C. Chanthad, K. Han, L. Dong, and Q. Wang, "Synthesis of poly(vinylidene fluoride-co-bromotrifluoroethylene) and effects of molecular defects on microstructure and dielectric properties," *Polymer Chemistry*, vol. 5, no. 20, pp. 5957–5966, 2014.

[18] K. Li, L. Tong, R. Yang, R. Wei, and X. Liu, "In-situ preparation and dielectric properties of silver-polyarylene ether nitrile nanocomposite films," *Journal of Materials Science: Materials in Electronics*, vol. 27, no. 5, pp. 4559–4565, 2016.

[19] Y. Zhan, X. Yang, H. Guo, J. Yang, F. Meng, and X. Liu, "Cross-linkable nitrile functionalized graphene oxide/poly(arylene ether nitrile) nanocomposite films with high mechanical strength and thermal stability," *Journal of Materials Chemistry*, vol. 22, no. 12, pp. 5602–5608, 2012.

[20] L. Tong, R. Wei, J. Wang, and X. Liu, "Phthalonitrile end-capped polyarylene ether nitrile nanocomposites with Cu2+ bridged carbon nanotube and graphene oxide network," *Materials Letters*, vol. 178, pp. 312–315, 2016.

[21] R. Wei, K. Li, J. Ma, H. Zhang, and X. Liu, "Improving dielectric properties of polyarylene ether nitrile with conducting polyaniline," *Journal of Materials Science: Materials in Electronics*, vol. 27, no. 9, pp. 9565–9571, 2016.

[22] X. Liu, S. Long, D. Luo, W. Chen, and G. Cao, "Preparation and properties of polyarylene ether nitrites/multi-walled carbon nanotubes composites," *Materials Letters*, vol. 62, no. 1, pp. 19–22, 2008.

[23] T. Abdel-Baset, M. Elzayat, and S. Mahrous, "Characterization and optical and dielectric properties of polyvinyl chloride/silica nanocomposites films," *International Journal of Polymer Science*, vol. 2016, Article ID 1707018, 13 pages, 2016.

[24] Z. Wang, R. Wei, and X. Liu, "Preparation and dielectric properties of copper phthalocyanine/graphene oxide nanohybrids via in situ polymerization," *Journal of Materials Science*, vol. 51, no. 9, pp. 1–9, 2016.

[25] P. Jain, R. Muralidharan, J. Sedloff, X. Li, N. A. Alcantar, and J. P. Harmon, "Processing and performance of polymeric transparent conductive composites," *International Journal of Polymer Science*, vol. 2013, Article ID 845432, 13 pages, 2013.

[26] Z. F. Liu, K. Hashimoto, and A. Fujishima, "Photoelectrochemical information storage using an azobenzene derivative," *Nature*, vol. 347, no. 6294, pp. 658–660, 1990.

[27] R. Wei, X. Wang, and Y. He, "Synthesis of side-on liquid crystalline diblock copolymers through macromolecular azo coupling reaction," *European Polymer Journal*, vol. 69, article no. 6716, pp. 584–591, 2015.

[28] A. A. Beharry and G. A. Woolley, "Azobenzene photoswitches for biomolecules," *Chemical Society Reviews*, vol. 40, no. 8, pp. 4422–4437, 2011.

[29] R. Wei, J. Ma, H. Zhang, and Y. He, "Synthesis, characterization, and photo-responsive properties of Y-shaped amphiphilic azo triblock copolymer," *Journal of Applied Polymer Science*, vol. 133, no. 29, Article ID 43695, 2016.

[30] G. S. Kumar and D. C. Neckers, "Photochemistry of azobenzene-containing polymers," *Chemical Reviews*, vol. 89, no. 8, pp. 1915–1925, 1989.

[31] S. Xie, A. Natansohn, and P. Rochon, "Recent developments in aromatic azo polymers research," *Chemistry of Materials*, vol. 5, no. 4, pp. 403–411, 1993.

[32] A. Natansohn and P. Rochon, "Photoinduced motions in azo-containing polymers," *Chemical Reviews*, vol. 102, no. 11, pp. 4139–4175, 2002.

[33] H. Yu and T. Ikeda, "Photocontrollable liquid-crystalline actuators," *Advanced Materials*, vol. 23, no. 19, pp. 2149–2180, 2011.

[34] R. Wei, Z. Xu, X. Liu, Y. He, and X. Wang, "Liquid-crystalline compounds containing both a strong push-pull azo chromophore and a cholesteryl unit as photoresponsive molecular glass materials," *Journal of Materials Chemistry C*, vol. 3, no. 41, pp. 10925–10933, 2015.

[35] Y. Zhu, Y. Zhou, and X. Wang, "Photoresponsive behavior of two well-defined azo polymers with different electron-withdrawing groups on push-pull azo chromophores," *Dyes and Pigments*, vol. 99, no. 1, pp. 209–219, 2013.

[36] G. Ye, D. Wang, Y. He, and X. Wang, "Nunchaku-like molecules containing both an azo chromophore and a biphenylene unit as a new type of high-sensitivity photo-storage material," *Journal of Materials Chemistry*, vol. 20, no. 47, pp. 10680–10687, 2010.

[37] Y. He, X. Wang, and Q. Zhou, "Epoxy-based azo polymers: synthesis, characterization and photoinduced surface-relief-gratings," *Polymer Journal*, vol. 43, no. 26, pp. 7325–7333, 2002.

[38] C. Hubert, C. Fiorini-Debuisschert, I. Maurin, J.-M. Nunzi, and P. Raimond, "Spontaneous patterning of hexagonal structures in an AZO-polymer using light-controlled mass transport," *Advanced Materials*, vol. 14, no. 10, pp. 729–732, 2002.

[39] H. Finkelmann, E. Nishikawa, G. G. Pereira et al., "A new opto-mechanical effect in solids," *Physical Review Letters*, vol. 87, no. 1, 2001, 015501.

[40] M.-H. Li, P. Keller, B. Li, X. Wang, and M. Brunet, "Light-driven side-on nematic elastomer actuators," *Advanced Materials*, vol. 15, no. 7-8, pp. 569–572, 2003.

[41] Y. L. Yu, M. Nakano, and T. Ikeda, "Photomechanics: directed bending of a polymer film by light," *Nature*, vol. 425, no. 6954, p. 145, 2003.

[42] D. Lei, J. Runt, A. Safari, and R. E. Newnham, "Dielectric properties of azo dye-poly(methyl methacrylate) mixtures," *Macromolecules* , vol. 20, no. 8, pp. 1797–1801, 1987.

[43] X. Wang, S. Balasubramanian, J. Kumar, S. K. Tripathy, and L. Li, "Azo chromophore-functionalized polyelectrolytes. 1. synthesis, characterization, and photoprocessing," *Chemistry of Materials*, vol. 10, no. 6, pp. 1546–1553, 1998.

[44] X. Wang, K. Yang, J. Kumar et al., "Heteroaromatic chromophore functionalized epoxy-based nonlinear optical polymers," *Macromolecules* , vol. 31, no. 13, pp. 4126–4134, 1998.

[45] J. Wang, Y. Zhou, X. Wang, and Y. He, "Synthesis of Y-shaped amphiphilic copolymers by macromolecular azo coupling reaction," *RSC Advances*, vol. 5, no. 13, pp. 9476–9481, 2015.

[46] Y. He, W. He, D. Liu, T. Gu, R. Wei, and X. Wang, "Synthesis of block copolymers via the combination of RAFT and a macromolecular azo coupling reaction," *Polymer Chemistry*, vol. 4, no. 2, pp. 402–406, 2013.

[47] Y. Zhu, Y. Zhou, Z. Chen, R. Lin, and X. Wang, "Photoresponsive diblock copolymers bearing strong push-pull azo chromophores and cholesteryl groups," *Polymer*, vol. 53, no. 16, pp. 3566–3576, 2012.